

EARLY X-RAY FLARES IN GRBS

R. RUFFINI,^{1,2,3,4} Y. WANG,^{1,2} Y. AIMURATOV,^{1,2} U. BARRES DE ALMEIDA,⁴ L. BECERRA,^{1,2} C. L. BIANCO,^{1,2}
Y. C. CHEN,^{1,2} M. KARLICA,^{1,2,3} M. KOVACEVIC,^{1,2,3} L. LI,^{2,5} J. D. MELON FUKSMAN,^{1,2} R. MORADI,^{1,2} M. MUCCINO,^{1,2}
A. V. PENACCHIONI,^{6,7,2} G. B. PISANI,^{1,2} D. PRIMORAC,^{1,2} J. A. RUEDA,^{1,2,4} S. SHAKERI,^{8,2} G. V. VERESHCHAGIN,^{1,2} AND
S.-S. XUE^{1,2}

¹*ICRA and Dipartimento di Fisica, Sapienza Università di Roma, P.le Aldo Moro 5, 00185 Rome, Italy*

²*ICRANet, P.zza della Repubblica 10, 65122 Pescara, Italy. yu.wang@icranet.org*

³*Université de Nice Sophia Antipolis, CEDEX 2, Grand Château Parc Valrose, Nice, France*

⁴*ICRANet-Rio, Centro Brasileiro de Pesquisas Físicas, Rua Dr. Xavier Sigaud 150, 22290-180 Rio de Janeiro, Brazil*

⁵*Department of Physics, Stockholm University, SE-106 91 Stockholm, Sweden*

⁶*ASI Science Data Center, Via del Politecnico s.n.c., 00133 Rome, Italy*

⁷*Dept. of Physical Sciences, Earth and Environment, University of Siena, Via Roma 56, 53100 Siena, Italy*

⁸*Department of Physics, Isfahan University of Technology, 84156-83111, Iran*

ABSTRACT

We analyze the early X-ray flares in the GRB “flare-plateau-afterglow” (FPA) phase observed by Swift-XRT. The FPA occurs only in one of the seven GRB subclasses: the binary-driven hypernovae (BdHNe). This subclass consists of long GRBs with a carbon-oxygen core and a neutron star (NS) binary companion as progenitors. The hypercritical accretion of the supernova (SN) ejecta onto the NS can lead to the gravitational collapse of the NS into a black hole. Consequently, one can observe a GRB emission with isotropic energy $E_{iso} \gtrsim 10^{52}$ erg, as well as the associated GeV emission and the FPA phase. Previous work had shown that gamma-ray spikes in the prompt emission occur at $\sim 10^{15}$ – 10^{17} cm with Lorentz gamma factor $\Gamma \sim 10^2$ – 10^3 . Using a novel data analysis we show that the time of occurrence, duration, luminosity and total energy of the X-ray flares correlate with E_{iso} . A crucial feature is the observation of thermal emission in the X-ray flares that we show occurs at radii $\sim 10^{12}$ cm with $\Gamma \lesssim 4$. These model independent observations cannot be explained by the “fireball” model, which postulates synchrotron and inverse Compton radiation from a single ultra relativistic jetted emission extending from the prompt to the late afterglow and GeV emission phases. We show that in BdHNe a collision between the GRB and the SN ejecta occurs at $\simeq 10^{10}$ cm reaching transparency at $\sim 10^{12}$ cm with $\Gamma \lesssim 4$. The agreement between the thermal emission observations and these theoretically derived values validates our model and opens the possibility of testing each BdHN episode with the corresponding Lorentz gamma factor.

Keywords: gamma-ray burst: general — binaries: general — stars: neutron — supernovae: general
— black hole physics — hydrodynamics

1. INTRODUCTION

Following the discovery of the gamma-ray bursts (GRBs) by the Vela satellites (Klebesadel et al. 1973) and the observations by the BATSE detectors on board the Compton Gamma-Ray Observatory (CGRO, Gehrels et al. 1993), a theoretical framework for the interpretation of GRBs was established. This materialized into the “traditional” model of GRBs developed in a large number of papers by various groups. They all agree in their general aspects: short GRBs are assumed to originate from the merging of binary NSs (see, e.g., Goodman 1986; Paczynski 1986; Eichler et al. 1989; Narayan et al. 1991, 1992; Mészáros & Rees 1997), and long GRBs are assumed to originate from a “collapsar” (Woosley 1993; Paczyński 1998; MacFadyen & Woosley 1999; Bromberg et al. 2013) which, in turn, originates from the collapse of the core of a single massive star to a black hole (BH) surrounded by a thick massive accretion disk (Piran 2004). In this traditional picture the GRB dynamics follows the “fireball” model, which assumes the existence of an ultra-relativistic collimated jet (see e.g. Shemi & Piran 1990; Piran et al. 1993; Meszaros et al. 1993; Mao & Yi 1994). The structures of long GRBs were described either by internal or external shocks (see Rees & Meszaros 1992, 1994). The emission processes were linked to the occurrence of synchrotron and/or inverse-Compton radiation coming from the jetted structure, characterized by Lorentz factors $\Gamma \sim 10^2$ – 10^3 , in what later become known as the “prompt emission” phase (see Sec. 3).

The joint X-ray, gamma ray and optical observations heralded by Beppo-SAX and later extended by Swift have discovered the X-ray “afterglow”, which allowed the optical identification and the determination of the GRBs cosmological distance. The first evidence for the coincidence of a GRB and a supernova (SN) (GRB 980425/SN 1998bw) was also announced, as well as the first observation of an early X-ray flare (XRT), later greatly extended in number and spectral data by the Swift satellite, the subjects of this paper. The launch of the Fermi and AGILE satellites led to the equally fundamental discovery of the GeV emission both in long and short GRBs (see Sec. 2).

The traditional model reacted to these new basic informations by extending the description of the “collapsar” model, adopted for the prompt emission, both to the afterglow and to the GeV emission. This approach based on the gravitational collapse of a single massive star, was initially inspired by analogies with the astrophysics of active galactic nuclei, has been adopted with the aim to identify a “standard model” for all long GRBs and vastly accepted by concordance (see, e.g., Piran 1999, 2004; Mészáros 2002, 2006; Gehrels et al. 2009; Berger 2014; Kumar & Zhang 2015). Attempts to incorporate the occurrence of a SN in the collapsar by considering nickel production in the accretion process around the BH were also proposed (MacFadyen & Woosley 1999). In 1999, a pioneering work by Fryer et al. (1999) introduced considerations based on population synthesis computations and emphasized the possible relevance of binary progenitors in GRBs.

Since 2001 we have developed an alternative GRB model based on the concept of induced gravitational collapse (IGC) paradigm which involves, as progenitors, a binary system with standard components: an evolved carbon-oxygen core (CO_{core}) and a binary companion neutron star (NS). The CO_{core} undergoes a traditional Ic SN explosion, which produces a new NS (νNS) and a large amount of ejecta. There is a multitude of new physical processes, occurring in selected episodes, associated with this process. The “first episode” (see Sec. 3) of the binary-driven hypernova (BdHN) is dominated by the hypercritical accretion process of the SN ejecta on the companion NS. This topic has been developed in (see, e.g., Ruffini et al. 2001c; Rueda & Ruffini 2012; Fryer et al. 2014; Becerra et al. 2015, 2016). These processes are not considered in the collapsar model. Our SN is a traditional type Ic, the creation of the νNS follows standard procedure occurring in pulsar physics (see e.g. Negreiros et al. 2012), the companion NS is a standard one regularly observed in binaries (see e.g. Rueda et al. 2017; Rueda & Ruffini 2012) and the physics of hypercritical accretion has been developed by us in a series of recent articles (see Sec. 3.4).

In BdHN the BH and a vast amount of e^+e^- plasma are formed only after the accreting NS reaches the critical mass and the “second episode” starts (see Sec. 3.5). The main new aspect of our model addresses the interaction of the e^+e^- plasma with the SN ejecta. We apply the fireshell model which make use of a general relativistic correct space-time parametrisation of the GRBs, as well as a new set of relativistic hydrodynamics equation for the dynamics of the e^+e^- plasma. Selected values of the baryon loads are adopted in correspondence to the different time varying density distribution of the SN ejecta.

In the “third episode” (see Sec. 3.6), we mention also the perspectives, utilising the experience gained both in data analysis and in the theory for the specific understanding of X-ray flares, to further address in forthcoming publications the more comprehensive case of the gamma-ray flares, the consistent treatment of the Afterglow and finally the implication of the GeV radiation.

As the model evolved we soon realized that the discovery of new sources was not leading to a “standard model” of long GRBs but, on the contrary, they were revealing a number of new GRB subclasses with distinct properties characterizing their light-curves, spectra and energetics (see [Ruffini et al. 2016a](#)). Moreover these seven subclasses did not necessarily contain a BH. We soon came to the conclusion that only in the subclass of BdHN, with an E_{iso} larger than 10^{52} erg, the hypercritical accretion from the SN into the NS leads to the creation of a newly-born BH with the associated signatures in the long GRB emission (see e.g. [Becerra et al. 2015, 2016](#)).

While our alternative model was progressing, we were supported by new astrophysical observations: the great majority of GRBs are related to type Ic SNe, which have no trace of hydrogen and helium in their optical spectra, and are spatially correlated with bright star-forming regions in their host galaxies ([Fruchter et al. 2006](#); [Svensson et al. 2010](#)). Most massive stars are found in binary systems ([Smith 2014](#)) where most type Ic SNe occur and which favor the deployment of hydrogen and helium from the SN progenitors ([Smith et al. 2011](#)), and the SNe associated with long GRBs are indeed of type Ic ([Della Valle 2011](#)). In addition, these SNe associated with long bursts are broad-lined Ic SNe (hypernovae) showing the occurrence of some energy injection leading to a kinetic energy larger than that of the traditional SNe Ic ([Lyman et al. 2016](#)).

The present paper addresses the fundamental role of X-ray flares as a separatrix between the two alternative GRB models and leads to the following main results, two obtained by the data analysis, and one obtained from the comparison of the alternative models:

- 1) The discovery of precise correlations between the X-ray flares and the GRB E_{iso} .
- 2) The radius of the occurrence X-ray flares ($\sim 10^{12}$ cm) and Lorentz Gamma factor ~ 2 .
- 3) The occurrence of a sharp brake between the prompt emission phase and the FPA phase, not envisaged in the current GRB literature. This transition evidence a contradiction in the ultra-relativistic jetted emission for explaining the X-ray flares, the plateau and the afterglow.

In [Sec. 2](#) we recall, following the gamma-ray observations by the Vela satellites and the Compton Gamma-Ray Observatory (CGRO), the essential role of Beppo-SAX and the Swift satellite. They provided the X-ray observations specifically on the X-ray flares, to which our new data-analysis techniques and paradigms have been applied. We also recall the Fermi and the AGILE satellites were the existence of the GeV emission was announced, which has become essential for establishing the division of GRBs into different subclasses.

In [Sec. 3](#) we update our classification of GRBs with known redshift into seven different subclasses (see [Table 2](#)). For each subclass we indicate the progenitor “in-states” and the corresponding “out-states”. We update the list of BdHNe (see [Appendix A](#)): long GRBs with $E_{iso} \gtrsim 10^{52}$ erg, with an associated GeV emission and with the occurrence of the FPA phase. We also recall the role of an appropriate time parametrization for GRBs, properly distinguishing the four time variables which enter into their analysis. Finally we recall the essential theoretical background needed for the description of the dynamics of BdHNe, the role of the neutrino emission in the process of hypercritical accretion of the SN ejecta onto the binary companion NS, the description of the dynamics of the e^+e^- -baryon plasma, and the prompt emission phase endowed with gamma-ray spikes. We then shortly address the new perspectives open by the present work, to be further extended to the analysis of gamma-ray flares, to the afterglow and the essential role of each BdHN component, including the ν NS. Having established the essential observational and theoretical background in [Secs. 2](#) and [3](#), we proceed to the data analysis of the X-ray flares.

In [Sec. 4](#) we address the procedure used to compare and contrast GRBs at different redshifts, including the description in their cosmological rest frame as well as the consequent K-corrections. This procedure has been neglected in the current GRB literature (see, e.g., [Chincarini et al. 2010](#), and references therein, as well as [Sec. 11](#)). We then identify the BdHNe as the only sources where early time X-ray flares are identifiable. We recall that no X-ray flares have been found in X-ray flashes, nor in short GRBs. We also show that a claim of the existence of X-ray flares in short bursts has been superseded. We recall our classified 345 BdHNe (through the end of 2016). Their T_{90}^1 , properly evaluated in the source rest-frame, corresponds to the duration of their prompt emission phase, mostly shorter than 100 s. Particular attention has been given to distinguishing the X-ray flares from the gamma-ray flares and spikes, each characterised by distinct spectral distributions and specific Lorentz gamma factors. The gamma ray flares are generally more energetic and with specific spectral signatures (see e.g. the significant example of GRB 140206A in [Sec. 5](#) below). In this article we focus on the methodology of studying X-ray flares: we plan to apply this knowledge

¹ The T_{90} is the duration defined as starting (ending) when the 5% (95%) of the total energy of the event in gamma-rays has been emitted.

to the case of the early gamma-ray flares. Out of the 345 BdHNe, there are 211 which have complete Swift-*XRT* observations, and among them, there are 16 BdHNe with a well-determined early X-ray flare structure. They cover a wide range of redshifts, as well as the typical range of BdHN isotropic energies ($\sim 10^{52}$ – 10^{54} erg). The sample includes all the identifiable X-ray flares.

In Sec. 5, we give the X-ray luminosity light curves of the 16 BdHNe of our sample and, when available, the corresponding optical observations. As usual, these quantities have been K-corrected to their rest frame (see Figs. 9–24, and Sec. 4). In order to estimate the global properties of these sources, we also examine data from the Swift, Konus-Wind and Fermi satellites. The global results of this large statistical analysis are given in Tab. 3 where the cosmological redshift z , the GRB isotropic energy E_{iso} , the flare peak time t_p , peak luminosity L_p , duration Δt , and the corresponding E_f are reproduced. This lengthy analysis has been carried out over the past years, and only the final results are summarized in Tab. 3.

In Sec. 6 we present the correlations between t_p , L_p , Δt , E_f and E_{iso} and give the corresponding parameters in Tab. 4. In this analysis we applied the Markov chain Monte Carlo (MCMC) method, and we also have made public the corresponding numerical codes in <https://github.com/YWangScience/AstroNeuron> and <https://github.com/YWangScience/MCCC>.

In Sec. 7 we discuss the correlation between the energy of the prompt emission, the energy of the FPA phase, and E_{iso} (see Tabs. 5–6 and Figs. 29–31).

In Sec. 8 we analyze the thermal emission observed during the X-ray flares (see Tab. 7). We derive, in an appropriate relativistic formalism, the relations between the observed temperature and flux and the corresponding temperature and radius of the thermal emitter in its comoving frame.

In Sec. 9 we use the results of Sec. 8 to infer the expansion speed of the thermal emitter associated with the thermal components observed during the flares (see Fig. 32 and Tab. 8). We find that the observational data implies a Lorentz factor $\Gamma \lesssim 4$ and a radius of $\approx 10^{12}$ cm for such a thermal emitter.

In Sec. 10 we present a theoretical treatment using a new relativistic hydrodynamical code to simulate the interaction of the e^+e^- -baryon plasma with the high-density regions of the SN ejecta. We first test the code in the same low-density domain of validity describing the prompt emission phase, and then we apply it in the high-density regime of the propagation of the plasma inside the SN ejecta which we use for the theoretical interpretation of the X-ray flares. Most remarkably, the theoretical code leads to a thermal emitter at transparency with a Lorentz factor $\Gamma \lesssim 4$ and a radius of $\approx 10^{12}$ cm. The agreement between these theoretically derived values and the ones obtained from the observed thermal emission validates the model and the binary nature of the BdHN progenitors, in clear contrast with the traditional ultra-relativistic jetted models.

In Sec. 11 we present our conclusions. We first show how the traditional model, describing GRBs as a single system with ultra-relativistic jetted emission extending from the prompt emission all the way to the final phases of the afterglow and of the GeV emission, is in conflict with the X-ray flare observations. We also present three main new results which illustrate new perspectives opened by our alternative approach based on the BdHNe.

A standard flat Λ CDM cosmological model with $\Omega_M = 0.27$, $\Omega_\Lambda = 0.73$, and $H_0 = 71$ km s $^{-1}$ Mpc $^{-1}$ is adopted throughout the paper, while Table 1 summarizes the acronyms we have used.

2. BACKGROUND FOR THE OBSERVATIONAL IDENTIFICATION OF THE X-RAY FLARES

The discovery of GRBs by the Vela satellites (Klebesadel et al. 1973) was presented at the AAAS meeting in February 1974 in San Francisco (Gursky & Ruffini 1975). The Vela satellites were operating in gamma rays in the 150–750 keV energy range and only marginally in X-rays (3–12 keV, Cline et al. 1979). Soon after it was hypothesized from first principles that GRBs may originate from an e^+e^- plasma in the gravitational collapse to a Kerr-Newman BH, implying an energy $\sim 10^{54} M_{BH}/M_\odot$ erg (Damour & Ruffini 1975, see also Ruffini 1998).

Since 1991 the BATSE detectors on the Compton Gamma-Ray Observatory (CGRO, see Gehrels et al. 1993) led to the classification of GRBs on the basis of their spectral hardness and of their observed T_{90} duration in the 50–300 keV energy band into short/hard bursts ($T_{90} < 2$ s) and long/soft bursts ($T_{90} > 2$ s (Mazets et al. 1981; Klebesadel 1992; Dezalay et al. 1992; Kouveliotou et al. 1993; Tavani 1998). Such an emission was later called the GRB “prompt emission”. In a first attempt it was proposed that short GRBs originate from merging binary NSs (see, e.g., Goodman 1986; Paczynski 1986; Eichler et al. 1989; Narayan et al. 1991, 1992; Mészáros & Rees 1997) and long GRBs originate from a single source with ultra-relativistic jetted emission (Woosley 1993; Paczyński 1998; MacFadyen & Woosley 1999; Bromberg et al. 2013).

Extended wording	Acronym
Binary-driven hypernova	BdHN
Black hole	BH
Carbon-oxygen core	CO _{core}
Circumburst medium	CBM
flare-Plateau-Afterglow	FPA
Gamma-ray burst	GRB
Gamma-ray flash	GRF
Induced gravitational collapse	IGC
Massive neutron star	MNS
Neutron star	NS
New neutron star	ν NS
Proper gamma-ray burst	P-GRB
Short gamma-ray burst	S-GRB
Short gamma-ray flash	S-GRF
Supernova	SN
Ultrashort gamma-ray burst	U-GRB
White dwarf	WD
X-ray flash	XRF

Table 1. Alphabetic ordered list of the acronyms used in this work.

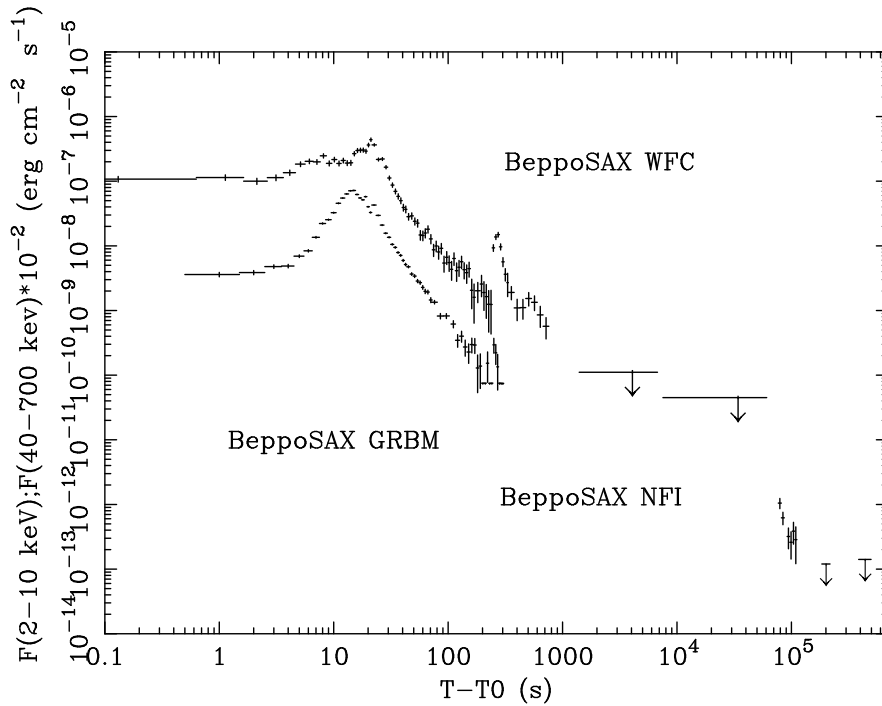


Figure 1. First X-ray flare observed by BeppoSAX in GRB 011121. Reproduced from Piro et al. (2005).

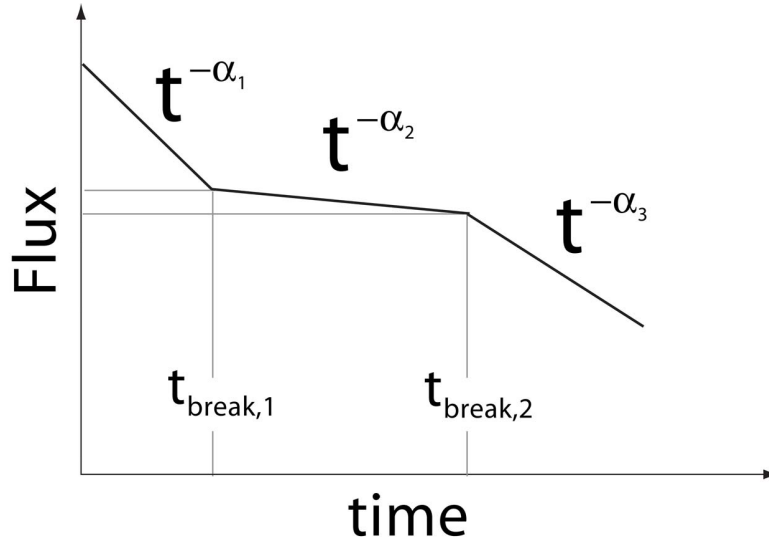


Figure 2. Schematic diagram of the X-ray light-curve composed of three power-law segments with different slopes ($3 \lesssim \alpha_1 \lesssim 5$, $0.5 \lesssim \alpha_2 \lesssim 1.0$, $1 \lesssim \alpha_3 \lesssim 1.5$). Figure taken from [Nousek et al. \(2006\)](#).

The Beppo-SAX satellite, operating since 1996, joined the expertise of the X-ray and gamma-ray communities. Its gamma-ray burst monitor (GRBM) operating in the 40–700 keV energy band determined the trigger of the GRB and two wide field cameras (WFCs) operating in the 2–30 keV X-ray energy band allowed the localization of the source within an arc minute resolution. This enabled a follow-up with the narrow field instruments (NFI) in the 2–10 keV energy band. Beppo-SAX discovered the X-ray afterglow ([Costa et al. 1997](#)), characterized by an X-ray luminosity decreasing with a constant index of ~ -1.3 (see [de Pasquale et al. 2006](#), as well as [Pisani et al. 2016](#)). This emission was detected after an “8 hour gap,” following the prompt emission identified by BATSE. The consequent determination of the accurate positions by the NFI, transmitted to the optical ([van Paradijs et al. 1997](#)) and radio telescopes ([Frail et al. 1997](#)), allowed the determination of the GRB cosmological redshifts ([Metzger et al. 1997](#)). The derived distances of ≈ 5 –10 Gpc confirmed their cosmological origin and their unprecedented energetics $\approx 10^{50}$ – 10^{54} erg, thus validating our hypothesis derived from first principles ([Damour & Ruffini 1975](#); [Ruffini 1998](#)).

To Beppo-SAX goes the credit of the discovery of the temporal and spatial coincidence of GRB 980425 with SN 1998bw ([Galama et al. 1998](#)), which suggested the connection between GRBs and SNe, soon supported by many additional events (see e.g. [Woosley & Bloom 2006](#); [Della Valle 2011](#); [Hjorth & Bloom 2012](#)). Beppo-SAX also discovered the first “X-ray flare” in GRB 011121 closely following the prompt emission ([Piro et al. 2005](#)), see Fig. 1. Our goal in this paper is to show how the X-ray flares, thanks to the observational campaign of the Swift satellite, have become the crucial test for understanding the astrophysical nature of the GRB-SN connection.

The Swift burst alert telescope (BAT), operating in the 15–150 keV energy band, can detect GRB prompt emissions and accurately determine their position in the sky within 3 arcmin. Within 90 s Swift can re-point the narrow-field X-ray telescope (XRT), operating in the 0.3–10 keV energy range, and relay the burst position to the ground. This overcame the “8 hour gap” in the Beppo-SAX data.

Thanks to the Swift satellite, the number of detected GRBs increased rapidly to 480 sources with known redshifts. By analyzing the light-curve of some long GRBs including the data in the “8 hour gap” of Beppo-SAX, [Nousek et al. \(2006\)](#) and [Zhang et al. \(2006\)](#) discovered three power-law segments in the XRT flux light-curves of some long GRBs. We refer to these as the “Nousek-Zhang power laws” (see Fig. 2). The nature of this feature has been the subject of a long debates, still ongoing, and finally resolved in this article.

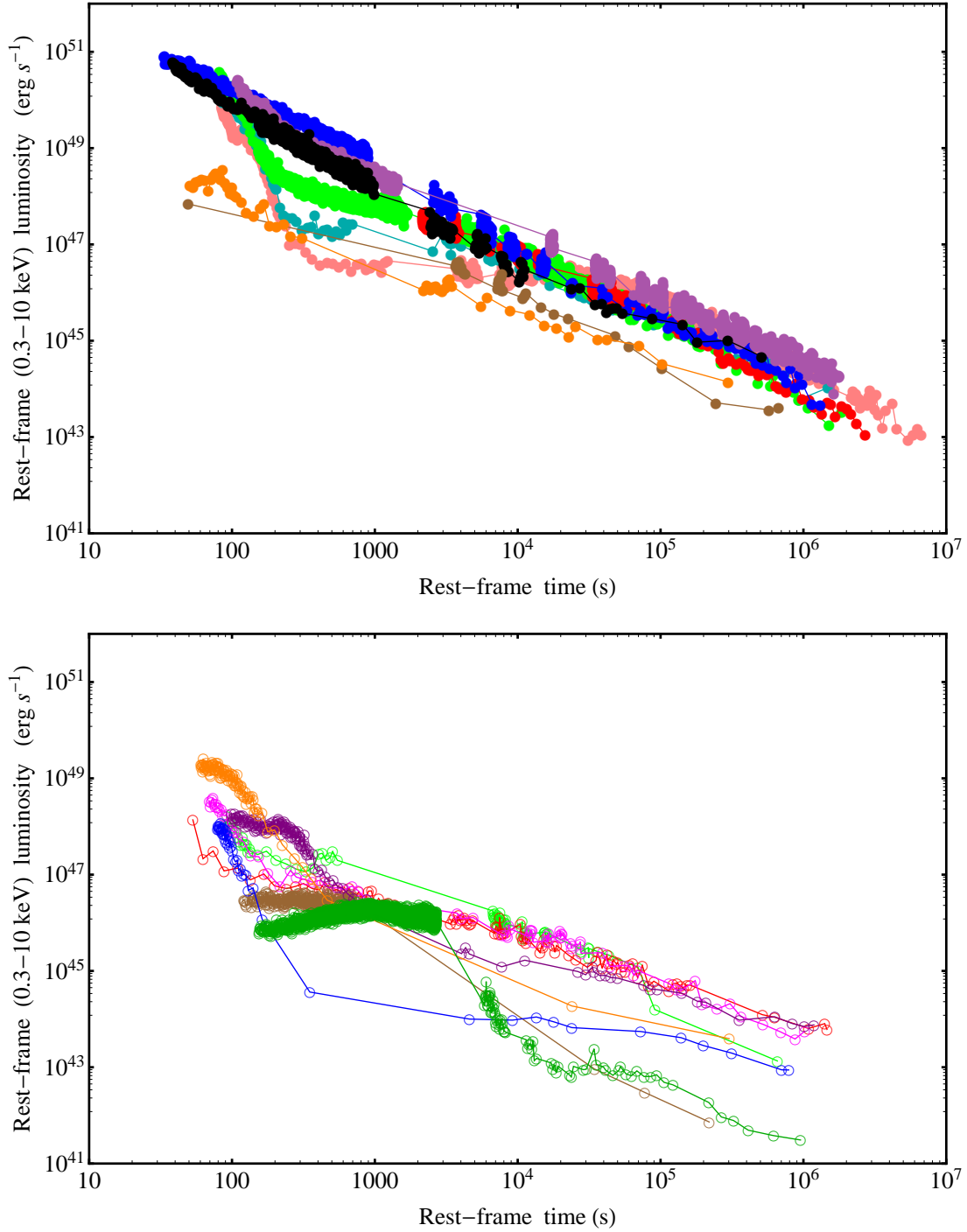


Figure 3. X-ray light-curves of long GRBs observed by Swift. Top panel: BdHNe 050525 (brown), 060729 (pink), 061007 (black), 080319B (blue), 090618 (green), 091127 (red), 100816A (orange), 111228A (light blue), and 130427A (purple). Bottom panel: XRFs 050416A (red), 060218 (dark green), 070419A (orange), 081007 (magenta), 100316D (brown), 101219B (purple), and 130831A (green). XRFs have generally lower and more scattered light-curves. All these GRBs have known redshift, and the light-curves have been transformed to their cosmological rest frames.

Table 2. Summary of the seven GRB subclasses (XRFs, BdHNe, BH-SN, short gamma-ray flashes (S-GRFs), authentic short GRBs (S-GRBs), ultrashort GRBs (U-GRB), and GRFs) and of their observational properties. In the first five columns we indicate the GRB subclasses and their corresponding number of sources with measured z , *in-states* and *out-states*. In the following columns we list the ranges of T_{90} in the rest-frame, rest-frame spectral peak energies $E_{p,i}$ and E_{iso} (rest-frame 1– 10^4 keV), the isotropic energy of the X-ray data $E_{iso,X}$ (rest-frame 0.3–10 keV), and the isotropic energy of the GeV emission $E_{iso,GeV}$ (rest-frame 0.1–100 GeV). In the last column we list, for each GRB subclass, the local observed number density rate ρ_{GRB} obtained in Ruffini et al. (2016a). For details see Ruffini et al. (2014, 2015a,b); Fryer et al. (2015); Ruffini et al. (2016b,a); Becerra et al. (2016).

Subclass	number	<i>In-state</i> (<i>Progenitor</i>)	<i>Out-state</i> (<i>Final outcome</i>)	T_{90} (s)	$E_{p,i}$ (MeV)	E_{iso} (erg)	$E_{iso,X}$ (erg)	$E_{iso,GeV}$ (erg)	ρ_{GRB} ($\text{Gpc}^{-3}\text{yr}^{-1}$)	
I	XRFs	82	$\text{CO}_{\text{core}}\text{-NS}$	$\nu\text{NS-NS}$	$\sim 2\text{-}10^3$	$\lesssim 0.2$	$\sim 10^{48}\text{-}10^{52}$	$\sim 10^{48}\text{-}10^{51}$	–	100^{+45}_{-34}
II	BdHNe	345	$\text{CO}_{\text{core}}\text{-NS}$	$\nu\text{NS-BH}$	$\sim 2\text{-}10^2$	$\sim 0.2\text{-}2$	$\sim 10^{52}\text{-}10^{54}$	$\sim 10^{51}\text{-}10^{52}$	$\lesssim 10^{53}$	$0.77^{+0.09}_{-0.08}$
III	BH-SN	–	$\text{CO}_{\text{core}}\text{-BH}$	$\nu\text{NS-BH}$	$\sim 2\text{-}10^2$	$\gtrsim 2$	$> 10^{54}$	$\sim 10^{51}\text{-}10^{52}$	$\gtrsim 10^{53}$	$\lesssim 0.77^{+0.09}_{-0.08}$
IV	S-GRFs	33	NS-NS	MNS	$\lesssim 2$	$\lesssim 2$	$\sim 10^{49}\text{-}10^{52}$	$\sim 10^{49}\text{-}10^{51}$	–	$3.6^{+1.4}_{-1.0}$
V	S-GRBs	7	NS-NS	BH	$\lesssim 2$	$\gtrsim 2$	$\sim 10^{52}\text{-}10^{53}$	$\lesssim 10^{51}$	$\sim 10^{52}\text{-}10^{53}$	$(1.9^{+1.8}_{-1.1}) \times 10^{-3}$
VI	U-GRBs	–	$\nu\text{NS-BH}$	BH	$\ll 2$	$\gtrsim 2$	$> 10^{52}$	–	–	$\gtrsim 0.77^{+0.09}_{-0.08}$
VII	GRFs	13	NS-WD	MNS	$\sim 2\text{-}10^2$	$\sim 0.2\text{-}2$	$\sim 10^{51}\text{-}10^{52}$	$\sim 10^{49}\text{-}10^{50}$	–	$1.02^{+0.71}_{-0.46}$

We have used Swift-XRT data in differentiating two distinct subclasses of long GRBs, the XRFs with $E_{iso} \lesssim 10^{52}$ erg and the BdHNe with $E_{iso} \gtrsim 10^{52}$ erg (see Sec. 3). An additional striking difference appears between the XRT luminosities of these two subclasses when measured in their cosmological rest frames: in the case of BdHNe the light-curves follow a specific behavior which conforms to the Nousek-Zhang power-law (see e.g. Penacchioni et al. 2012, 2013; Pisani et al. 2013, 2016; Ruffini et al. 2014). None of these features are present in the case of XRFs (see Fig. 3).

Finally, the Fermi satellite (Atwood et al. 2009) launched in 2008 detects ultra-high energy photons from 20 MeV to 300 GeV with the large area telescope (LAT), and detects photons from 8 keV to 30 MeV with the gamma-ray burst monitor (GBM). For the purposes of this article addressing long GRBs, the Fermi observations have been prominent in further distinguishing XRFs and BdHNe: the Fermi-LAT GeV emission has been observed only in BdHNe and never in XRFs.

3. BACKGROUND FOR THE THEORETICAL INTERPRETATION OF X-RAY FLARES AND THEIR DYNAMICS

3.1. The classification of GRBs

The very extensive set of observations carried out by the above satellites in coordination with the largest optical and radio telescopes over a period of almost 40 years has led to an impressive set of data on 480 GRBs, all characterized by spectral, luminosity, and time variability information, and each one with a well established cosmological redshift. By classifying both the commonalities and the differences among all GRBs it has been possible to create “equivalence relations” and divide GRBs into a number of subclasses, each one identified by a necessary and sufficient number of observables. We recall in Tab. 2 and Fig. 4 the binary nature of all GRB progenitors and their classification into seven different subclasses (see e.g. Ruffini et al. 2016a). In Tab. 2 we indicate the number of sources in each subclass, the nature of their progenitors and final outcomes of their evolution, their rest-frame T_{90} , their rest frame spectral peak energy $E_{p,i}$ and E_{iso} , as well as the isotropic energy in X-rays $E_{iso,X}$ and in GeV emission $E_{iso,GeV}$, and finally their local observed number density rate. In Fig. 4 we mention for these sources the $E_{p,i}$ – E_{iso} relations, including the Amati one for BdHNe and the MuRuWaZha one for the short bursts (see Ruffini et al. 2016a,b), comprising short gamma-ray flashes (S-GRFs) with $E_{iso} \lesssim 10^{52}$ erg, authentic short GRBs (S-GRBs) with $E_{iso} \gtrsim 10^{52}$ erg, and gamma-ray flashes (GRFs), sources with hybrid short/long burst properties in their gamma-ray light curves, i.e., an initial spike-like harder emission followed by a prolonged softer emission observed up to ~ 100 s, originating from NS–white dwarf binaries (Caito et al. 2009, 2010; Ruffini et al. 2016a). We have no evidence for an $E_{p,i}$ and E_{iso} relation in the XRFs (see Fig. 4). The Amati and the MuRuWaZha relations have not yet been theoretically understood, and as such they have no predictive power.

3.2. The role of the time parametrization in GRBs

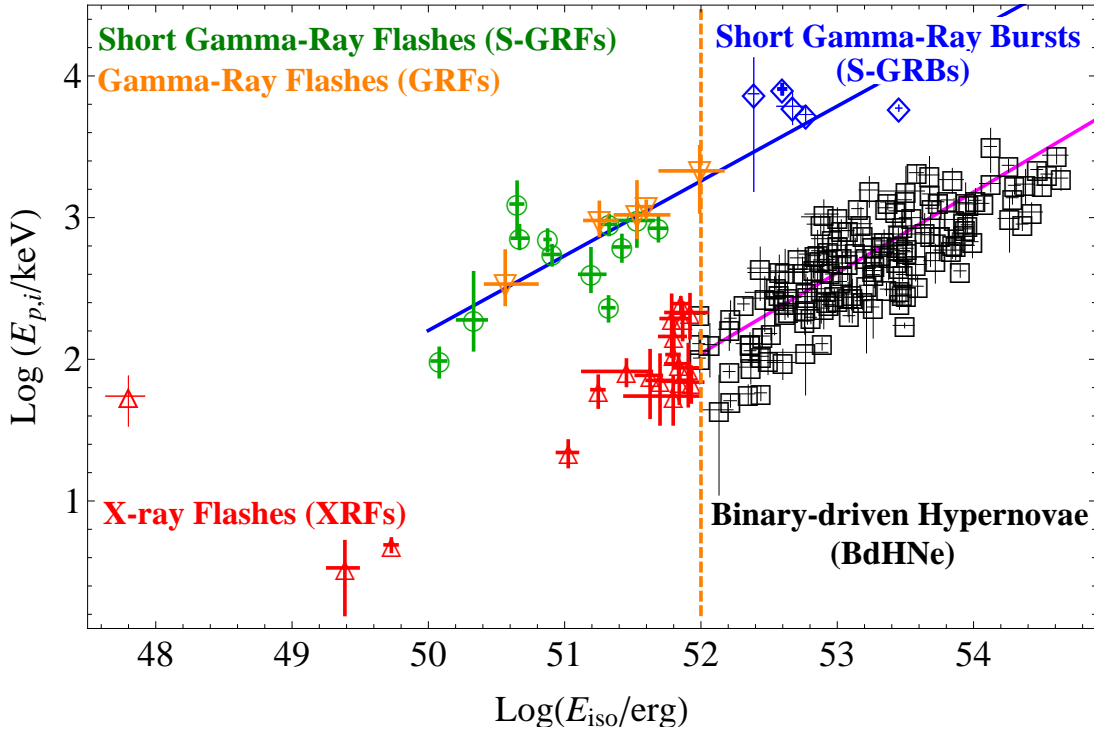


Figure 4. The updated $E_{p,i}-E_{iso}$ plane for the subclasses defined in Ruffini et al. (2016a): XRFs (red triangles) cluster in the region defined by $E_{p,i} \lesssim 200$ keV and $E_{iso} \lesssim 10^{52}$ erg. BdHNe (black squares) cluster in the region defined by $E_{p,i} \gtrsim 200$ keV and $E_{iso} \gtrsim 10^{52}$ erg and fulfill the Amati relation (solid magenta line with slope $\alpha = 0.57 \pm 0.06$ and extra scatter $\sigma = 0.25$, see e.g. Amati & Della Valle 2013; Calderone et al. 2015). S-GRFs (green circles) and the initial spike-like emission of the GRFs (orange reverse triangles) are concentrated in the region defined by $E_{p,i} \lesssim 2$ MeV and $E_{iso} \lesssim 10^{52}$ erg, while S-GRBs (blue diamonds) in the region defined by $E_{p,i} \gtrsim 2$ MeV and $E_{iso} \gtrsim 10^{52}$ erg. Short bursts and GRFs fulfill the MuRuWaZha relation (blue solid line with slope $\alpha = 0.53 \pm 0.07$ and extra scatter $\sigma = 0.24$, see e.g. Ruffini et al. 2015a; Calderone et al. 2015; Zhang et al. 2012; Ruffini et al. 2016b). BH-SN and U-GRB subclasses (see Tab. 2 Ruffini et al. 2016a, for details) are not in the plot since their observational identification is still pending. The crucial difference between BdHNe and XRFs, and SGRBs and SGRF, is that BdHNe and S-GRBs form a BH, their energy is $\gtrsim 10^{52}$ erg, and exhibit the GeV emission.

Precise general relativistic rules in the space-time parameterization of GBRs are needed (Ruffini et al. 2001a). Indeed, there are four time variables entering this discussion which have to be properly distinguished one from another: 1) the comoving time t_{com} , which is the time used to compute the evolution of the thermodynamical quantities (density, pressure, temperature); 2) the laboratory time $t = \Gamma t_{com}$, where as usual the Lorentz gamma factor is $\Gamma = (1 - \beta^2)^{-1/2}$ and $\beta = v/c$ is the expansion velocity of the source; 3) the arrival time t_a at which each photon emitted by the source reaches an observer in the cosmological rest frame of the source, given by (see also Bianco et al. 2001; Ruffini et al. 2002; Bianco & Ruffini 2005a):

$$t_a = t - \frac{r(t)}{c} \cos \vartheta, \quad (1)$$

where $r(t)$ is the radius of the expanding source in the laboratory frame and ϑ is the displacement angle of the normal to the emission surface from the line of sight; and 4) the arrival time at the detector on the Earth $t_a^d = t_a(1 + z)$ corrected for cosmological effects, where z is the source redshift, needed in order to compare GRBs at different redshifts z . As emphasized in Ruffini et al. (2001a), “the bookkeeping of these four different times and the corresponding space variables must be done carefully in order to keep the correct causal relation in the time sequence of the events involved”. The chain of relations between these four times is given by (see e.g. Bianco et al. 2001; Ruffini et al. 2001a, 2002; Bianco & Ruffini 2005a, and see also Secs. 8 and 9 for the dynamics of the flares):

$$t_a^d = (1 + z)t_a = (1 + z) \left(t - \frac{r(t)}{c} \cos \vartheta \right) = (1 + z) \left(\Gamma t_{com} - \frac{r(\Gamma t_{com})}{c} \cos \vartheta \right). \quad (2)$$

The proper use of these four time variables is mandatory in modeling GRB sources, especially when we are dealing with a model not based on a single component but on multiple components, each characterized by a different world-line and a different Lorentz gamma factor, as it is the case for BdHNe (see Secs. 4 and 5).

3.3. *The role of the GRBs cosmological rest-frame*

In addition to all the above, in order to compare the luminosities of different GRBs at different redshifts we need to express the observational data in the cosmological rest frames of each source (where the arrival time is t_a), and correspondingly apply the K-correction to luminosities and spectra (see Sec. 4). This formalism is at the very foundation of the treatment presented in this paper and has been systematically neglected in the great majority of current GRB models.

3.4. *The Episode 1 :The hypercritical accretion process*

In order to describe the dynamics of BdHNe a number of different episodes involving different physical conditions have to be described. Episode 1 is dominated by the IGC paradigm: the hypercritical accretion of a SN ejecta on the companion binary NS (see, e.g., Fryer et al. 2014; Becerra et al. 2015; Fryer et al. 2015; Becerra et al. 2016). Weak interactions and neutrinos (see e.g. Fermi 1934), which play a fundamental role in SN through the URCA process (Gamow & Schoenberg 1940, 1941), are also needed in the case of hypercritical accretion processes onto a NS in a SN fallback (Colgate 1971; Zel’dovich et al. 1972; Ruffini & Wilson 1973). They are especially relevant in the case of BdHNe where the accretion rate onto the NS companion from the CO_{core} can reach up to $\dot{M} = 0.1 M_{\odot} \text{ s}^{-1}$ (Rueda & Ruffini 2012; Fryer et al. 2014; Becerra et al. 2015, 2016). Due to weak interactions, e^+e^- pairs annihilate to $\nu\bar{\nu}$ pairs with a cross-section $\sigma \sim G_F \langle E_e \rangle^2$ (Munakata et al. 1985; Itoh et al. 1989). In the thermal system of e^+e^- pairs at large temperature $kT > m_e c^2$ and density $n_e \sim T^3$, the neutrino emissivity of the e^+e^- annihilation is $\epsilon_{e^+e^-} \sim n_e^2 \langle \sigma v_e \rangle \langle E_e \rangle \sim 10^{25} (kT/\text{MeV})^9 \text{ erg s}^{-1} \text{ cm}^{-3}$, leading to neutrino luminosities $L_{\nu} \sim R_{\text{NS}}^3 \epsilon_{e^+e^-} \sim 10^{52} \text{ erg s}^{-1}$, which dominate over other microscopic processes for cooling (Becerra et al. 2016). Thus the e^+e^- pair annihilation to $\nu\bar{\nu}$ is the main process for cooling, allowing the process of hypercritical accretion to convert gravitational energy to thermal energy, to build up high temperature and consequently to form an e^+e^- plasma. Only at the end of this Episode 1, as the critical mass of the companion NS is reached, a BH is formed with the additional e^+e^- pairs linked to the BH electro-dynamical process (Damour & Ruffini 1975; Cherubini et al. 2009).

3.5. *The e^+e^- pairs colliding with the SN ejecta*

Episode 2. This Episode is dominated by the new phenomena of the impact of the e^+e^- pairs generated in the GRB with the SN ejecta. We describe this process within the fireshell model. Two main differences exist between the fireshell and the fireball model. In the fireshell model the e^+e^- plasma is initially in thermal equilibrium and undergoes an ultra-relativistic expansion keeping this condition of thermal equilibrium all the way to reaching transparency (Ruffini 1998, see also Aksenov et al. 2007; Ruffini et al. 2010 and references therein) while, in the fireball model Cavallo & Rees (1978), the e^+e^- pairs undergo an initial annihilation process producing the photons driving the fireball. An additional basic difference is that the evolution of the e^+e^- plasma is not imposed by a given asymptotic solution but integrated following the relativistic fluid dynamics equations. The plasma, with energy $E_{e^+e^-}$, goes first through an initial acceleration phase (Ruffini et al. 1999). After colliding with the baryons (of total mass M_B), characterized by the baryon load parameter $B = M_B c^2 / E_{e^+e^-}$, the optically thick plasma keeps accelerating until reaching transparency and emitting a proper gamma-ray burst (P-GRB, see Ruffini et al. 2000). The accelerated baryons then interact with the circumburst medium (CBM) clouds (Ruffini et al. 2001b); the equation of motion of the plasma has been integrated leading to results which differ from the ones of the Blandford & McKee (1976) self-similar solution (see Bianco & Ruffini 2004, 2005a,b, 2006). By using Eq. (2) defining the “equitemporal surfaces” (see Bianco et al. 2001; Bianco & Ruffini 2004, 2005a,b, 2006) it has been possible to infer the structure of the gamma-ray spikes in the prompt emission, which for the most part has been applied to the case of BdHNe (see, e.g., Ruffini et al. 2002; Bernardini et al. 2005; Patricelli et al. 2012; Izzo et al. 2012; Penacchioni et al. 2012, 2013; Ruffini et al. 2016b). For typical baryon loads $10^{-4} \lesssim B \lesssim 10^{-2}$ leading to Lorentz gamma factors $\Gamma \approx 10^2\text{--}10^3$ at transparency for the e^+e^- -baryon plasma, characteristic distances from the BH of $\approx 10^{15}\text{--}10^{17} \text{ cm}$ have been derived (see, e.g., Ruffini et al. 2016a, and references therein). Those procedures are further generalised in this paper to compute the propagation of the e^+e^- through the SN ejecta (see Sec. 10), after having computed their density profiles (see Fig. 35) and the corresponding baryon load (see Fig. 34). The equations have been integrated all the way up to reaching the condition of transparency (see Figs. 36 and 37).

3.6. Episode 3: the ongoing research on the gamma-ray flares, afterglow and GeV emission

We have exemplified the necessary steps in the analysis of each episode which include: to determine the physical nature of each episode, the corresponding world-line with the specific time-dependent Lorentz gamma factor and so determining, using Eq. (2), the arrival time at the detector which has to agree, for consistency, with the one obtained from the observations. This program is applied in this article specifically for the analysis of early X-ray flares (see Sec. 8 and 9). We will follow the same procedures for: 1) the more complex analysis of gamma-ray flares, 2) the analysis of the afterglow consistent with the constraints on the X-ray flares observations, and 3) the properties of the GeV emission, common to BdHNe and S-GRBs (Ruffini et al. 2015b, 2016b). Having established the essential observational and theoretical background in Secs. 2 and 3, we proceed to the data analysis of the early X-ray flares (see Secs. 4–10).

4. THE EARLY FLARES AND SAMPLE SELECTION

With the increase in the number of observed GRBs, an attempt was made to analyze the X-ray flares and other processes considered to be similar in the observer reference frame, independent of the nature of the GRB type and of the value of their cosmological redshift or the absence of such a value. This goal of this attempt was to identify their “standard” properties, following a statistical analysis methodology often applied in classical astronomy (see Chincarini et al. 2007; Falcone et al. 2007; Margutti et al. 2010 as well as the review articles Piran 1999, 2004; Mészáros 2002, 2006; Berger 2014; Kumar & Zhang 2015). We now summarize our alternative approach, having already given in the introduction and in Sec. 2 and 3 the background for the observational identification and the theoretical interpretation of the X-ray flares.

As a first step, we only consider GRBs with an observed cosmological redshift. Having ourselves proposed the classification of all GRBs into seven different subclasses (see Sec. 3), we have given preliminary attention to verifying whether X-ray flares actually occur preferentially in some of these subclasses and if so, to identify the physical reasons determining such a correlation. We have analyzed all X-ray flares and found, a posteriori, that X-ray flares only occur in BdHNe. No X-ray flare has been identified in any other GRB subclass, either long or short. A claim of their existence in short bursts (Barthelmy et al. 2005; Fan et al. 2005; Dai et al. 2006) has been superseded: GRB 050724 with $T_{90} \sim 100$ s is not a short GRB, but actually a GRF, expected to originate in the merging of a neutron star and a white dwarf (see Fig. 4), the X-ray data for this source from XRT is sufficient to assert that there is no evidence of an X-ray flare as defined in this section. GRB 050709 is indeed a short burst. It has been classified as S-GRF (Aimurатов et al. 2017), and has been observed by HETE with very sparse X-ray data (Butler et al. 2005), and no presence of an X-ray flare can be inferred; the Swift satellite pointed at this source too late, 38.5 hours after the HETE trigger (Morgan et al. 2005).

As a second step, since all GRBs have a different redshift z , in order to compare them we need a description of each one of them in its own cosmological rest frame. The luminosities have to be estimated after doing the necessary K-corrections and the time coordinate in the observer frame has to be corrected by the cosmological redshift $t_a^d = (1+z)t_a$. This also affects the determination of the T_{90} of each source (see e.g. Fig. 38 in Sec. 11 where the traditional approach by Kouveliotou et al. (1993); Bromberg et al. (2013) has been superseded by ours).

As a third step, we recall an equally important distinction from the traditional fireball approach with a single ultra relativistic jetted emission. Our GRB analysis envisages the existence of different episodes within each GRB, each one characterized by a different physical process and needing the definition of its own world-line and corresponding gamma factors, essential for estimating the time parametrization in the rest-frame of the observer (see Sec. 2).

These three steps are applied in the present article, which specifically addresses the study of the early X-ray flares and their fundamental role in establishing the physical and astrophysical nature of BdHNe and in distinguishing our binary model from the traditional one.

Before proceeding let us recall the basic point of the K-correction. All the observed GRBs have a different redshift. In order to compare them it is necessary to refer each one of them to its cosmological rest frame. This step has often been neglected in the current literature (Chincarini et al. 2007; Falcone et al. 2007; Margutti et al. 2010). Similarly, for the flux observed by the above satellites in Sec. 2, each instrument is characterized by its fixed energy window $[\epsilon_{obs,1}; \epsilon_{obs,2}]$. The observed flux f_{obs} , defined as the energy per unit area and time in a fixed instrumental energy window $[\epsilon_{obs,1}; \epsilon_{obs,2}]$, is expressed in terms of the observed photon number spectrum n_{obs} (i.e., the number of observed

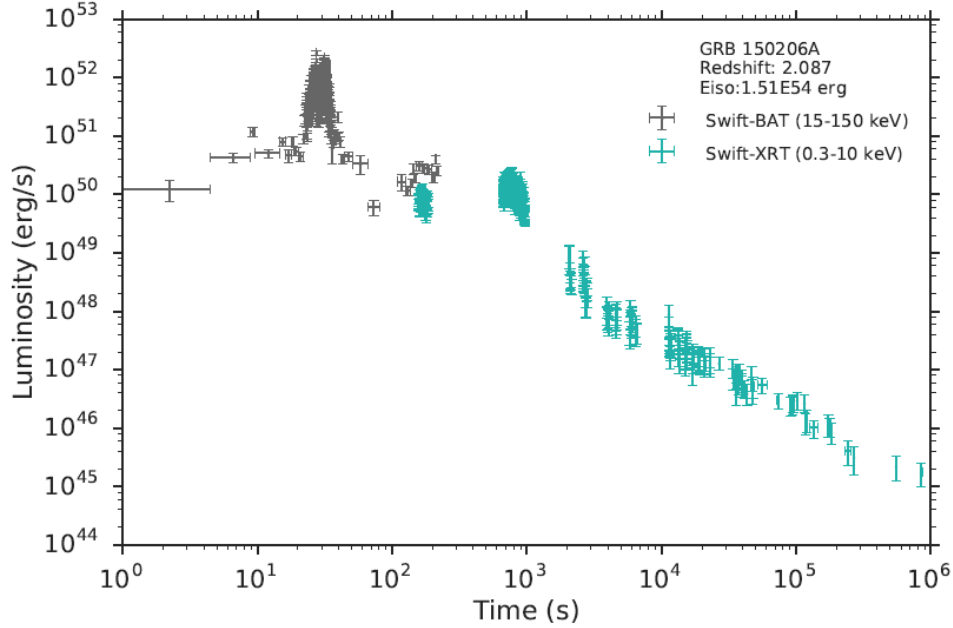


Figure 5. GRB 150206A is an example of a GRB with incomplete data, which therefore must be excluded. It only has 30 Swift-*XRT* observations in the early 300 s. The flare determination is not possible under these conditions.

photons per unit energy, area and time) as

$$f_{obs, [\epsilon_{obs,1}; \epsilon_{obs,2}]} = \int_{\epsilon_{obs,1}}^{\epsilon_{obs,2}} \epsilon n_{obs}(\epsilon) d\epsilon. \quad (3)$$

It then follows that the luminosity L of the source (i.e., the total emitted energy per unit time in a given bandwidth), expressed by definition in the source cosmological rest frame, is related to f_{obs} through the luminosity distance $D_L(z)$:

$$L_{[\epsilon_{obs,1}(1+z); \epsilon_{obs,2}(1+z)]} = 4\pi D_L^2(z) f_{obs, [\epsilon_{obs,1}; \epsilon_{obs,2}]} . \quad (4)$$

The above Eq.(4) gives the luminosities in different cosmological rest frame energy bands, depending on the source redshift. To express the luminosity L in a fixed cosmological rest frame energy band, e.g., $[E_1; E_2]$, common to all sources, we can rewrite Eq.(4) as:

$$L_{[E_1; E_2]} = 4\pi D_L^2 f_{obs, [\frac{E_1}{1+z}; \frac{E_2}{1+z}]} = 4\pi D_L^2 k[\epsilon_{obs,1}; \epsilon_{obs,2}; E_1; E_2; z] f_{obs, [\epsilon_{obs,1}; \epsilon_{obs,2}]} , \quad (5)$$

where we have defined the K-correction factor:

$$k[\epsilon_{obs,1}; \epsilon_{obs,2}; E_1; E_2; z] = \frac{f_{obs, [\frac{E_1}{1+z}; \frac{E_2}{1+z}]} }{f_{obs, [\epsilon_{obs,1}; \epsilon_{obs,2}]}} = \frac{\int_{\frac{E_1}{1+z}}^{\frac{E_2}{1+z}} \epsilon n_{obs}(\epsilon) d\epsilon}{\int_{\epsilon_{obs,1}}^{\epsilon_{obs,2}} \epsilon n_{obs}(\epsilon) d\epsilon} . \quad (6)$$

If the energy range $[\frac{E_1}{1+z}; \frac{E_2}{1+z}]$ is not fully inside the instrumental energy band $[\epsilon_{obs,1}; \epsilon_{obs,2}]$, It may well happen that we need to extrapolate n_{obs} within the integration boundaries $[\frac{E_1}{1+z}; \frac{E_2}{1+z}]$.

Finally we express each luminosity in a rest frame energy band which coincides with the energy window of each specific instrument.

We turn now to the selection procedure for the early X-ray flares. We take the soft X-ray flux light curves of each source with known redshift from the Swift-*XRT* repository (Evans et al. 2007, 2009). We then apply the above K-correction to obtain the corresponding luminosity light curves in the rest frame 0.3–10 keV energy band. Starting from 421 Swift-*XRT* light curves, we found in 50 sources X-ray flare structures in the early 200 s. Remarkably, all of them are in BdHNe. We further filter our sample by applying the following criteria:

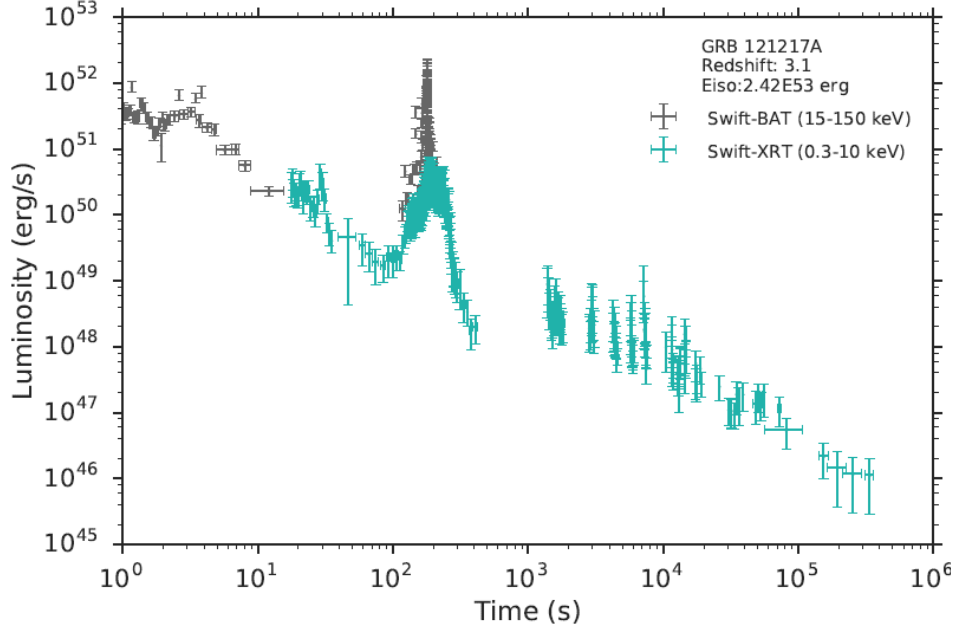


Figure 6. GRB 121217A clearly shows a gamma-ray flare observed by Swift-BAT which coincides with a soft X-ray component observed by Swift-XRT. From the spectral analysis, it has a soft power-law photon index, and most of the energy deposited in high energy gamma-rays. This is an indication that the soft X-ray component is likely the low energy part of a gamma-ray flare. For these reasons, we neglect it in our sample.

1. We exclude GRBs with flares having low (< 20) signal to noise ratio (SNR), or with an incomplete data coverage of the early X-ray light curve — 14 GRBs are excluded (see e.g., Fig. 5).
2. We consider only X-ray flares and do not address here the gamma-ray flares which will be studied in a forthcoming article — 8 GRBs having only gamma-ray flares are temporarily excluded (see e.g., Fig. 6). In Fig. 7 we show an illustrative example of the possible co-existence of a X-ray flare and a gamma-ray flare, and a way to distinguish them.
3. We also neglect here the late X-ray flare, including the ultra-long GRB, which will be discussed in a forthcoming paper — 6 GRBs are consequently excluded.
4. We neglect the GRBs for which the soft X-ray energy observed by Swift-XRT (0.3 – 10 keV) before the plateau phase is higher than the gamma-ray energy observed by Swift-BAT (15 – 150 keV) during the entire valid Swift-BAT observation. This Swift-BAT anomaly points to an incomplete coverage of the prompt emission – 6 GRBs are excluded (see e.g., Fig. 8).

Finally, we have found 16 BdHNe satisfying all the criteria to be included in our sample. Among them, 7 BdHNe show a single flare. The other 9 BdHNe contain two flares: generally we exclude the first one, which appears to be a component from the gamma-ray spike or gamma-ray flare, and therefore select the second one for analysis (see, e.g., Fig. 7).

These 16 selected BdHNe cover a wide range of redshifts. The closest one is GRB 070318 with redshift $z = 0.84$, and the farthest one is GRB 090516A with redshift $z = 4.11$. Their isotropic energy is also distributed over a large range: 5 GRBs have energies of the order of 10^{52} erg, 9 GRBs of the order of 10^{53} erg, and 2 GRBs have extremely high isotropic energy $E_{iso} > 10^{54}$ erg. Therefore, this sample is well-constructed although the total number is limited.

5. THE XRT LUMINOSITY LIGHT CURVES OF THE 16 BDHN SAMPLE

We now turn to the light curves of each one of the 16 GRBs composing our sample (see Figs. 9–24). Blue curves represent the X-rays observed by Swift-XRT, and green curves are the corresponding optical observations when available.

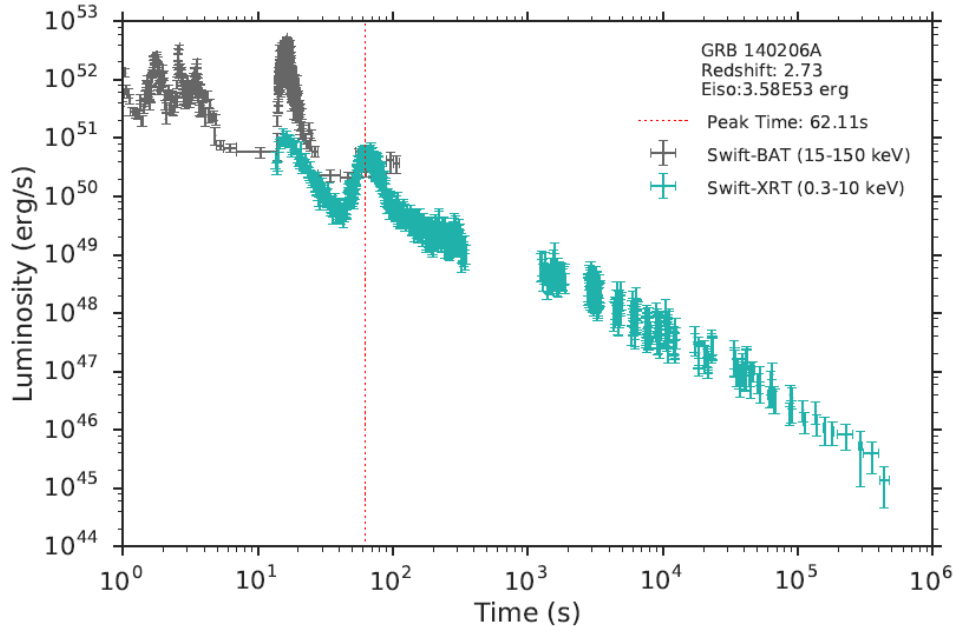


Figure 7. GRB 140206A has two flares. A gamma-ray flare coincides with the first flare while it is dim in the second one. The spectral analysis, using both Swift-XRT and Swift-BAT data, indicates a power-law index -0.88 ± 0.03 for the first flare. While the second flare requires an additional blackbody component; its power-law index is -1.73 ± 0.06 and its blackbody temperature is 0.54 ± 0.07 keV. Clearly, the energy of the first flare is contributed mainly by gamma-ray photons—it is a gamma-ray flare, and the second flare is an X-ray flare that we consider in this article.

All the values are in the rest-frame and the X-ray luminosities have been K-corrected. The red vertical lines indicate the peak time of the X-ray flares. The rest-frame luminosity light curves of some GRBs show different flare structures compared to the observed count flux light-curves. An obvious example is GRB 090516A, as follows by comparing Fig. 18 in this paper with Fig. 1 in Troja et al. (2015). The details of the FPA, as well as their correlations or absence of correlation with E_{iso} , are given in the next section.

We then conclude that in our sample, there are Swift data for all the GRBs, *Konus-Wind* observed GRB 080607, 080810, 090516A, 131030A, 140419A, 141221A and 151027A while Fermi detected GRB 090516A, 140206, 141221A, 151027A. The energy coverage of the available satellites is limited, as mentioned in Sec. 2: Fermi detects the widest photon energy band, from 8 keV to 300 GeV, *Konus-Wind* observes from 20 keV to 15 MeV, Swift-BAT has a narrow coverage from 15 keV to 150 keV. No GeV photons were observed, though GRB 090516A and 151027 were in the Fermi-LAT field of view. This contrasts with the observations of S-GRBs for which, in all of the sources so far identified and within the Fermi-LAT field of view, GeV photons were always observed (Ruffini et al. 2016b,a) and can always freely reach a distant observer. These observational facts suggest that NS-NS (or NS-BH) mergers leading to the formation of a BH leave the surrounding environment poorly contaminated by the material ejected in the merging process ($\lesssim 10^{-2}$ – $10^{-3} M_{\odot}$) and therefore the GeV emission, originating from accretion on the BH formed in the merger process (Ruffini et al. 2016b) can be observed. On the other hand, BdHNe originate in CO_{core}-NS binaries in which the material ejected from the CO_{core} explosion ($\approx M_{\odot}$) greatly pollutes the environment where the GeV emission has to propagate to reach the observer (see Sec. 3). This together with the asymmetries of the SN ejecta (see Sec. 3 and Becerra et al. 2016) lead to the possibility that the GeV emission in BdHNe can be “obscured” by the material of the SN ejecta, explaining the absence of GeV photons in the above cases of GRB 090516A and 151027.

We derive the isotropic energy E_{iso} by assuming the prompt emission to be isotropic and by integrating the prompt photons in the rest-frame energy range from 1 keV to 10 MeV (Bloom et al. 2001). None of the satellites is able to cover the entire energy band of E_{iso} , so we need to fit the spectrum and find the best-fit function, then extrapolate the integration of energy by using this function. This method is relatively safe for GRBs observed by Fermi and *Konus-Wind*, but 6 GRBs in our sample have been observed only by Swift, so we uniformly fit and extrapolate these

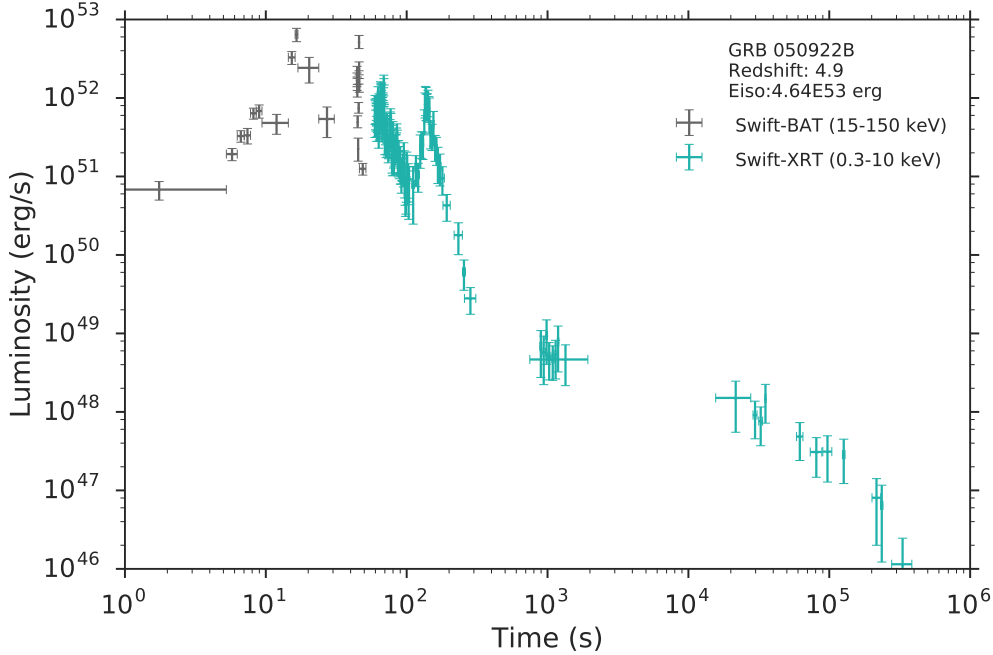


Figure 8. The Swift-BAT data of GRB 050922B has poor resolution, it cannot provide valid information after 50 s; the energy observed in its energy band 15–150 keV during this 50 s duration is 1.19×10^{53} erg. The energy observed by Swift-XRT is higher; the energy of the flares (60 – 200 s) in the Swift-XRT band 0.3–10 keV is 3.90×10^{53} erg. These results imply that the Swift-BAT observations may not cover the entire prompt emission phase; the isotropic energy computed from the Swift-BAT data is not reliable, and consequently the Swift-XRT observed partial prompt emission which brings complexity to the X-ray light-curve makes the identification of the authentic X-ray flare more difficult.

6 GRBs by power-laws and cutoff power-laws; then we take the average value as E_{iso} . In general, our priority in computing E_{iso} is Fermi, Konus-Wind, then Swift. In order to take into account the expansion of the universe, all of our computations consider K-correction. The formula of K-correction for E_{iso} varies depending on the best-fit function. The energy in the X-ray afterglow is computed in the cosmological rest-frame energy band from 0.3 keV to 10 keV. We smoothly fit the luminosity light-curve using an algorithm named locally weighted regression (Cleveland & Devlin 1988) which provides a sequence of power-law functions. The corresponding energy in a fixed time interval is obtained by summing up all of the integrals of the power-laws within it. This method is applied to estimate the energy of the flare E_f , as well as the energy of the FPA phase up to 10^9 s, E_{FPA} . An interesting alternative procedure was used in Swenson & Roming (2014) to fit the light-curve and determine the flaring structure with a Bayesian Information method. On this specific aspect the two treatments are equally valid and give compatible results.

Tab. 3 contains the relevant energy and time information of the 16 BdHNe of the sample: the cosmological redshift z , E_{iso} , the flare peak time t_p , the corresponding peak luminosity L_p , the flare duration Δt , and the energy of the flare E_f . To determine t_p we apply a locally weighted regression, which results in a smoothed light-curve composed of power-law functions: the flare peak is localized where the power-law index is zero. Therefore t_p is defined as the time interval between the flare peak and the trigger time of *Swift*-BAT². Correspondingly, we find the peak luminosity L_p at t_p and its duration Δt which is defined as the time interval between a start time and an end time at which the luminosity is half of L_p . We have made public the entire details including the codes online³.

6. STATISTICAL CORRELATION

We then establish correlations between the above quantities characterizing each luminosity light curve of the sample with the E_{iso} of the corresponding BdHN. We have relied heavily on the Markov chain Monte Carlo (MCMC) method

² In reality, the GRB occurs earlier than the trigger time, since there is a short period when the flux intensity is lower than the satellite trigger threshold (Fenimore et al. 2003)

³ <https://github.com/YWangScience/AstroNeuron>

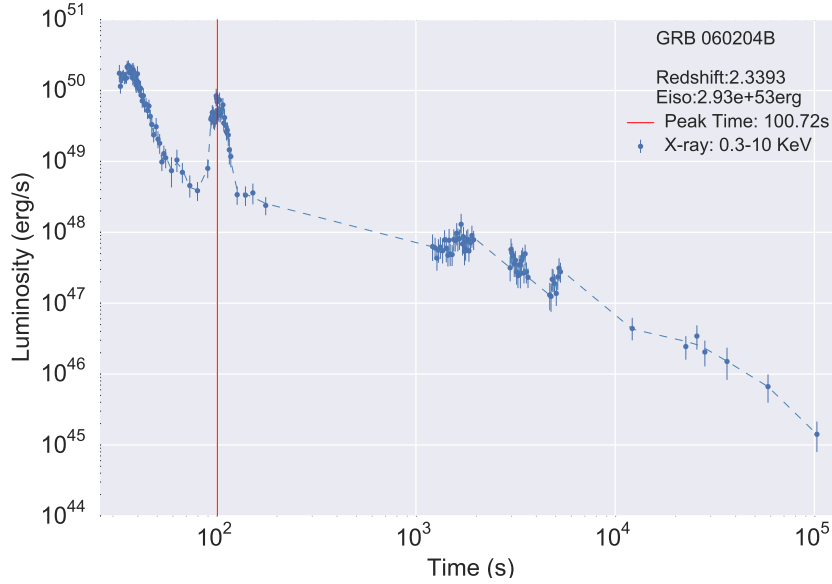


Figure 9. 060204B: this GRB was triggered by Swift-BAT (Falcone et al. 2006); Swift-XRT began observing 28.29 sec after the BAT trigger. There is no observation from the Fermi satellite. X-shooter found its redshift at 2.3393 based on the host galaxy (Perley et al. 2016). The isotropic energy of this GRB reaches 2.93×10^{53} erg computed from Swift-BAT data.

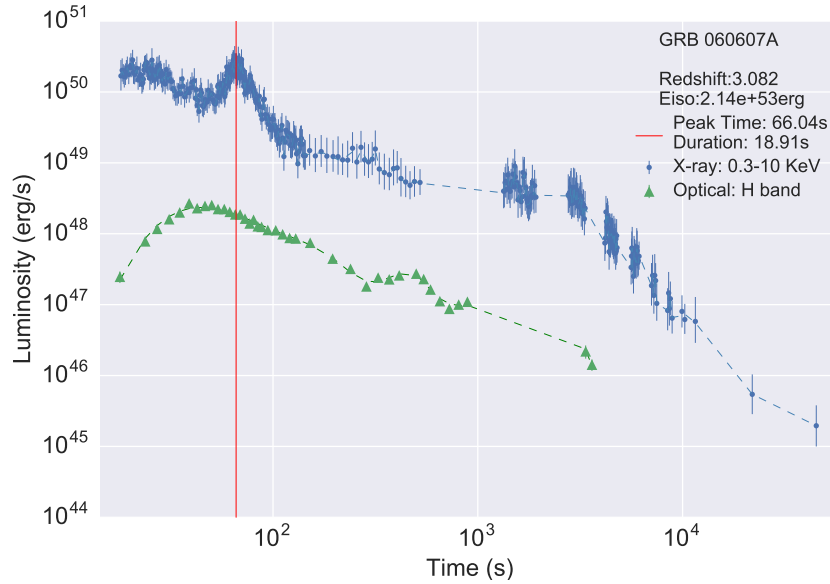


Figure 10. 060607A: this source has been detected by the Swift satellite (Ziaepour et al. 2006). It has a bright optical counterpart (Ziaepour et al. 2006). It is located at a redshift $z = 3.082$ (Ledoux et al. 2006). The prompt light curve presents a doubled-peaked emission that lasts around 10 s, plus a second emission at ~ 25 s of 2.5 s duration. The isotropic energy is $E_{iso} = 2.14 \times 10^{53}$ erg. Optical data is from Nysewander et al. (2009)

and iterated 10^5 times for having the best fit of the power-law and their correlation coefficient. The main results are summarized in Figs. 25–28. All the codes are publicly available online⁴. We conclude that the peak time and the duration of the flare, as well as the peak luminosity and the total energy of flare, are highly correlated with E_{iso} , with

⁴ <https://github.com/YWangScience/MCCC>

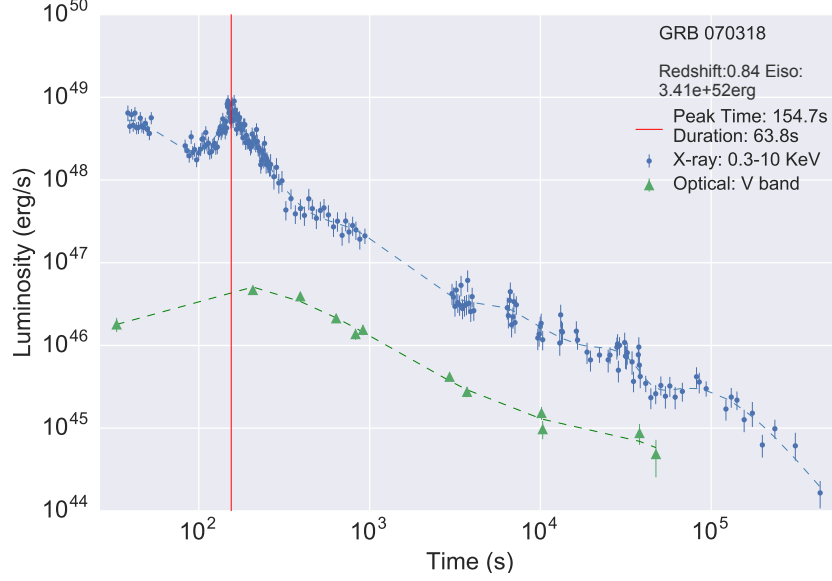


Figure 11. 070318: this source has been detected by the Swift satellite (Cummings et al. 2007). It has a spectroscopic redshift of $z = 0.836$ (Jaunsen et al. 2007). The prompt light curve shows a peak with a typical fast-rise exponential-decay (FRED) behavior lasting about 55 s. XRT began observing the field 35 s after the BAT trigger. The isotropic energy is $E_{iso} = 3.64 \times 10^{52}$ erg. From the optical observation at ~ 20 days, no source or host galaxy is detected at the position of the optical afterglow, indicating that the decay rate of the afterglow must have steepened after some hours (Cobb 2007). Its optical data is from Chester et al. (2008)

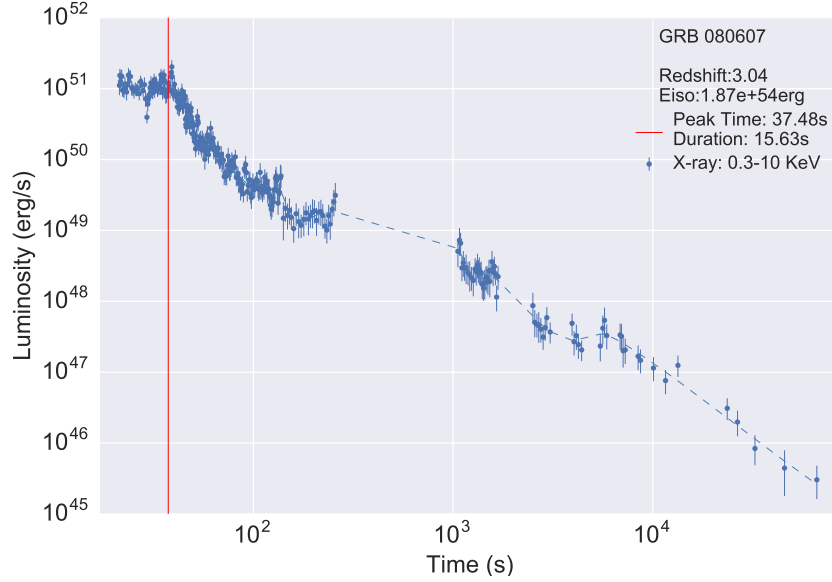


Figure 12. 080607: this source has been observed by AGILE (Marisaldi et al. 2008), Konus-Wind (Golenetskii et al. 2008) and Swift (Mangano et al. 2008). UVOT detected only a faint afterglow, since the source is located at a redshift $z = 3.04$. The isotropic energy is $E_{iso} = 1.87 \times 10^{54}$ erg. The BAT prompt light curve shows a very pronounced peak that lasts ~ 10 s, followed by several shallow peaks until 25 s. The Swift localization is at about 113° off-axis with respect to the AGILE pointing, so well out of the field of view of the AGILE gamma-ray imaging detector (GRID), which does not show any detection. The Konus-Wind light curve in the 50–200 keV range shows a multiple peak emission lasting 15 s.

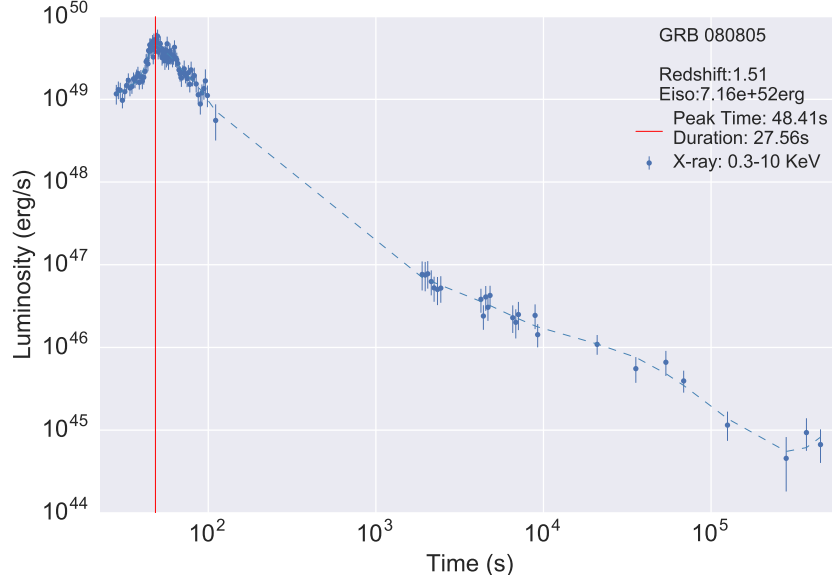


Figure 13. 080805: this source was detected by *Swift* (Pagani et al. 2008). The prompt light curve shows a peak with a FRED behavior lasting about 32 s. The redshift is $z = 1.51$, as reported by VLT (Jakobsson et al. 2008), and the isotropic energy is $E_{iso} = 7.16 \times 10^{52}$ erg.

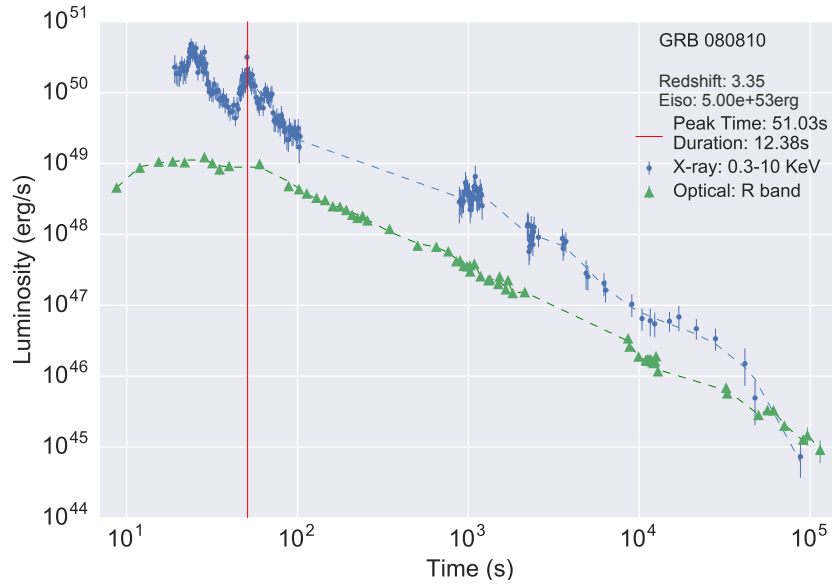


Figure 14. 080810: this source was detected by *Swift* (Golenetskii et al. 2008). The BAT light curve shows a multiple-peaked structure lasting about 23 s. XRT began observing the field 76 s after the BAT trigger. The source is located at a redshift of $z = 3.35$ and has an isotropic energy $E_{iso} = 3.55 \times 10^{53}$ erg. Optical data is taken from Page et al. (2009).

correlation coefficients larger than 0.6 (or smaller than -0.6). The average values and the $1-\sigma$ uncertainties are shown in Tab. 4.

7. THE PARTITION OF ELECTRON-POSITRON PLASMA ENERGY BETWEEN THE PROMPT EMISSION AND THE FPA

The energy of the prompt emission is proportional to E_{iso} if and only if spherical symmetry is assumed: this clearly follows from the prompt emission time integrated luminosity. We are now confronted with a new situation: the

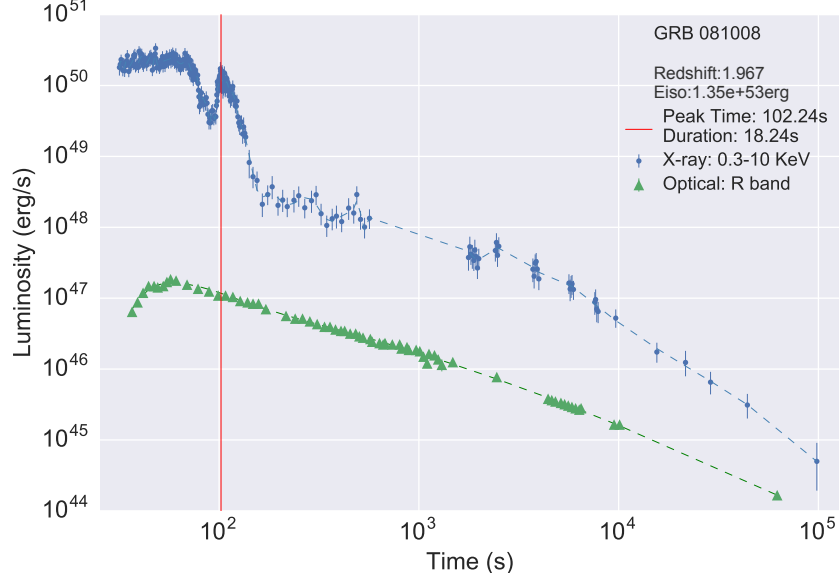


Figure 15. 081008: this source was detected by *Swift* (Racusin et al. 2008). The prompt emission lasts about 60 s and shows two peaks separated by 13 s. It is located at $z = 1.967$, as reported by VLT (D’Avanzo et al. 2008), and has an isotropic energy $E_{iso} = 1.07 \times 10^{53}$ erg. Optical data is from Yuan et al. (2010).

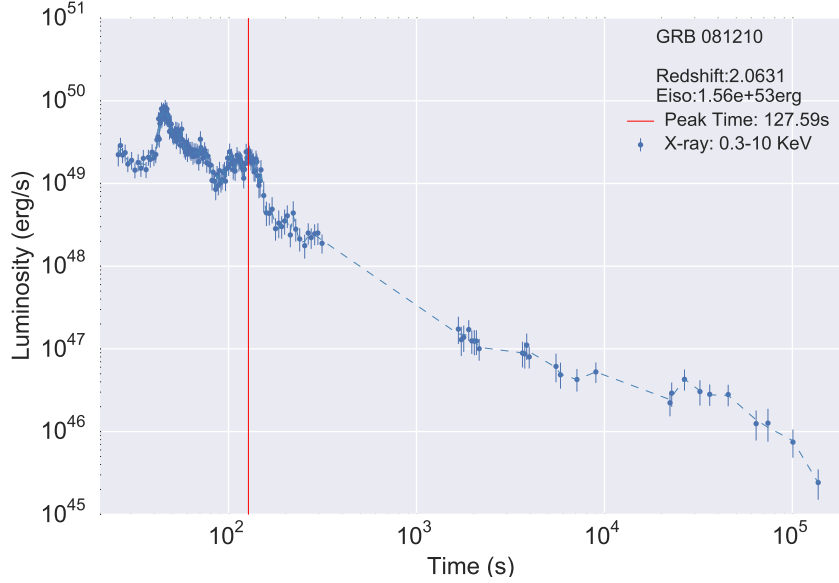


Figure 16. 081210: this GRB was detected by Swift-BAT (Krimm et al. 2008), Swift-XRT began observing at 23.49 s after the BAT trigger. The BAT light curve begins with two spikes with a total duration of about 10 s, and an additional spike at 45.75 s. There is no observation from the Fermi satellite. X-shooter found its redshift to be 2.0631 (Perley et al. 2016). The isotropic energy of this GRB is 1.56×10^{53} erg.

total energy of the FPA emission up to 10^9 s (E_{FPA}) is also proportional to E_{iso} , following the correlation given in Tabs. 5 and 6, and Fig. 29. What is clear is that there are two very different components where the energy of the dyadosphere $E_{e^+e^-}$ is utilized: the energy E_{prompt} of the prompt emission and the energy E_{FPA} of the FPA, i.e., $E_{e^+e^-} = E_{iso} = E_{prompt} + E_{FPA}$. Fig. 30 and Fig. 31 show the distribution of $E_{e^+e^-} = E_{iso}$ among these two components.

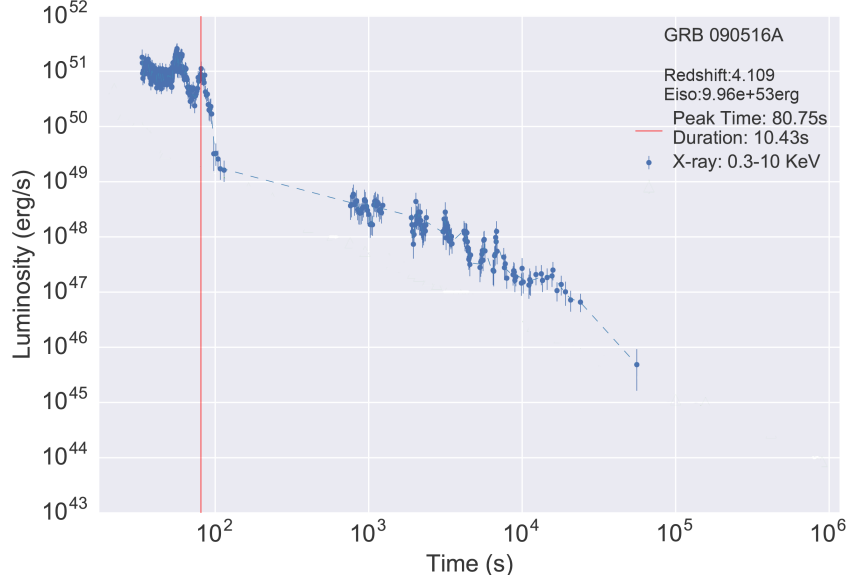


Figure 17. 090516A: this source was detected by Swift (Rowlinson et al. 2009), Konus Wind and Fermi/GBM (McBreen 2009). The BAT prompt light curve is composed of two episodes, the first starting 2 s before the trigger and lasting up to 10 s after the trigger, while the second episode starts at 17 s and lasts approximately 2 s. The GBM light curve consists of about five overlapping pulses from $T_{F,0} - 10$ s to $T_{F,0} + 21$ s (where $T_{F,0}$ is the trigger time of the *Fermi*/GBM). Konus-Wind observed this GRB in the waiting mode. VLT identified the redshift of the afterglow as $z = 4.109$ (de Ugarte Postigo et al. 2012), in agreement with the photometric redshift obtained with GROND (Rossi et al. 2009). Fermi-LAT was inside of the field of view, following the standard Fermi-LAT likelihood analysis in https://fermi.gsfc.nasa.gov/ssc/data/analysis/scitools/likelihood_tutorial.html, the upper limit of observed count flux is 4.76×10^{-6} photons $\text{cm}^{-2} \text{s}^{-1}$, no GeV photon was found for this high redshift and low observed fluence GRB. The isotropic energy is $E_{iso} = 6.5 \times 10^{53}$ erg.

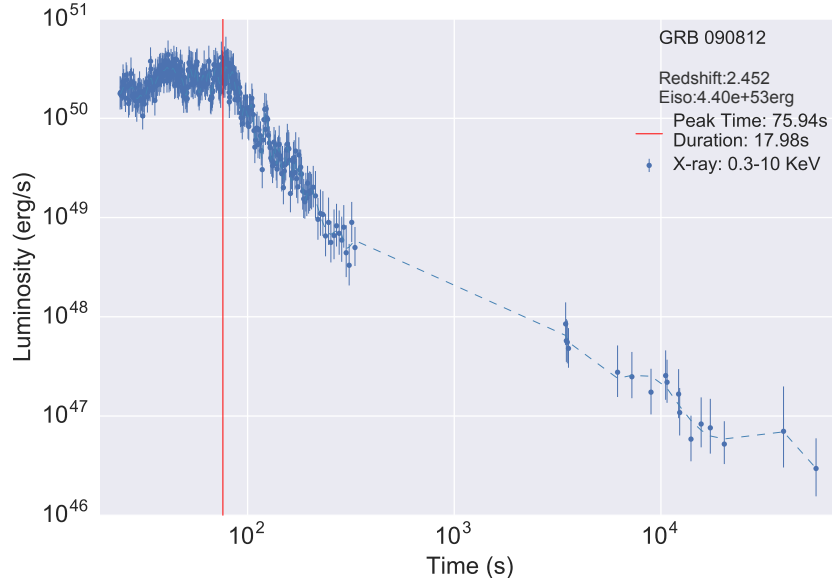


Figure 18. 090812: this source was detected by *Swift* (Stamatikos et al. 2009). It has a redshift $z = 2.452$ as confirmed by VLT (de Ugarte Postigo et al. 2012) and an isotropic energy $E_{iso} = 4.75 \times 10^{53}$ erg. The BAT light curve shows three successive bumps lasting ~ 20 s in total. XRT began observing the field 22 s after the BAT trigger (Stamatikos et al. 2009). The BAT light curve shows a simple power-law behavior.

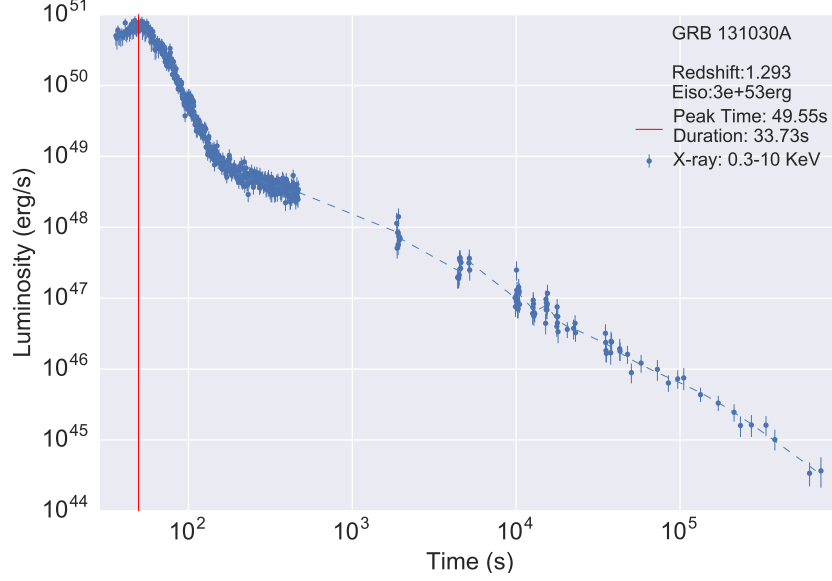


Figure 19. 131030A: this source was observed by *Swift* (Troja et al. 2013) and Konus-Wind (Golenetskii et al. 2013). The BAT light curve shows two overlapping peaks starting, with respect to the Swift-BAT trigger $T_{B,0}$, at $\sim T_{B,0} - 3.5$ s and peaking at $\sim T_{B,0} + 4.4$ s (Barthelmy et al. 2013). The duration is 18 s in the 15–350 keV band. The Konus-Wind light curve shows a multi-peaked pulse from $\sim T_{KW,0} - 1.3$ s till $\sim T_{KW,0} + 11$ s (where $T_{KW,0}$ is the Konus-Wind trigger time). The redshift of this source is $z = 1.293$, as determined by NOT (Xu et al. 2013). The isotropic energy is $E_{iso} = 3 \times 10^{53}$ erg.

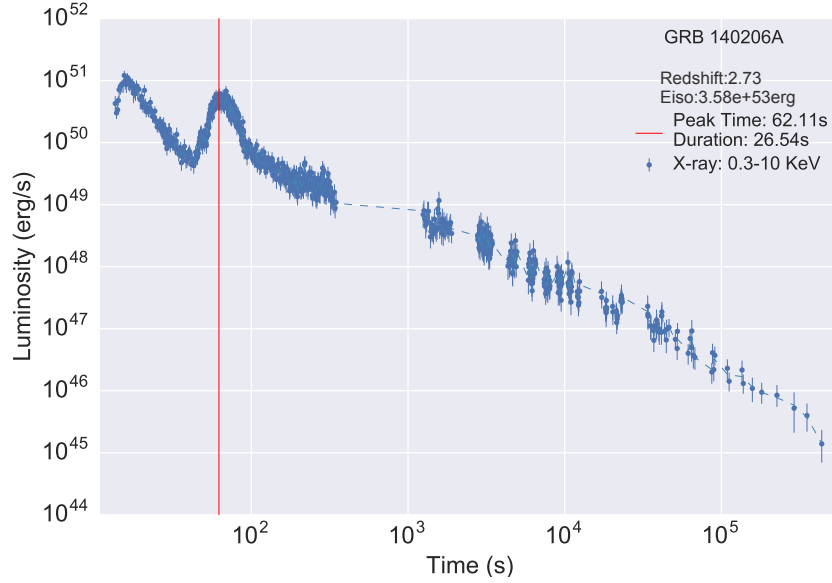


Figure 20. 140206A: this source was detected by all the instruments onboard *Swift* (Lien et al. 2014) and by Fermi/GBM (von Kienlin & Bhat 2014). The GBM light curve shows a single pulse with a duration of ~ 7 s (50–300 keV). The source was outside of the field of view, 123° from the LAT bore-sight at the time of the trigger. The BAT light curve shows a multi-peaked structure with roughly three main pulses (Sakamoto et al. 2014). The source duration in the 15–350 keV band is 25 s. The redshift, as observed by NOT (Malesani et al. 2014) is $z = 2.73$, and the isotropic energy is $E_{iso} = 4.3 \times 10^{53}$ erg.

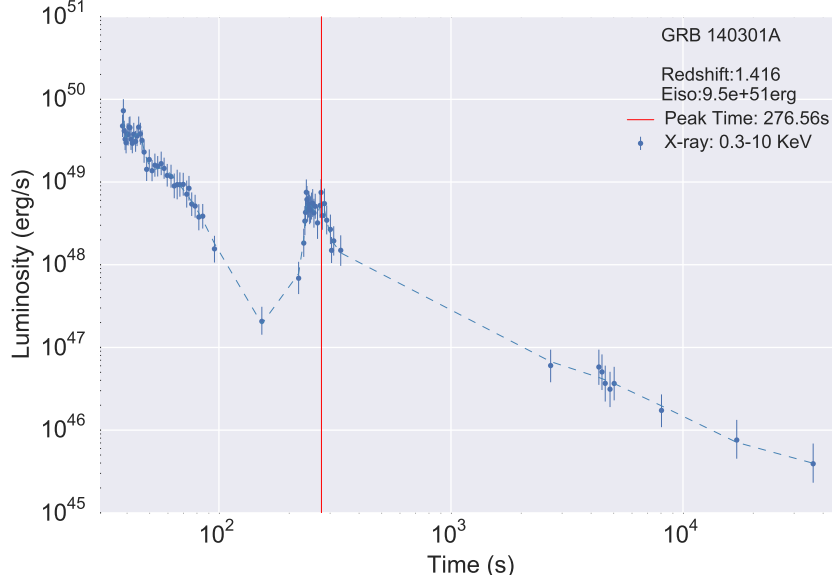


Figure 21. 140301A: this GRB was triggered by Swift-BAT (Page et al. 2014); the BAT light-curve has a single spike with a duration of about 4 s. XRT started to observe 35.63 s after the BAT trigger. There is no observation from the Fermi satellite. From the X-shooter spectrum analysis, redshift was revealed at 1.416 (Kruehler et al. 2014). The isotropic energy of this GRB is 9.5×10^{51} erg.

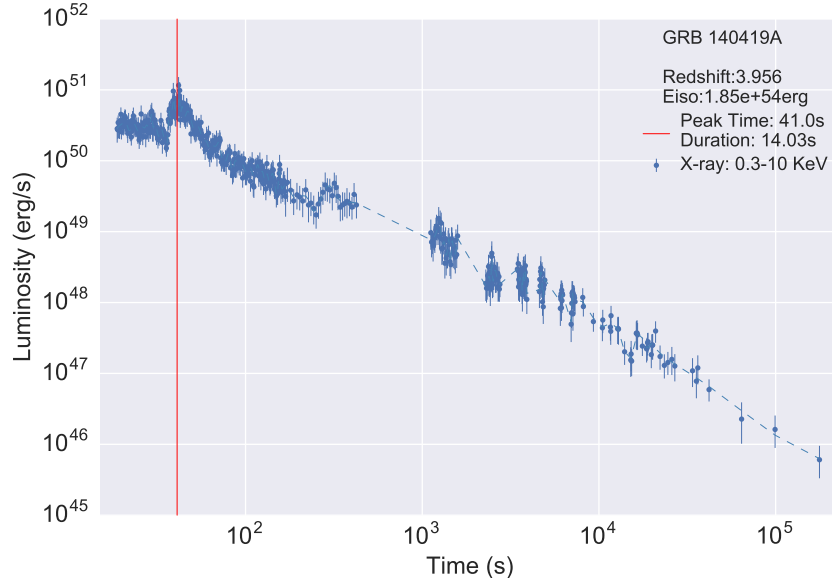


Figure 22. 140419A: this source was detected by Konus Wind (Golenetskii et al. 2014) and Swift (Marshall et al. 2014). The Konus Wind light curve shows a broad pulse from $\sim T_{\text{KW},0} - 2$ s to $\sim T_{\text{KW},0} + 8$ s, followed by softer pulses around $\sim T_{\text{KW},0} + 10$ s. The total duration of the burst is ~ 16 s. The BAT light curve shows two slightly overlapping clusters of peaks, starting at $\sim T_{\text{B},0} - 2$ s, peaking at $\sim T_{\text{B},0} + 2$ s and $\sim T_{\text{B},0} + 10$ s, and ending at $\sim T_{\text{B},0} + 44$ s (Baumgartner et al. 2014). The total duration (in the 15–350 keV) is 19 s. The redshift of this source, as determined by Gemini, is $z = 3.956$ (Tanvir et al. 2014) and its isotropic energy is $E_{\text{iso}} = 1.85 \times 10^{54}$ erg.

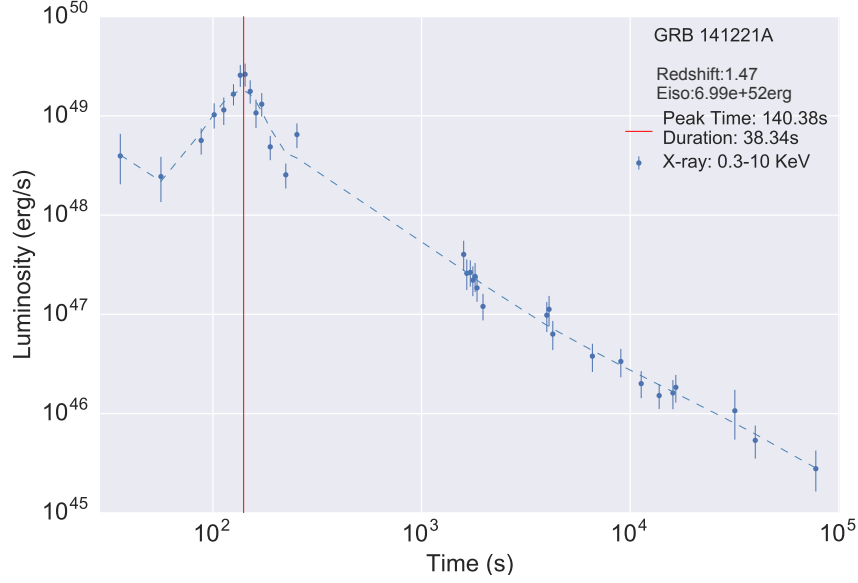


Figure 23. 141221A: this source is located at a spectroscopic redshift $z = 1.47$, as determined by Keck (Perley et al. 2014). Its isotropic energy is $E_{iso} = 1.91 \times 10^{52}$ erg. The emission was detected by all the instruments onboard Swift (Sonbas et al. 2014) and by Fermi/GBM (Yu 2014). The GBM light curve consists of two pulses with a duration of about 10 s (50–300 keV). The source was 76° from the LAT boresight at the time of the trigger, out of the field of view. The BAT light curve showed a double-peaked structure with a duration of about 8 s. XRT began observing the field 32 s after the BAT trigger.

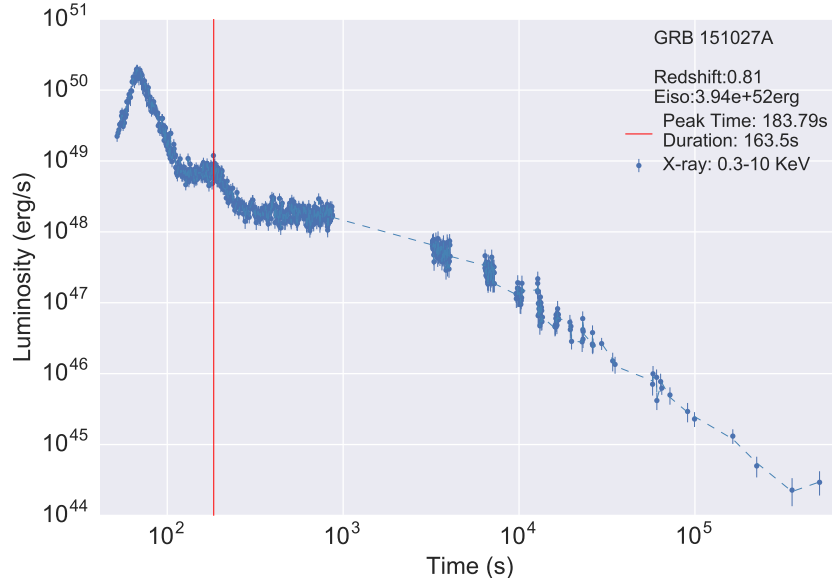


Figure 24. 151027A: this source was detected by MAXI (Masumitsu et al. 2015), Konus-Wind (Golenetskii et al. 2015), Swift (Maselli et al. 2015) and Fermi/GBM (Toelge et al. 2015). It is located at a redshift $z = 0.81$, as determined by Keck/HIRES (Perley et al. 2015), and the isotropic energy is $E_{iso} = 3.94 \times 10^{52}$ erg. The LAT boresight of the source was 10° at the time of the trigger, there are no clear associated high energy photons; an upper limit of observed count flux is computed as 9.24×10^{-6} photons $\text{cm}^{-2} \text{s}^{-1}$ following the standard Fermi-LAT likelihood analysis. The BAT light curve showed a complex peaked structure lasting at least 83 seconds. XRT began observing the field 48 s after the BAT trigger. The GBM light curve consists of three pulses with a duration of about 68 s in the 50–300 keV band. The Konus-Wind light curve consists of at least three pulses with a total duration of ~ 66 s. The MAXI detection is not significant, but the flux is consistent with the interpolation from the *Swift*/XRT light curve.

GRB	z	T_{90} (s)	E_{iso} (erg)	t_p (s)	L_p (erg/s)	Δt (s)	E_f (erg)	α_f
060204B	2.3393	40.12	$2.93(\pm 0.60) \times 10^{53}$	100.72 ± 6.31	$7.35(\pm 2.05) \times 10^{49}$	17.34 ± 6.83	$8.56(\pm 0.82) \times 10^{50}$	2.73
060607A	3.082	24.49	$2.14(\pm 1.19) \times 10^{53}$	66.04 ± 4.98	$2.28(\pm 0.48) \times 10^{50}$	18.91 ± 3.84	$3.33(\pm 0.32) \times 10^{51}$	1.72
070318	0.84	28.80	$3.41(\pm 2.14) \times 10^{52}$	154.7 ± 12.80	$6.28(\pm 1.30) \times 10^{48}$	63.80 ± 19.82	$3.17(\pm 0.37) \times 10^{50}$	1.84
080607	3.04	21.04	$1.87(\pm 0.11) \times 10^{54}$	37.48 ± 3.60	$1.14(\pm 0.27) \times 10^{51}$	15.63 ± 4.32	$1.54(\pm 0.24) \times 10^{52}$	2.08
080805	1.51	31.08	$7.16(\pm 1.90) \times 10^{52}$	48.41 ± 5.46	$4.66(\pm 0.59) \times 10^{49}$	27.56 ± 9.33	$9.68(\pm 1.24) \times 10^{50}$	1.25
080810	3.35	18.25	$5.00(\pm 0.44) \times 10^{53}$	51.03 ± 6.49	$1.85(\pm 0.53) \times 10^{50}$	12.38 ± 4.00	$1.80(\pm 0.17) \times 10^{51}$	2.37
081008	1.967	62.52	$1.35(\pm 0.66) \times 10^{53}$	102.24 ± 5.66	$1.36(\pm 0.33) \times 10^{50}$	18.24 ± 3.63	$1.93(\pm 0.16) \times 10^{51}$	2.46
081210	2.0631	47.66	$1.56(\pm 0.54) \times 10^{53}$	127.59 ± 13.68	$2.23(\pm 0.21) \times 10^{49}$	49.05 ± 6.49	$8.86(\pm 0.54) \times 10^{50}$	2.28
090516A	4.109	68.51	$9.96(\pm 1.67) \times 10^{53}$	80.75 ± 2.20	$9.10(\pm 2.26) \times 10^{50}$	10.43 ± 2.44	$7.74(\pm 0.63) \times 10^{51}$	3.66
090812	2.452	18.77	$4.40(\pm 0.65) \times 10^{53}$	77.43 ± 16.6	$3.13(\pm 1.38) \times 10^{50}$	17.98 ± 4.51	$5.18(\pm 0.61) \times 10^{51}$	2.20
131030A	1.293	12.21	$3.00(\pm 0.20) \times 10^{53}$	49.55 ± 7.88	$6.63(\pm 1.12) \times 10^{50}$	33.73 ± 6.55	$3.15(\pm 0.57) \times 10^{52}$	2.22
140206A	2.73	7.24	$3.58(\pm 0.79) \times 10^{53}$	62.11 ± 12.26	$4.62(\pm 0.99) \times 10^{50}$	26.54 ± 4.31	$1.04(\pm 0.59) \times 10^{51}$	1.73
140301A	1.416	12.83	$9.50(\pm 1.75) \times 10^{51}$	276.56 ± 15.50	$5.14(\pm 1.84) \times 10^{48}$	64.52 ± 10.94	$3.08(\pm 0.22) \times 10^{50}$	2.30
140419A	3.956	16.14	$1.85(\pm 0.77) \times 10^{54}$	41.00 ± 4.68	$6.23(\pm 1.45) \times 10^{50}$	14.03 ± 5.74	$7.22(\pm 0.88) \times 10^{51}$	2.32
141221A	1.47	9.64	$6.99(\pm 1.98) \times 10^{52}$	140.38 ± 5.64	$2.60(\pm 0.64) \times 10^{49}$	38.34 ± 9.26	$7.70(\pm 0.78) \times 10^{50}$	1.79
151027A	0.81	68.51	$3.94(\pm 1.33) \times 10^{52}$	183.79 ± 16.43	$7.10(\pm 1.75) \times 10^{48}$	163.5 ± 30.39	$4.39(\pm 2.91) \times 10^{51}$	2.26

Table 3. GRB sample properties of the prompt and flare phases. This table contains: the redshift z , the T_{90} in the rest frame, the isotropic energy E_{iso} , the flare peak time t_p in the rest frame, the flare peak luminosity L_p , the flare duration of which the starting and ending time correspond to half of the peak luminosity Δt , the flare energy E_f within the time interval Δt , and α_f power-law index from the fitting of the flare’s spectrum.

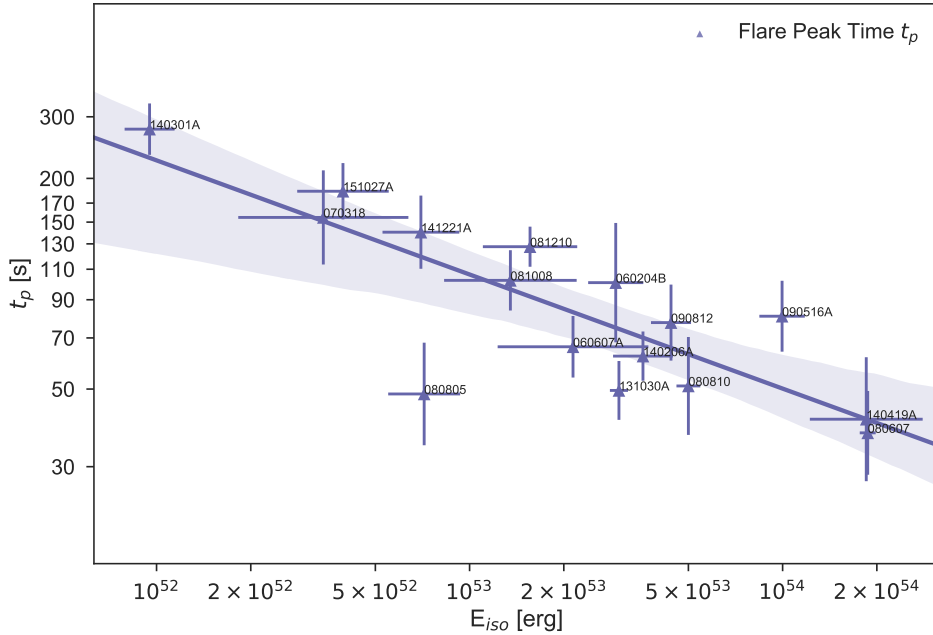


Figure 25. Relation between E_{iso} and t_p fit by a power-law. The shaded area indicates the 95% confidence level.

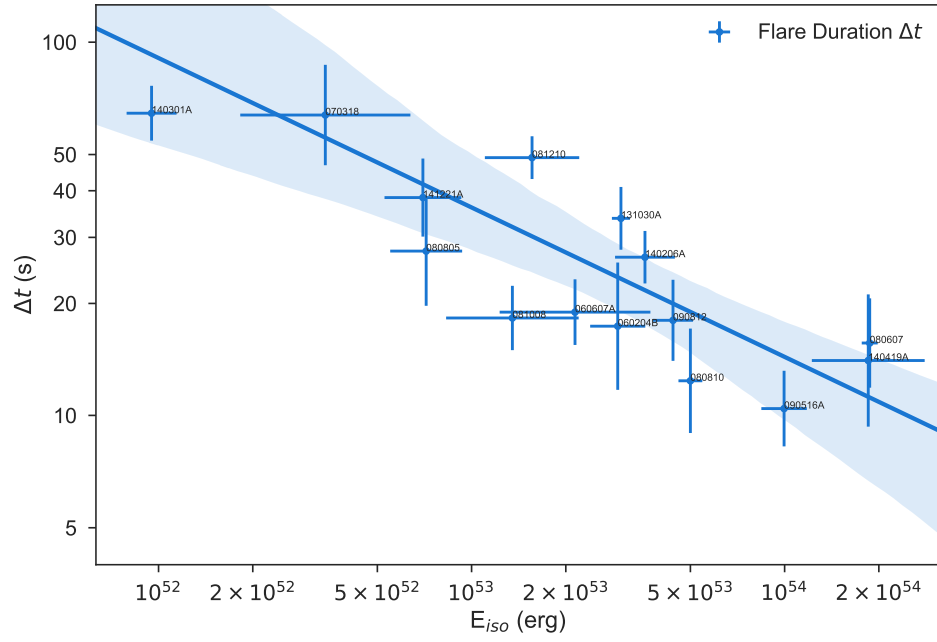


Figure 26. Relation between E_{iso} and Δt fit by a power-law. The shaded area indicates the 95% confidence level.

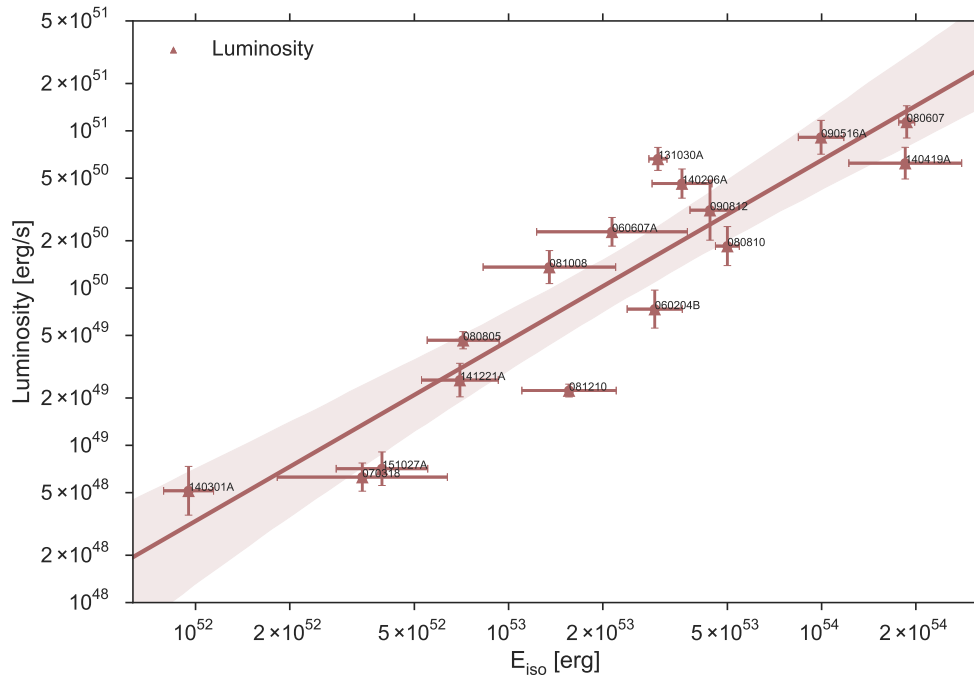


Figure 27. Relation between E_{iso} and L_p fit by a power-law. The shaded area indicates the 95% confidence level.

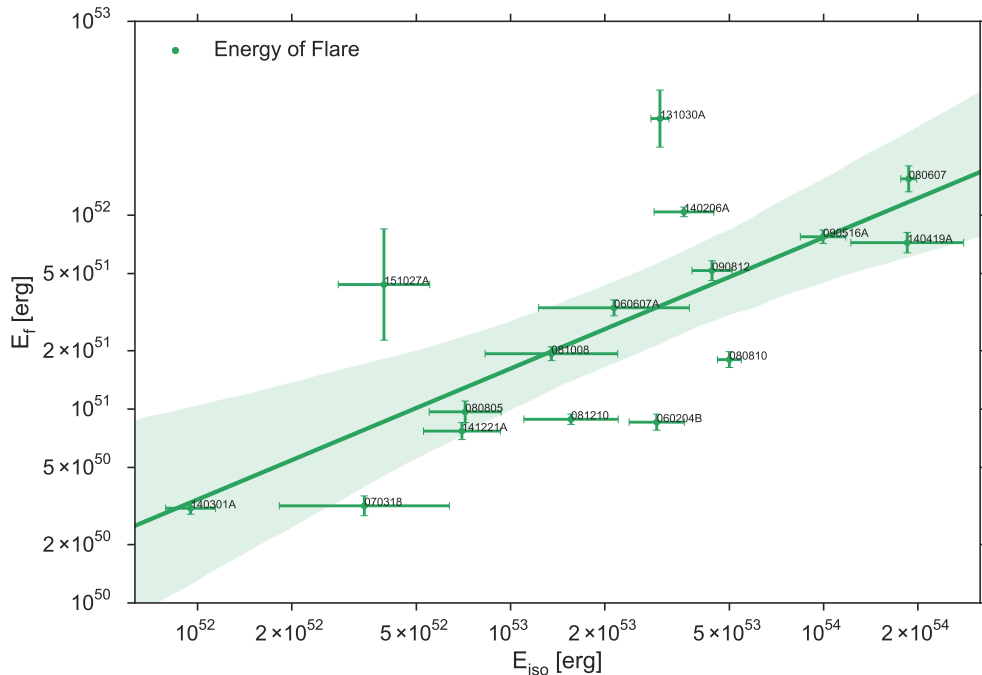


Figure 28. Relation between E_{iso} and E_f fit by a power-law. The shaded area indicates the 95% confidence level.

Correlation	Power-Law Index	Coefficient
$E_{iso} - t_p$	$-0.290(\pm 0.010)$	$-0.764(\pm 0.123)$
$E_{iso} - \Delta t$	$-0.461(\pm 0.042)$	$-0.760(\pm 0.138)$
$E_{iso} - L_p$	$1.186(\pm 0.037)$	$0.883(\pm 0.070)$
$E_{iso} - E_f$	$0.631(\pm 0.117)$	$0.699(\pm 0.145)$

Table 4. Power-law correlations among the quantities in Tab. 3. The values and uncertainties (at $1-\sigma$ confidence level) of the power-law index and of the correlation coefficient are obtained from 10^5 MCMC iterations. All relations are highly correlated.

As a consequence of the above, in view of the presence of the companion SN remnant ejecta (see [Becerra et al. 2016](#), for more details), we assume here that the spherical symmetry of the prompt emission is broken. Part of the energy due to the impact of the e^+e^- plasma on the SN is captured by the SN ejecta, and gives origin to the FPA emission as originally proposed by [Ruffini \(2015\)](#). We shall return to the study of the impact between the plasma and the SN ejecta in Sec. 10 after studying the motion of the matter composing the FPA in the next few sections.

It can also be seen that the relative partition between E_{prompt} and E_{FPA} strongly depends on the value of $E_{e^+e^-}$: the lower the GRB energy, the higher the FPA energy percentage and consequently the lower is the prompt energy percentage (see Fig. 31).

In [Becerra et al. \(2016\)](#) we indicate that both the value of $E_{e^+e^-}$ and the relative ratio of the above two components can in principle be explained in terms of the geometry of the binary nature of the system: the smaller the distance is between the CO_{core} and the companion NS, the shorter the binary period of the system, and the larger the value of $E_{e^+e^-}$.

8. ON THE FLARE THERMAL EMISSION, ITS TEMPERATURE AND DYNAMICS

We discuss now the profound difference between the prompt emission, which we recall is emitted at distances of the order of 10^{16} cm away from the newly-born BH with $\Gamma \approx 10^2-10^3$, and the FPA phase. We focus on a further

GRB	z	E_{iso} (erg)	E_{FPA} (erg)
060204B	2.3393	$2.93(\pm 0.60) \times 10^{53}$	$6.02(\pm 0.20) \times 10^{51}$
060607A	3.082	$2.14(\pm 1.19) \times 10^{53}$	$2.39(\pm 0.12) \times 10^{52}$
070318	0.84	$3.41(\pm 2.14) \times 10^{52}$	$4.76(\pm 0.21) \times 10^{51}$
080607	3.04	$1.87(\pm 0.11) \times 10^{54}$	$4.32(\pm 0.96) \times 10^{52}$
080805	1.51	$7.16(\pm 1.90) \times 10^{52}$	$6.65(\pm 0.42) \times 10^{51}$
080810	3.35	$5.00(\pm 0.44) \times 10^{53}$	$1.67(\pm 0.14) \times 10^{52}$
081008	1.967	$1.35(\pm 0.66) \times 10^{53}$	$6.56(\pm 0.60) \times 10^{51}$
081210	2.0631	$1.56(\pm 0.54) \times 10^{53}$	$6.59(\pm 0.60) \times 10^{51}$
090516A	4.109	$9.96(\pm 1.67) \times 10^{53}$	$3.34(\pm 0.22) \times 10^{52}$
090812	2.452	$4.40(\pm 0.65) \times 10^{53}$	$3.19(\pm 0.36) \times 10^{52}$
131030A	1.293	$3.00(\pm 0.20) \times 10^{53}$	$4.12(\pm 0.23) \times 10^{52}$
140206A	2.73	$3.58(\pm 0.79) \times 10^{53}$	$5.98(\pm 0.69) \times 10^{52}$
140301A	1.416	$9.50(\pm 1.75) \times 10^{51}$	$1.42(\pm 0.14) \times 10^{50}$
140419A	3.956	$1.85(\pm 0.77) \times 10^{54}$	$6.84(\pm 0.82) \times 10^{52}$
141221A	1.47	$6.99(\pm 1.98) \times 10^{52}$	$5.31(\pm 1.21) \times 10^{51}$
151027A	0.81	$3.94(\pm 1.33) \times 10^{52}$	$1.19(\pm 0.18) \times 10^{52}$

Table 5. GRB sample properties of the prompt and FPA phases. This table lists: z , E_{iso} , and the FPA energy E_{FPA} from the flare till 10^9 s.

Correlation	Power-Law Index	Coefficient
$E_{iso}-E_{FPA}$	$0.613(\pm 0.041)$	$0.791(\pm 0.103)$
$E_{iso}-E_{FPA}/E_{iso}$	$-0.005(\pm 0.002)$	$0.572(\pm 0.178)$

Table 6. Power-law correlations among the quantities in Tab. 5. The statistical considerations of Tab. 4 are valid here as well.

fundamental set of data, which originates from a thermal emission associated with the flares⁵. Only in some cases is this emission so clear and prominent that it allows the estimation of the flare expansion speed, and the determination of its mildly relativistic Lorentz factor $\Gamma \lesssim 4$, which creates a drastic separatrix, both in the energy and in the gamma factor between the astrophysical nature of the prompt emission and of the flares.

Following the standard data reduction procedure of Swift-XRT (Romano et al. 2006; Evans et al. 2007, 2009), X-ray data within the duration of flare are retrieved from the United Kingdom Swift Science Data Centre (UKSSDC)⁶ and analyzed by Heasoft⁷. Tab. 7 shows the fit of the spectrum within the duration Δt of the flare for each BdHN of the sample. As a first approximation, in computing the radius we have assumed a constant expansion velocity of $0.8c$ indicated for some BdHNe, such as GRB 090618 (Ruffini et al. 2014) and GRB 130427A (Ruffini et al. 2015b). Out of 16 sources, 7 BdHNe have highly confident thermal components (significance > 0.95 , see boldface in Tab. 7), which means that the addition of a blackbody spectrum improves a single power-law fit (which is, conversely, excluded at $2-\sigma$ of confidence level). These blackbodies have fluxes in a range from 1% to 30% of the total flux and share similar order of magnitude radii, i.e., $\sim 10^{11}-10^{12}$ cm. In order to have a highly significant thermal component, the blackbody radiation itself should be prominent, as well as its ratio to the non-thermal part. Another critical reason is that the observable temperature must be compatible with the satellite bandpass. For example, Swift-XRT observes in the 0.3–10 keV photon energy band, but the hydrogen absorption affects the lower energy part (~ 0.5 keV), and data

⁵ The late afterglow phases have been already discussed in Pisani et al. (2013, 2016).

⁶ <http://www.swift.ac.uk>

⁷ <http://heasarc.gsfc.nasa.gov/lheasoft/>

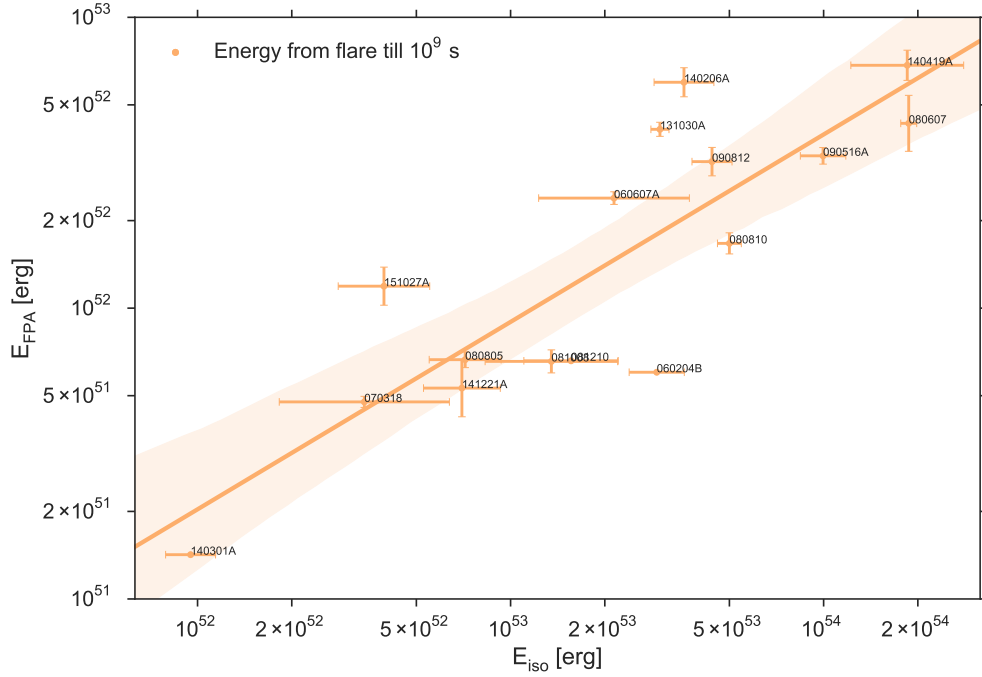


Figure 29. Relation between E_{iso} and E_{FPA} fit by a power-law. The shaded area indicates the 95% confidence level.

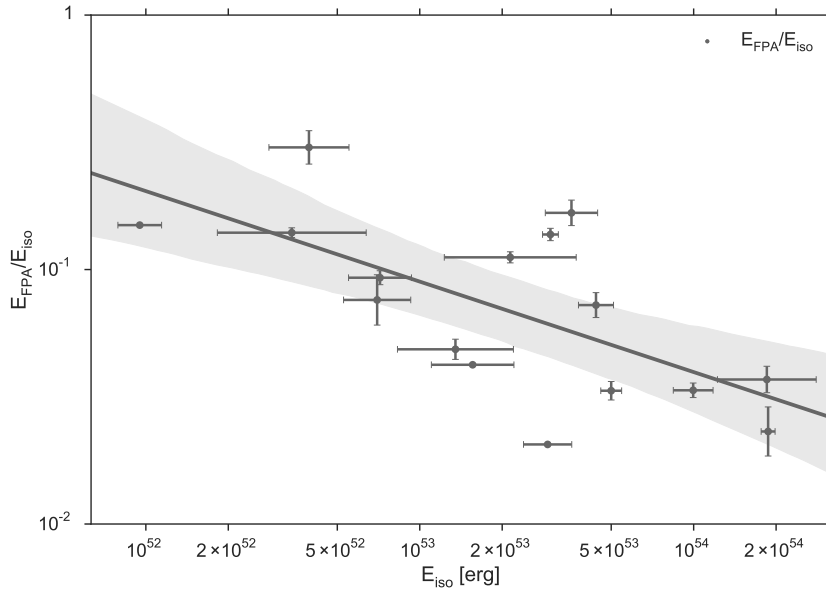


Figure 30. Relation between the percentage of $E_{e^+e^-}$ going to the SN ejecta and accounting for the energy in FPA, i.e., $E_{FPA}/E_{iso} \times 100\%$, and E_{iso} fit by a power-law. The shaded area indicates the 95% confidence level.

is always not adequate beyond 5 keV, due to the low effective area of satellite for high energy photons. The reliable temperature only ranges from 0.15 keV to 1.5 keV (since peak photon energy is equal to the temperature times 2.82), so the remaining 9 GRBs may contain a thermal component in the flare but outside the satellite bandpass.

We now attempt to perform a more refined analysis to infer the value of β from the observations. We assume that during the flare the black body emitter has spherical symmetry and expands with a constant Lorentz gamma factor.

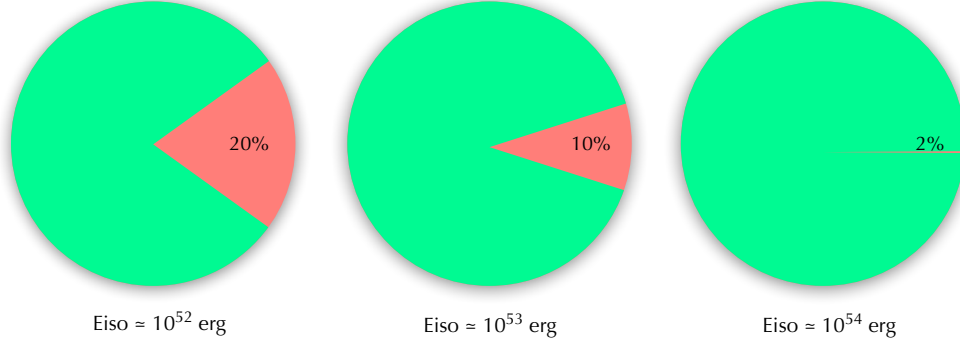


Figure 31. Distribution of the GRB total energy $E_{e+e-} = E_{iso}$ into prompt and FPA energies. The percentage of E_{e+e-} going to the SN ejecta accounting for the energy in FPA phase appears in red, i.e., $E_{FPA}/E_{iso} \times 100\%$. The green part is therefore the percentage of E_{e+e-} used in the prompt emission, i.e., $E_{prompt}/E_{iso} \times 100\%$. It can be seen that the lower the GRB energy $E_{e+e-} = E_{iso}$, the higher the FPA energy percentage, and consequently the lower the prompt energy percentage.

GRB	Radius (cm)	kT_{obs} (keV)	Significance
060204B	$1.80(\pm 1.11) \times 10^{11}$	0.60(±0.15)	0.986
060607A	$1.67(\pm 1.01) \times 10^{11}$	0.92(±0.24)	0.991
070318	<i>unconstrained</i>	1.79(±1.14)	0.651
080607	$1.52(\pm 0.72) \times 10^{12}$	0.49(±0.10)	0.998
080805	$1.12(\pm 1.34) \times 10^{11}$	1.31(±0.59)	0.809
080810	$2.34(\pm 4.84) \times 10^{11}$	0.61(±0.57)	0.999
081008	$1.84(\pm 0.68) \times 10^{12}$	0.32(±0.03)	0.999
081210	<i>unconstrained</i>	0.80(±0.51)	0.295
090516A	<i>unconstrained</i>	1.30(±1.30)	0.663
090812	$1.66(\pm 1.84) \times 10^{12}$	0.24(±0.12)	0.503
131030A	$3.67(\pm 1.02) \times 10^{12}$	0.55(±0.06)	0.999
140206A	$9.02(\pm 2.84) \times 10^{11}$	0.54(±0.07)	0.999
140301A	<i>unconstrained</i>	<i>unconstrained</i>	0.00
140419A	$1.85(\pm 1.17) \times 10^{12}$	0.23(±0.05)	0.88
141221A	$1.34(\pm 2.82) \times 10^{12}$	0.24(±0.24)	0.141
151027A	$1.18(\pm 0.67) \times 10^{12}$	0.29(±0.06)	0.941

Table 7. Radii and temperatures of the thermal components detected within the flare duration Δt . The observed temperatures kT_{obs} are inferred from fitting with a power-law plus blackbody spectral model. The significance of a blackbody is computed by the maximum likelihood ratio for comparing nested models and its addition improves a fit when the significance is > 0.95 . The radii are calculated assuming mildly-relativistic motion ($\beta = 0.8$) and isotropic radiation. The GRBs listed in boldface have prominent black bodies, with radii of the order of $\sim 10^{11}$ – 10^{12} cm. Uncertainties are given at $1-\sigma$ confidence level.

Therefore, the expansion velocity β is also constant during the flare. The relations between the comoving time t_{com} , the laboratory time t , the arrival time t_a , and the arrival time t_a^d at the detector, given in Eq. (2), in this case become:

$$t_a^d = t_a(1+z) = t(1 - \beta \cos \vartheta)(1+z) = \Gamma t_{\text{com}}(1 - \beta \cos \vartheta)(1+z). \quad (7)$$

We can infer an effective radius R of the black body emitter from: 1) the observed black body temperature T_{obs} , which comes from the spectral fit of the data during the flare; 2) the observed bolometric black body flux $F_{\text{bb,obs}}$, computed

from T_{obs} and the normalization of the black body spectral fit; and 3) the cosmological redshift z of the source (see also [Izzo et al. 2012](#)). We recall that $F_{\text{bb,obs}}$ by definition is given by:

$$F_{\text{bb,obs}} = \frac{L}{4\pi D_L(z)^2}, \quad (8)$$

where $D_L(z)$ is the luminosity distance of the source, which in turn is a function of the cosmological redshift z , and L is the source bolometric luminosity (i.e., the total emitted energy per unit time). L is Lorentz invariant, so we can compute it in the co-moving frame of the emitter using the usual black body expression:

$$L = 4\pi R_{\text{com}}^2 \sigma T_{\text{com}}^4, \quad (9)$$

where R_{com} and T_{com} are the comoving radius and the comoving temperature of the emitter, respectively, and σ is the Stefan-Boltzmann constant. We recall that T_{com} is constant over the entire shell due to our assumption of spherical symmetry. From Eq. (8) and Eq. (9) we then have:

$$F_{\text{bb,obs}} = \frac{R_{\text{com}}^2 \sigma T_{\text{com}}^4}{D_L(z)^2}. \quad (10)$$

We now need the relation between T_{com} and the observed black body temperature T_{obs} . Considering both the cosmological redshift and the Doppler effect due to the velocity of the emitting surface, we have:

$$T_{\text{obs}}(T_{\text{com}}, z, \Gamma, \cos \vartheta) = \frac{T_{\text{com}}}{(1+z)\Gamma(1-\beta \cos \vartheta)} = \frac{T_{\text{com}} \mathcal{D}(\cos \vartheta)}{1+z}, \quad (11)$$

where we have defined the Doppler factor $\mathcal{D}(\cos \vartheta)$ as:

$$\mathcal{D}(\cos \vartheta) \equiv \frac{1}{\Gamma(1-\beta \cos \vartheta)}. \quad (12)$$

Eq. (11) gives us the observed black body temperature of the radiation coming from different points of the emitter surface, corresponding to different values of $\cos \vartheta$. However, since the emitter is at a cosmological distance, we are not able to resolve spatially the source with our detectors. Therefore, the temperature that we actually observe corresponds to an average of Eq. (11) computed over the emitter surface:⁸

$$\begin{aligned} T_{\text{obs}}(T_{\text{com}}, z, \Gamma) &= \frac{1}{1+z} \frac{\int_{\beta}^1 \mathcal{D}(\cos \vartheta) T_{\text{com}} \cos \vartheta d \cos \vartheta}{\int_{\beta}^1 \cos \vartheta d \cos \vartheta} \\ &= \frac{2}{1+z} \frac{\beta(\beta-1) + \ln(1+\beta)}{\Gamma \beta^2 (1-\beta^2)} T_{\text{com}} \\ &= \Theta(\beta) \frac{\Gamma}{1+z} T_{\text{com}} \end{aligned} \quad (13)$$

where we defined

$$\Theta(\beta) \equiv 2 \frac{\beta(\beta-1) + \ln(1+\beta)}{\beta^2}, \quad (14)$$

we have used the fact that due to relativistic beaming, we observe only a portion of the surface of the emitter defined by:

$$\beta \leq \cos \vartheta \leq 1, \quad (15)$$

and we used the definition of Γ given in Sec. 3. Therefore, inverting Eq. (13), the comoving black body temperature T_{com} can be computed from the observed black body temperature T_{obs} , the source cosmological redshift z and the emitter Lorentz gamma factor in the following way:

$$T_{\text{com}}(T_{\text{obs}}, z, \Gamma) = \frac{1+z}{\Theta(\beta)\Gamma} T_{\text{obs}}. \quad (16)$$

⁸ From the point of view of the observer the spectrum is not a perfect black body, coming from a convolution of black body spectra at different temperatures. The black body component we obtain from the spectral fit of the observed data is an effective black body of temperature T_{obs} , analogously to other cases of effective temperatures in cosmology (see, e.g., [Ruffini et al. 1983](#)).

We can now insert Eq. (16) into Eq. (10) to obtain:

$$F_{\text{bb,obs}} = \frac{R_{\text{com}}^2}{D_L(z)^2} \sigma T_{\text{com}}^4 = \frac{R_{\text{com}}^2}{D_L(z)^2} \sigma \left[\frac{1+z}{\Theta(\beta)\Gamma} T_{\text{obs}} \right]^4. \quad (17)$$

Since the radius R_{lab} of the emitter in the laboratory frame is related to R_{com} by:

$$R_{\text{com}} = \Gamma R_{\text{lab}}, \quad (18)$$

we can insert Eq. (18) into Eq. (17) and obtain:

$$F_{\text{bb,obs}} = \frac{(1+z)^4}{\Gamma^2} \left(\frac{R_{\text{lab}}}{D_L(z)} \right)^2 \sigma \left[\frac{T_{\text{obs}}}{\Theta(\beta)} \right]^4. \quad (19)$$

Solving Eq. (19) for R_{lab} we finally obtain the thermal emitter effective radius in the laboratory frame:

$$R_{\text{lab}} = \Theta(\beta)^2 \Gamma \frac{D_L(z)}{(1+z)^2} \sqrt{\frac{F_{\text{bb,obs}}}{\sigma T_{\text{obs}}^4}} = \Theta(\beta)^2 \Gamma \phi_0, \quad (20)$$

where we have defined ϕ_0 :

$$\phi_0 \equiv \frac{D_L(z)}{(1+z)^2} \sqrt{\frac{F_{\text{bb,obs}}}{\sigma T_{\text{obs}}^4}}. \quad (21)$$

In astronomy the quantity ϕ_0 is usually identified with the radius of the emitter. However, in relativistic astrophysics this identity cannot be straightforwardly applied, because the estimate of the effective emitter radius R_{lab} in Eq. 20 crucially depends on the knowledge of its expansion velocity β (and, correspondingly, of Γ).

It must be noted that Eq. (20) above gives the correct value of R_{lab} for all values of $0 \leq \beta \leq 1$ by taking all the relativistic transformations properly into account. In the non-relativistic limit ($\beta \rightarrow 0$, $\Gamma \rightarrow 1$) we have respectively:

$$\Theta \xrightarrow{\beta \rightarrow 0} 1, \quad \Theta^2 \xrightarrow{\beta \rightarrow 0} 1, \quad (22)$$

$$T_{\text{com}} \xrightarrow{\beta \rightarrow 0} T_{\text{obs}}(1+z), \quad R_{\text{lab}} \xrightarrow{\beta \rightarrow 0} \phi_0, \quad (23)$$

as expected.

9. IMPLICATIONS ON THE DYNAMICS OF THE FLARES FROM THEIR THERMAL EMISSION

An estimate of the expansion velocity β can be deduced from the ratio between the variation of the emitter effective radius ΔR_{lab} and the emission duration in laboratory frame Δt , i.e.,

$$\beta = \frac{\Delta R_{\text{lab}}}{c \Delta t} = \Theta(\beta)^2 \Gamma (1 - \beta \cos \vartheta) (1+z) \frac{\Delta \phi_0}{c \Delta t_a^d}, \quad (24)$$

where we have used Eq. (20) and the relation between Δt and Δt_a^d given in Eq. (7). We then have:

$$\beta = \Theta(\beta)^2 \frac{1 - \beta \cos \vartheta}{\sqrt{1 - \beta^2}} (1+z) \frac{\Delta \phi_0}{c \Delta t_a^d}, \quad (25)$$

where we used the definition of Γ given in Sec. 3.

For example, in GRB 081008 we observe a temperature of $T_{\text{obs}} = (0.44 \pm 0.12)$ keV between $t_a^d = 280$ s and $t_a^d = 300$ s (i.e., 20 s before the flare peak time), and a temperature of $T_{\text{obs}} = (0.31 \pm 0.05)$ keV between $t_a^d = 300$ s and $t_a^d = 320$ s (i.e., 20 s after the flare peak time, see the corresponding spectra in Fig. 32). In these two time intervals we can infer ϕ_0 and by solving Eq. (25) and taking the errors of the parameters properly into account, get the value of $\langle \beta \rangle$ corresponding to the average expansion speed of the emitter from the beginning of its expansion up to the upper bound of the time interval considered. The results so obtained are listed in Tab. 8. Moreover, we can also compute the value of $\langle \beta \rangle$ between the two time intervals considered above. For $\cos \vartheta = 1$, namely along the line of sight, we obtain $\langle \beta \rangle = 0.90_{-0.31}^{+0.06}$ and $\langle \Gamma \rangle = 2.34_{-1.10}^{+1.29}$. In conclusion, no matter what the details of the approximation adopted, the Lorentz gamma factor is always moderate, i.e., $\Gamma \lesssim 4$.

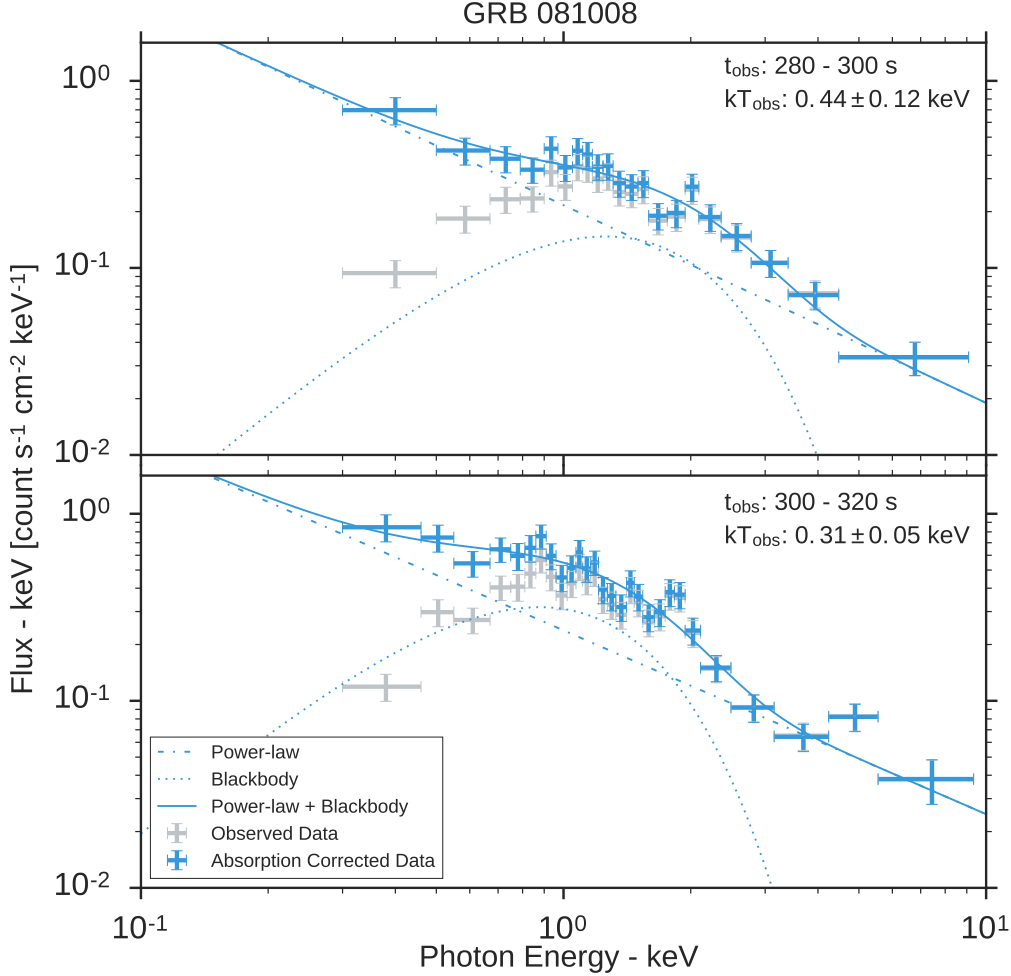


Figure 32. Thermal evolution of GRB 081008 ($z = 1.967$) in the observer frame. The X-ray flare of this GRB peaks at $304(\pm 17)$ s. **Upper:** Swift-*XRT* spectrum from 280 s to 300 s. **Lower:** Swift-*XRT* spectrum from 300 s to 320 s. The grey points are the observed data markedly absorbed at low energies, while the blue points are absorption corrected ones. The data is fit with a combination of power-law (dot-dashed lines) and blackbody (dotted line curves) spectra. The power-law + blackbody spectra are shown as solid curves. Clearly, the temperature decreases with time from ~ 0.44 keV to ~ 0.31 keV, but the ratio of thermal component goes up from $\sim 20\%$ to $\sim 30\%$. This is a remarkable high percentage among our sample.

10. THE ELECTRON-POSITRON PLASMA AS THE COMMON ORIGIN OF THE PROMPT EMISSION AND THE X-RAY FLARES

10.1. Necessity for a new hydrodynamic code for $10 \leq B \leq 10^2$

As stated above, there are many different components in BdHNe: following episode 1 of the hypercritical accretion of the SN ejecta onto the NS, the prompt emission occurs with $\Gamma \approx 10^2\text{--}10^3$ which represents the most energetic component accelerated by the e^+e^- plasma; a third component which encompasses the X-ray flare with $\Gamma \lesssim 4$, which represents only a fraction of $E_{e^+e^-}$ ranging from 2 to 20% (see Fig. 31); finally, there are in addition the gamma-ray flare and the late X-ray flares which will be addressed in a forthcoming publication as well as the late afterglow phases, which have been already addressed in Pisani et al. (2013, 2016) but whose dynamics will be discussed elsewhere. As already mentioned, for definiteness we address here the case of X-ray flares.

In 3.5 we have shown that our model successfully explains the entire prompt emission as originating from the transparency of an initially optically thick e^+e^- plasma with a baryon load $B < 10^{-2}$ reaching $\Gamma \approx 10^2\text{--}10^3$ and the

Time interval	$280 \text{ s} \leq t_a^d \leq 300 \text{ s}$	$300 \text{ s} \leq t_a^d \leq 320 \text{ s}$
T_{obs} [keV]	0.44 ± 0.12	0.31 ± 0.05
ϕ_0 [cm]	$(5.6 \pm 3.2) \times 10^{11}$	$(1.44 \pm 0.48) \times 10^{12}$
$\langle \beta \rangle_{(\cos \vartheta=1)}$	$0.19^{+0.10}_{-0.11}$	$0.42^{+0.10}_{-0.12}$
$\langle \Gamma \rangle$	$1.02^{+0.03}_{-0.02}$	$1.10^{+0.07}_{-0.05}$
R_{lab} [cm]	$(7.1 \pm 4.1) \times 10^{11}$	$(2.34 \pm 0.78) \times 10^{12}$

Table 8. List of the physical quantities inferred from the thermal components observed during the flare of GRB 081008. For each time interval we summarize: the observed temperature T_{obs} , ϕ_0 , the average expansion speed $\langle \beta \rangle$ computed from the beginning up to the upper bound of the considered time interval, and the corresponding average Lorentz factor $\langle \Gamma \rangle$ and laboratory radius R_{lab} .

accelerated baryons interacting with the clouds of the CBM. The fundamental equations describing the dynamics of the optically thick plasma, its self-acceleration to ultra-relativistic velocities, and its interaction with the baryon load have been described in [Ruffini et al. \(1999, 2000\)](#). A semi-analytic approximate numerical code was developed, which assumed that the plasma expanded as a shell with a constant thickness in the laboratory frame (the so called ‘‘slab’’ approximation, see [Ruffini et al. 1999](#)). This semi-analytic approximate code was validated by comparing its results with the ones obtained by numerically integrating the complete system of equations, for selected values of the initial conditions. It turns out that the semi-analytic code is an excellent approximation to the complete system of equations for $B < 10^{-2}$, which is the relevant regime for the prompt emission, but this approximation is not valid beyond this limit (see [Ruffini et al. 1999, 2000](#), for details).

We examine here the possibility that also the energy of the X-ray flare component originates from a fraction of the e^+e^- plasma energy (see [Fig. 31](#)) interacting with the much denser medium of the SN ejecta with $10 \lesssim B \lesssim 10^2$. The above-mentioned semi-analytic approximate code cannot be used for this purpose, since it is valid only for $B < 10^{-2}$, and therefore, thanks to the more powerful computers we have at present, we move on here to a new numerical code to integrate the complete system of equations.

We investigate if indeed the dynamics to be expected from an initially pure e^+e^- plasma with a negligible baryon load relativistically expanding in the fireshell model, with an initial Lorentz factor $\Gamma \sim 100$, and then impacting onto such a SN ejecta can lead, reaching transparency, to the Lorentz factor $\Gamma \lesssim 4$ inferred from the thermal emission observed in the flares (see [Tabs. 7 and 8](#), and [Fig. 32](#)).

We have performed hydrodynamical simulations of such a process using the one-dimensional relativistic hydrodynamical (RHD) module included in the freely available PLUTO⁹ code ([Mignone et al. 2011](#)). In the spherically symmetric case considered here, only the radial coordinate is used and the code integrates partial differential equations with two variables: radius and time. This permits the study of the evolution of the plasma along one selected radial direction at a time. The code integrates the equations of an ideal relativistic fluid in the absence of gravity, which can be written as follows:

$$\frac{\partial(\rho\Gamma)}{\partial t} + \nabla \cdot (\rho\Gamma\mathbf{v}) = 0, \quad (26)$$

$$\frac{\partial m_r}{\partial t} + \nabla \cdot (m_r\mathbf{v}) + \frac{\partial p}{\partial r} = 0, \quad (27)$$

$$\frac{\partial \mathcal{E}}{\partial t} + \nabla \cdot (\mathbf{m} - \rho\Gamma\mathbf{v}) = 0, \quad (28)$$

where ρ and p are, respectively, the comoving fluid density and pressure, \mathbf{v} is the coordinate velocity in natural units ($c = 1$), $\Gamma = (1 - \mathbf{v}^2)^{-\frac{1}{2}}$ is the Lorentz gamma factor, $\mathbf{m} = h\Gamma^2\mathbf{v}$ is the fluid momentum, m_r its radial component, \mathcal{E} is the internal energy density, and h is the comoving enthalpy density which is defined by $h = \rho + \epsilon + p$. In this last

⁹ <http://plutocode.ph.unito.it/>

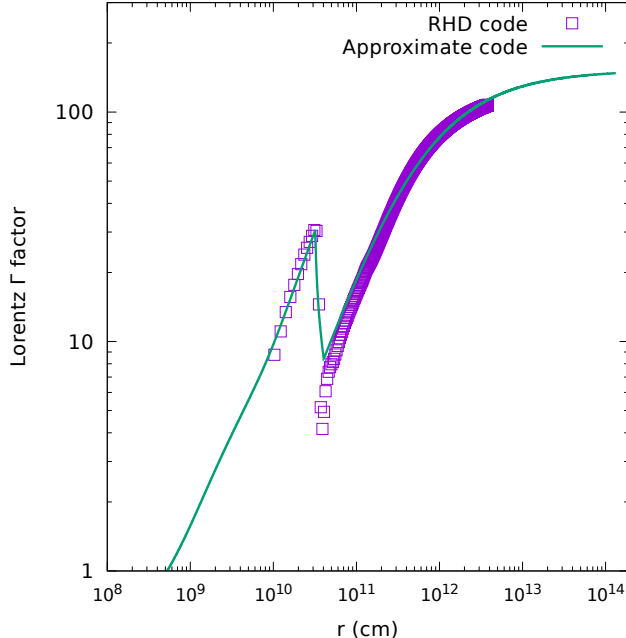


Figure 33. Lorentz gamma factor computed with the new RHD code compared with the one computed with the old semi-analytic approximate code. This plot is for $E_{e^+e^-} = 1.0 \times 10^{53}$ erg and $B = 6.61 \times 10^{-3}$. Similar agreement is found for other values of $E_{e^+e^-}$ and B as long as $B < 10^{-2}$.

definition ϵ is equal to \mathcal{E} measured in the comoving frame. We define \mathcal{E} as follows:

$$\mathcal{E} = h\Gamma^2 - p - \rho\Gamma. \quad (29)$$

The first two terms on the right hand side of this equation coincide with the T^{00} component of the fluid energy-momentum tensor $T^{\mu\nu}$, and the last one is the mass density in the laboratory frame.

Under the conditions discussed in Appendix B, the plasma satisfies the equation of state of an ideal relativistic gas, which can be expressed in terms of its enthalpy as:

$$h = \rho + \frac{\gamma p}{\gamma - 1}, \quad (30)$$

with $\gamma = 4/3$. Fixing this equation of state completely defines the system, leaving the choice of the boundary conditions as the only remaining freedom. To compute the evolution of these quantities in the chosen setup, the code uses the Harten-Lax-van Leer-Contact Riemann solver. Time integration is performed by means of a second-order Runge-Kutta algorithm, and a second-order total variation diminishing scheme is used for spatial reconstruction (Mignone et al. 2011). Before each integration step, the grid is updated according to an adaptive mesh refinement algorithm, provided by the CHOMBO library (Colella et al. 2003).

It must be emphasized that the above equations are equivalent (although written in a different form) to the complete system of equations used in Ruffini et al. (1999, 2000). To validate this new numerical code, we compare its results with the ones obtained with the old semi-analytic “slab” approximate code in the domain of its validity (i.e., for $B < 10^{-2}$), finding excellent agreement. As an example, in Fig. 33 we show the comparison between the Lorentz gamma factors computed with the two codes for one particular value of $E_{e^+e^-}$ and B . We can then conclude that for $B < 10^{-2}$ the new RHD code is consistent with the old semi-analytic “slab” approximate one, which in turn is consistent with the treatment done in Ruffini et al. (1999, 2000). This is not surprising, since we already stated that the above system of equations is equivalent to the one considered in Ruffini et al. (1999, 2000).

Having validated the new RHD code in the region of the parameter space where the old semi-analytic one can also be used, we now explore the region of $B > 10^{-2}$ which is relevant for the interaction of the plasma with the SN ejecta.

10.2. Inference from the IGC scenario for the ejecta mass profile

We start with the shape of the SN ejecta, following the results of the numerical simulations in [Becerra et al. \(2016\)](#).

The first simulations of the IGC process were presented in [Fryer et al. \(2014\)](#) including: 1) detailed SN explosions of the CO_{core} obtained from a 1D core-collapse SN code of Los Alamos ([Fryer et al. 1999](#)); 2) the hydrodynamic details of the hypercritical accretion process; 3) the evolution of the SN ejecta material entering the Bondi-Hoyle region all the way up to its incorporation into the NS in a spherically symmetric approximation. Then in [Becerra et al. \(2015\)](#) estimates were presented of the angular momentum carried by the SN ejecta and transferred to the NS via accretion. The effects of such angular momentum transfer into the evolution and fate of the system were examined there. These calculations followed the following procedure: first the accretion rate onto the NS is computed adopting an homologous expansion of the SN ejecta and introducing the pre-SN density profile of the CO_{core} envelope from numerical simulations. Then the angular momentum that the SN material might transfer to the NS is estimated: it turns out that the ejecta have enough angular momentum to circularize for a short time and form a disc-like structure around the NS. Then the evolution of the NS central density and rotation angular velocity is followed computing the equilibrium configurations from the numerical solution of the axisymmetric Einstein equations in full rotation, until the critical point of collapse of the NS to a BH is reached, accounting for the stability limits given by mass-shedding and the secular axisymmetric instability. In [Becerra et al. \(2016\)](#) an improved simulation of all the above processes leading to a BdHN was recently presented. In particular:

1. The accretion rate estimate includes effects of the finite size/thickness of the ejecta density profile.
2. Different CO_{core} progenitors leading to different SN ejecta masses were also considered.
3. The maximum orbital period, P_{\max} , up to which the accretion onto the NS companion is high enough to bring it to the critical mass for gravitational collapse to a BH, first estimated in [Becerra et al. \(2015\)](#), was computed for all the possible initial values of the mass of the NS companion. Various values of the angular momentum transfer efficiency parameter were also explored there.
4. It was shown there how the presence of the NS companion gives rise to large asymmetries in the SN ejecta. As we show here such a density of the SN ejecta modified by the presence of the NS companion plays a crucial role in the physical explanation for the occurrence of X-ray flares.
5. The evolution of the SN material and its consequent accretion onto the NS companion is followed via a smoothed-particle-hydrodynamic-like code in which point-like particles describe the SN ejecta. The trajectory of each particle is computed by solving the Newtonian equations of motion including the effects of the gravitational field of the NS on the SN ejecta including the orbital motion as well as the changes in the NS gravitational mass owing to the accretion process via the Bondi-Hoyle formalism. The initial conditions of the SN are obtained from the Los Alamos core-collapse SN code ([Fryer et al. 1999](#)). The initial power-law density profile of the CO envelope is simulated by populating the inner layers with more particles. The particles crossing the Bondi-Hoyle radius are captured and accreted by the NS so we remove them from the system. We adopted a total number of 16 million particles in this simulation.

For further details we refer the reader to [Becerra et al. \(2016\)](#) and references therein.

10.3. *The density profile of the ejecta and the reaching of transparency*

We now use the results of a simulation with the following binary parameters: the NS has an initial mass of $2.0 M_{\odot}$; the CO_{core} obtained from a progenitor with a zero-age-main-sequence mass $M_{\text{ZAMS}} = 30 M_{\odot}$ leads to a total ejecta mass $7.94 M_{\odot}$, and follows an approximate power-law profile $\rho_{\text{ej}}^0 \approx 3.1 \times 10^8 (8.3 \times 10^7 / r)^{2.8} \text{ g cm}^{-3}$. The orbital period is $P \approx 5 \text{ min}$, i.e., a binary separation $a \approx 1.5 \times 10^{10} \text{ cm}$. For these parameters the NS reaches the critical mass and collapses to form a BH.

[Fig. 34](#) shows the SN ejecta mass that is enclosed within a cone of 5 degrees of semi-aperture angle, whose vertex is at the position of the BH at the moment of its formation (see the lower left panel of [Fig. 6](#) in [Becerra et al. 2016](#)), and whose axis is along various directions measured counterclockwise with respect to the line of sight. [Fig. 35](#) shows instead the cumulative radial mass profiles within a selected number of the aforementioned cones. We can see from these plots how the e^+e^- plasma engulfs different amounts of baryonic mass along different directions due to the asymmetry of the SN ejecta created by the presence of the NS binary companion and the accretion process onto it (see [Becerra et al. 2016](#)).

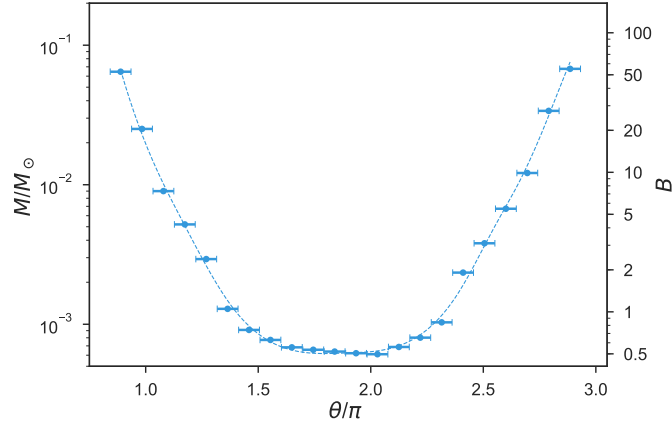


Figure 34. The SN ejecta mass enclosed within a cone of 5 degrees of semi-aperture angle, whose vertex is at the position of the BH at the moment of its formation (see the lower left panel of Fig. 6 in Becerra et al. 2016), and whose axis is along various directions measured counterclockwise with respect to the line of sight. The binary parameters of these simulations are: the NS has an initial mass of $2.0 M_{\odot}$; the CO_{core} obtained from a progenitor with a zero-age-main-sequence mass $M_{\text{ZAMS}} = 30 M_{\odot}$ leads to a total ejecta mass $7.94 M_{\odot}$, and the orbital period is $P \approx 5$ min, i.e., a binary separation $a \approx 1.5 \times 10^{10}$ cm. The vertical axis on the right side gives, as an example, the corresponding value of the baryon loading B assuming a plasma energy of $E_{e^+e^-} = 3.16 \times 10^{53}$ erg.

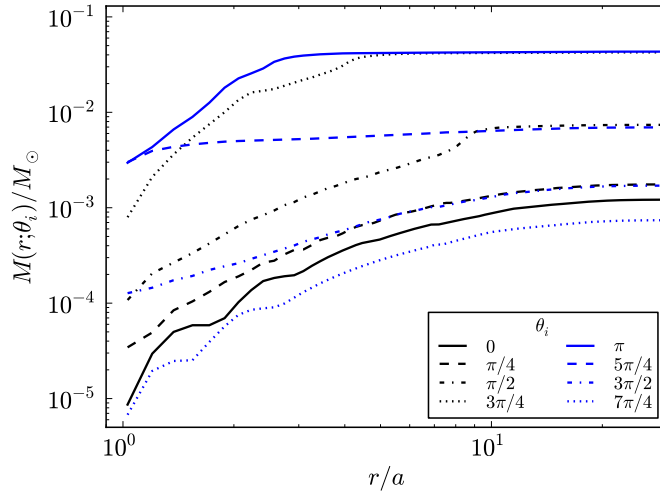


Figure 35. Cumulative radial mass profiles within selected cones among the ones used in Fig. 34. We note that the final value for the cumulative mass reached at the end of each direction, namely the value when each curve flattens, is consistent with the total integrated mass value of the corresponding direction shown in Fig. 34. The binary parameters of these simulations are: the NS has an initial mass of $2.0 M_{\odot}$; the CO_{core} obtained from a progenitor with a zero-age-main-sequence mass $M_{\text{ZAMS}} = 30 M_{\odot}$ leads to a total ejecta mass $7.94 M_{\odot}$, and the orbital period is $P \approx 5$ min, i.e., a binary separation $a \approx 1.5 \times 10^{10}$ cm.

In these calculations, we have chosen initial conditions consistent with those of the BdHNe. At the initial time, the e^+e^- plasma has $E_{e^+e^-} = 3.16 \times 10^{53}$ erg, a negligible baryon load and is distributed homogeneously within a region of radii on the order of 10^8 – 10^9 cm. The surrounding SN ejecta, whose pressure has been assumed to be negligible, has a mass density radial profile given by:

$$\rho \propto (R_0 - r)^\alpha, \quad (31)$$

where the parameters R_0 and α , with $2 < \alpha < 3$, as well as the normalization constant, are chosen to fit the profiles obtained in Becerra et al. (2016) and represented in Fig. 35. The initial radial velocity is taken to be $v_r \propto r$ in order to reproduce the homologous expansion of the SN ejecta before its interaction with the plasma. Every choice of these parameters corresponds to studying the evolution along a single given direction.

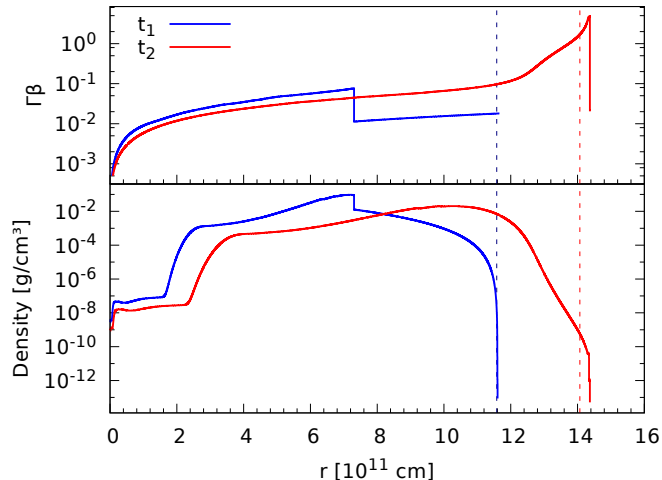


Figure 36. Above: Distribution of the velocity inside the SN ejecta at the two fixed values of the laboratory time t_1 (before the plasma reaches the external surface of the ejecta) and t_2 (the moment at which the plasma, after having crossed the entire SN ejecta, reaches the external surface). We plotted the quantity $\Gamma\beta$, recalling that we have $\Gamma\beta \sim \beta$ when $\beta < 1$ and $\Gamma\beta \sim \Gamma$ when $\beta \sim 1$. **Below:** Corresponding distribution of the mass density of the SN ejecta in the laboratory frame ρ_{lab} . These particular profiles are made using a baryon load $B = 200$. The dashed vertical lines corresponds to the two values of the transparency radius R_{ph} , see Fig. 37 and Eq.(32). In particular, we see that at t_1 the shock front did not reach R_{ph} yet and the system is optically thick.

The evolution from these initial conditions leads to the formation of a shock and to its subsequent expansion until reaching the outermost part of the SN. In Fig. 36 we show the radial distribution profiles of the velocity and mass density ρ_{lab} in the laboratory frame inside the SN ejecta as a function of r for $B = 200$ at two selected values of the laboratory time. The velocity distribution peaks at the shock front (with a Lorentz gamma factor $\Gamma \lesssim 4$), and behind the front it is formed a broad tail of accelerated material with $0.1 \lesssim \beta \lesssim 1$.

Fig. 37 shows the Lorentz Γ factor at the transparency radius R_{ph} , namely the radius at which the optical depth τ , calculated from the observer's line of sight, is equal to 1. If we assume to have a constant cross section, τ becomes Lorentz invariant, and therefore we can compute it in laboratory coordinates in the following way:

$$\tau = \int_{R_{ph}}^{\infty} dr \sigma_T n_{e^-}(r), \quad (32)$$

where $\sigma_T = 6.65 \times 10^{-25} \text{ cm}^2$ is the Thomson cross section, and the electron density is related to the baryon mass density by means of the formula $n_{e^-} = \rho \Gamma / m_P$, where m_P is the proton mass, the mass of the electrons and positrons is considered to be negligible with respect to that of the baryons, and we have assumed to have one electron per nucleon on average. The values of Γ at $r = R_{ph}$ computed in this way are shown in Fig. 37, as a function of the time measured in the laboratory frame, for several values of $B > 10^{-2}$ corresponding to the expansion of the e^+e^- plasma along several different directions inside the SN ejecta (see Figs. 34 and 35).

We conclude that the relativistic expansion of an initially pure e^+e^- plasma (see Fig. 33), interacting with a SN ejecta with the above-described induced asymmetries (see Figs. 39–40), leads to the formation of a shock that reaches the outermost part of the ejecta with Lorentz gamma factors at the transparency radius $\Gamma(R_{ph}) \lesssim 4$. This is in striking agreement with the one inferred from the thermal component observed in the flares (see Sec. 9). The space-time diagram of the global scenario is represented in Fig. 39. Clearly in this approach neither ultra-relativistic jetted emission nor synchrotron or inverse Compton processes play any role.

11. SUMMARY, CONCLUSIONS AND PERSPECTIVES

11.1. Summary

In the last twenty five years the number of observed GRBs has exponentially increased thanks to unprecedented technological developments in all ranges of wavelengths, going from the X-ray, to the gamma ray to the GeV radiation, as well as to the radio and the optical. In spite of this progress, the traditional GRB approach has continued to

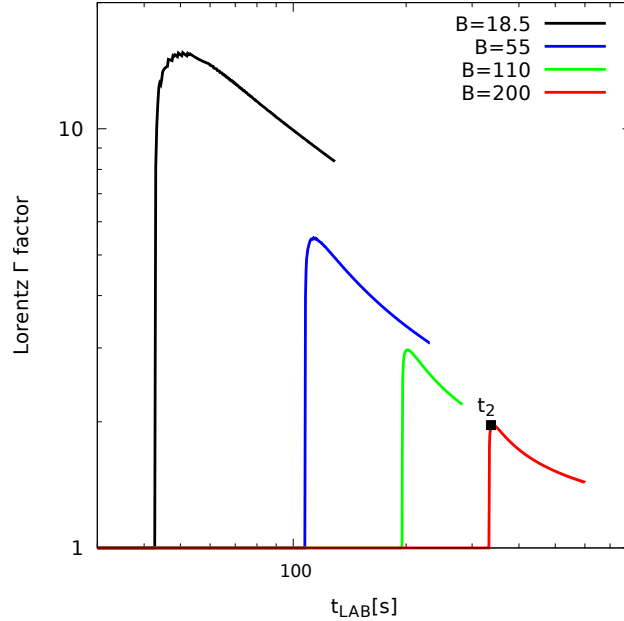


Figure 37. Lorentz Γ factor at the transparency radius R_{ph} as a function of the laboratory time for $E_{e^+e^-} = 3.16 \times 10^{53}$ erg and various selected values of the B parameter. Such B values correspond to the expansion of the e^+e^- plasma along various selected directions inside the remnant (see Figs. 34 and 35). Along the red curve, corresponding to $B = 200$, there is marked the laboratory time instant t_2 represented in Fig. 36 (at t_1 the plasma did not reach R_{ph} yet). We see that these results are in agreement with the Lorentz gamma factor $\Gamma \lesssim 4$ inferred from the thermal emission observed in the flare (see Sec. 9).

follow the paradigm of a single system (the “collapsar” paradigm, see Woosley 1993), where accretion into an already formed BH occurs (see, e.g., Piran 2004, and references therein). Following the fireball model, synchrotron and inverse Compton emission processes, related to an ultra-relativistic jetted emission described by the Blandford & McKee (1976) solution, have been assumed to occur (see, e.g., Troja et al. 2015, for one of the latest example where this approach is further extended to the GeV emission component). The quest for a “standard” GRB model has been pursued even lately (see, e.g., Chincarini et al. 2007; Margutti et al. 2010) neglecting differences among GRB subclasses and/or neglecting all relativistic corrections in the time parameterizations presented in Sec. 3. Under these conditions, it is not surprising that the correlations we have found here have been missed.

It is appropriate to recall that a “standard” GRB energy of 10^{51} erg (Frail et al. 2001) was considered, assuming the collimation of GRBs and the existence of a light-curve break in the GRB afterglows. This possibility followed from the traditional approach expecting the ultra-relativistic component to extend all the way from the prompt emission to the last phases of the afterglow (Mao & Yi 1994; Sari et al. 1999; Panaitescu & Mészáros 1999). This “traditional” approach to GRBs has appeared in a large number of papers over recent decades and is well summarized in a series of review papers (see, e.g., Piran 1999, 2004; Mészáros 2002, 2006; Berger 2014; Kumar & Zhang 2015), which are disproved by the data presented here in which the upper limit for the Lorentz factor $\Gamma \lesssim 4$ is established in the FPA phase.

Since 2001 we have followed an alternative approach introducing three paradigms: the space-time parametrization of GRBs (Ruffini et al. 2001a), the field equations of the prompt emission phase (Ruffini et al. 2002), and the IGC paradigm (Rueda & Ruffini 2012; Penacchioni et al. 2013; Ruffini et al. 2015b), see Sec. 3. Since then:

a) we demonstrated that all GRBs originate in binary systems: the short GRBs in binary NSs or in binaries composed of a NS and a BH (Fryer et al. 2015; Ruffini et al. 2016a); the long GRBs in binary systems composed of CO_{core} and a NS, or alternatively a BH and a CO_{core} , or also a white dwarf and a NS;

b) we distinguish GRBs into seven different subclasses (Ruffini et al. 2016a), each characterized by specific signatures in their spectra and luminosities in the various energy bands;

c) we address the new physical and astrophysical processes in the ultra-relativistic regimes made possible by the vast amount of gravitational and rotational energies in such binaries.

As recalled in Secs. 1–3, we have confirmed the binary nature of the GRB progenitors (see, e.g., Fryer et al. 2014; Becerra et al. 2015; Fryer et al. 2015; Becerra et al. 2016; Ruffini et al. 2016b; Aimuratov et al. 2017). We have obtained the first evidence of the formation of a BH in the hypercritical accretion process of the SN ejecta onto the binary NS companion: the BdHN (Ruffini et al. 2014, 2015b, 2016a), clearly different from the single star collapsar model. Finally, in this paper we have addressed the interaction which occurs in a BdHN of the GRB on the SN ejecta considered as the origin of the X-ray flares. We use this process and the mildly-relativistic region in which it occurs as a discriminant between the traditional approach and our binary system approach: we use the X-ray flare properties as a discriminant between our BdHN and the “fireball” GRB models.

11.2. Conclusions

We have reached three major results.

1) We have searched X-ray flares in all GRBs and identified 16 of them with excellent data. After examining the seven GRB subclasses (Ruffini et al. 2016a), we conclude that they all occur in BdHNe and no X-ray flares are observed in other GRB sources. This indicates a link between the occurrence of the flare and the formation of a Black Hole in long GRBs. In Sec. 4 we have shown how the previously proposed association of X-ray flares with short GRBs 050724 and 050709 has been superseded.

By a statistical analysis we correlate the time of occurrence of their peak luminosity in the cosmological rest frame, their duration, their energy, their X-ray luminosity to the corresponding GRB E_{iso} . We also correlate the energy of the FPA phase, E_{FPA} , as well as the relative ratio E_{FPA}/E_{iso} , to the E_{iso} .

2) Using the data from the associated thermal emission, the relativistic relation between the co-moving time, the arrival time at the detector, the cosmological and Doppler corrections, we determine the thermal emitter effective radii as a function of the rest frame time. We determine the expansion velocity of the emitter β as the ratio between the variation of the emitter effective radius ΔR_{lab} and the emission duration in the Laboratory time; see Eq. (25). We obtain a radius 10^{12} cm for the effective radius of the emitter, moving with $\Gamma \lesssim 4$ at a time ~ 100 s in the rest frame (see Tab. 8). These results show the clear rupture between the processes in the prompt emission phase, occurring prior to the flares at radii of the order of 10^{16} cm and $\Gamma = 10^2\text{--}10^3$, and the ones of the X-ray flares.

3) We have modeled the X-ray flares by considering the impact of the GRB on the SN ejecta introducing a new set of relativistic hydrodynamic equations for the expansion of the optically thick e^+e^- plasma into a medium with baryon load in the range $10\text{--}10^2$. The matter density and velocity profiles of the ejecta are obtained from the 1D core-collapse code developed at Los Alamos (Fryer et al. 1999). With this we generate initial conditions for our smoothed-particle-hydrodynamics-like simulation (Becerra et al. 2016) which follows the evolution of the ejecta matter and the accretion rate at the position of the Bondi-Hoyle surface of the NS binary companion. In our simulations we have adopted 16 million particles (see Section 10 for further details). We start the simulation of the interaction of the e^+e^- plasma with such ejecta at 10^{10} cm and continue all the way to 10^{12} cm where transparency is reached. We found full agreement between the radius of the emitter at transparency and the one derived from the observations, as well as between the time of the peak energy emission and the observed time of arrival of the flare, derived following Eq. (2) using the computed Lorentz Γ factor of the worldline of the process.

We can now conclude that:

The existence of such mildly relativistic Lorentz gamma factors in the FPA phase rules out the traditional GRB model, including the claims of the existence of GRB beaming, collimation and break in the luminosity (see, e.g., Piran 1999; Frail et al. 2001; Mészáros 2002; Piran 2004; Mészáros 2006; Berger 2014; Kumar & Zhang 2015). In these models the common underlying assumption is the existence of a single ultra-relativistic component extending from the prompt radiation, through the FPA phase, all the way to the late afterglow and to the GeV emission assuming a common dynamics solely described by the Blandford & McKee (1976) solution, see however Bianco & Ruffini (2005b, 2006). These assumptions were made without ever looking for observational support. It is not surprising that all GRB models in the current literature purport the existence of an ultra-relativistic Lorentz gamma factor extending into the afterglow, among many others, see e.g., Jin et al. (2010); Yi et al. (2015). All these claims have been disproven by the present article, where a drastic break from the ultra-relativistic physics with $\Gamma \sim 10^2\text{--}10^3$, occurring in the prompt emission, is indicated already at times ~ 100 s, when the Lorentz gamma factor is limited to $\Gamma \leq 4$.

In our approach a multi-episode structure for each GRB is necessary. Each episode, being characterized by a different physical process, leads to a different worldline with a specific Lorentz gamma factor at each event. The knowledge of the worldline is essential, following Eq. (2) in Sec. 3, to compute the arrival time of the signals in the observer

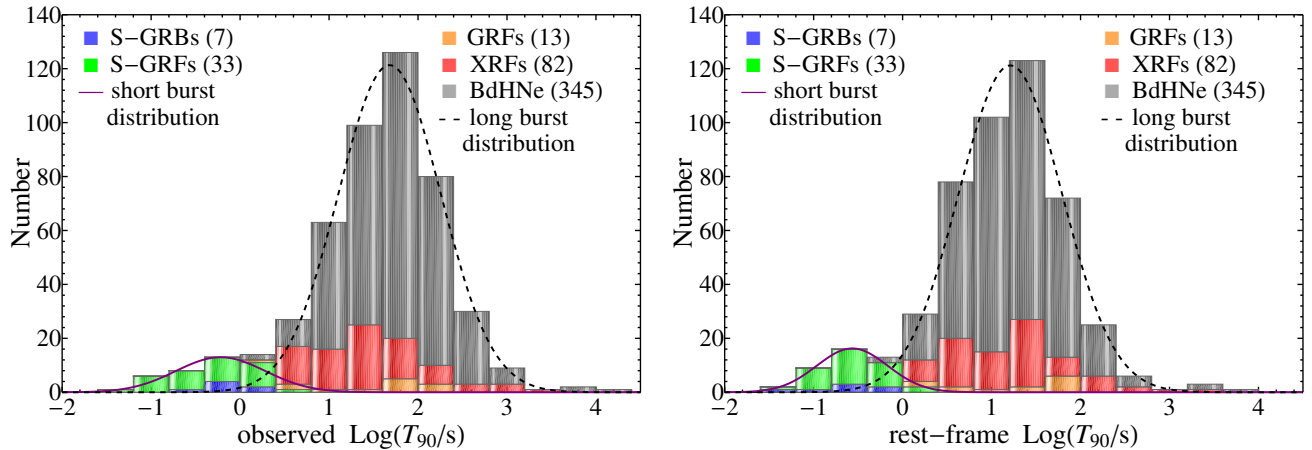


Figure 38. Histograms of T_{90} distributions in the observer frame (left panel, which is the traditional treatment widely adopted in many previous articles, see e.g. Kouveliotou et al. 1993; Bromberg et al. 2013, and references therein) and in the cosmological rest frame (right panel, which is the approach adopted in the present paper). Both histograms are built using the total number of GRBs with known redshift. The contribution to the total distributions and the number of sources of each subclass are highlighted in the legend (the choice of the colors is the same as in Fig. 4). The short burst (solid purple curve) and the long burst (dashed black curve) distributions are also shown. In the observer frame we obtain $T_{90}^{\text{short}} = 0.60_{-0.41}^{+1.31}$ s and $T_{90}^{\text{long}} = 48_{-35}^{+133}$ s; in the cosmological rest frame we have $T_{90}^{\text{short}} = 0.27_{-0.16}^{+0.41}$ s and $T_{90}^{\text{long}} = 16_{-12}^{+46}$ s. The T_{90} value discriminating between short and long bursts shifts from ≈ 2 s in the observer frame, to ≈ 0.75 s in the cosmological rest frame. The existence of BdHNe with $T_{90} \gtrsim 10^2$ s indicates the origin of the possible contamination between the prompt emission spikes and the X-ray flares, which is indeed observed in some cases (see Sec. 4 for details).

frame and compare with the observations. This procedure, previously routinely adopted in the prompt emission phase of BdHN, has for the first time been introduced here for the X-ray flares. As a byproduct we have confirmed both the binarity and the nature of the progenitors of the BdHNe, composed of a CO_{core} undergoing a SN explosion and accreting onto a close-by binary NS and impact of the GRB on the hypernova ejecta.

11.3. Perspectives

Far from representing solely a criticism of the traditional approach, in this paper: 1) we exemplify new procedures in data analysis, see Sec. 4 to Sec. 7, 2) we open up the topic to an alternative style of conceptual analysis which adopts procedures well tested in high energy physics and not yet appreciated in the astrophysical community, see Sec. 8 to Sec. 10, and 3) we introduce new tools for simulation techniques affordable with present day large computer facilities, see figures in Sec. 11, which, if properly guided by a correct theoretical understanding, can be particularly helpful in the visualization of these phenomena.

We give three specific examples of our new approach and indicate as well, when necessary, some disagreements with current approaches:

- A) The first step in any research on GRBs is to represent the histogram of the T_{90} for the GRB subclasses. We report in Fig. 38 the T_{90} values for all the GRB subclasses we have introduced (see Ruffini et al. 2016a). The values reported are both in the observer frame (left panel; see, e.g., Kouveliotou et al. 1993; Bromberg et al. 2013) and properly converted to the cosmological rest frame of the sources (right panel). The large majority of papers on GRBs have been neglecting the cosmological corrections and subdivision in the subclasses, making impossible the comparison of the T_{90} among different GRBs (see e.g. Falcone et al. 2007; Chincarini et al. 2010).
- B) For the first time, we present a simplified space-time diagram of the BdHNe (see Fig. 39). This space-time diagram emphasizes the many different emission episodes, each one with distinct corresponding Lorentz gamma factors and consequently leading through Eq. (2) to a specific value of their distinct times of occurrence in the cosmological rest frame of the GRB (see Fig. 39). In all Episodes we analyzed for the X-ray flares, and more generally for the entire FPA phase, there is no need for collapsar related concepts. Nevertheless, in view of the richness of the new scenario in Fig. 39, we have been examining the possibility that such concepts can play a role in additional Episodes, either in BdHNe or in any of the additional six GRB sub-classes, e.g. in S-GRBs. These

results are being submitted for publication. The use of space-time diagrams in the description of GRBs is indeed essential in order to illustrate the causal relation between the source in each episode, the place of occurrence and the time at detection. Those procedures have been introduced long ago in the study of high energy particle physics processes and codified in textbooks. Our group, since the basic papers (Ruffini et al. 2001a,b,c) has widely shared these space-time formulations (see e.g. in Taylor & Wheeler 1992) and also extended the concept of the quantum S-Matrix (Heisenberg 1943; Wheeler 1937) to the classic astrophysical regime of the many components of a BdHN introducing the concept of the cosmic matrix (Ruffini et al. 2015b). The majority of astrophysicists today make wide use of the results of nuclear physics in the study of stellar evolution (Bethe 1991) and of Fermi statistics also in general relativity (Oppenheimer & Volkoff 1939). They have not yet been ready, however, to approach these additional concepts more typical of relativistic astrophysics and relativistic field theories which are necessary for the study of GRBs and active galactic nuclei.

- C) The visual representation of our result (see Fig. 40) have been made possible thanks to the simulations of SN explosions with the core-collapse SN code developed at Los Alamos (see e.g. Frey et al. 2013; Fryer et al. 1999, 2014), the smoothed-particle-hydrodynamics-like simulations of the evolution of the SN ejecta accounting for the presence of a NS companion (Ruffini et al. 2016a), and the possibility to vary the parameters of the NS, of the SN, and of the distance between the two to explore all possibilities (Becerra et al. 2015; Ruffini et al. 2016a). We recall that these signals occur in each galaxy every \sim hundred million years, but with their luminosity $\sim 10^{54}$ erg they can be detected in all 10^9 galaxies. The product of these two factors give the “once per day” rate. They are not visualizable in any other way, but analyzing the spectra and time of arrival of the photons now, and simulating these data on the computer: they indeed already occurred billions of years ago in our past light cone, and they are revived by scientific procedures today.

We are happy to acknowledge fruitful discussions with Fulvio Melia, Tsvi Piran and Bing Zhang, in our attempt to make these new results clearer for a broader audience, and with Roy Kerr on the implication of GRB GeV emission for the Kerr-Newman solution. We also thank the second referee for important suggestions. We acknowledge the continuous support of the MAECI. This work made use of data supplied by the UK Swift Science Data Center at the University of Leicester. M. Ka. and Y.A. are supported by the Erasmus Mundus Joint Doctorate Program Grant N. 2014–0707 from EACEA of the European Commission. M.M. and J.A.R. acknowledge the partial support of the project N 3101/GF4 IPC-11, and the target program F.0679 0073-6/PTsF of the Ministry of Education and Science of the Republic of Kazakhstan.

APPENDIX

A. THE COMPLETE LIST OF THE BDHNE

We present here in Tab. 9 the complete list of the 345 BdHNe observed up through the end of 2016, which includes the 161 BdHNe already presented in Pisani et al. (2016).

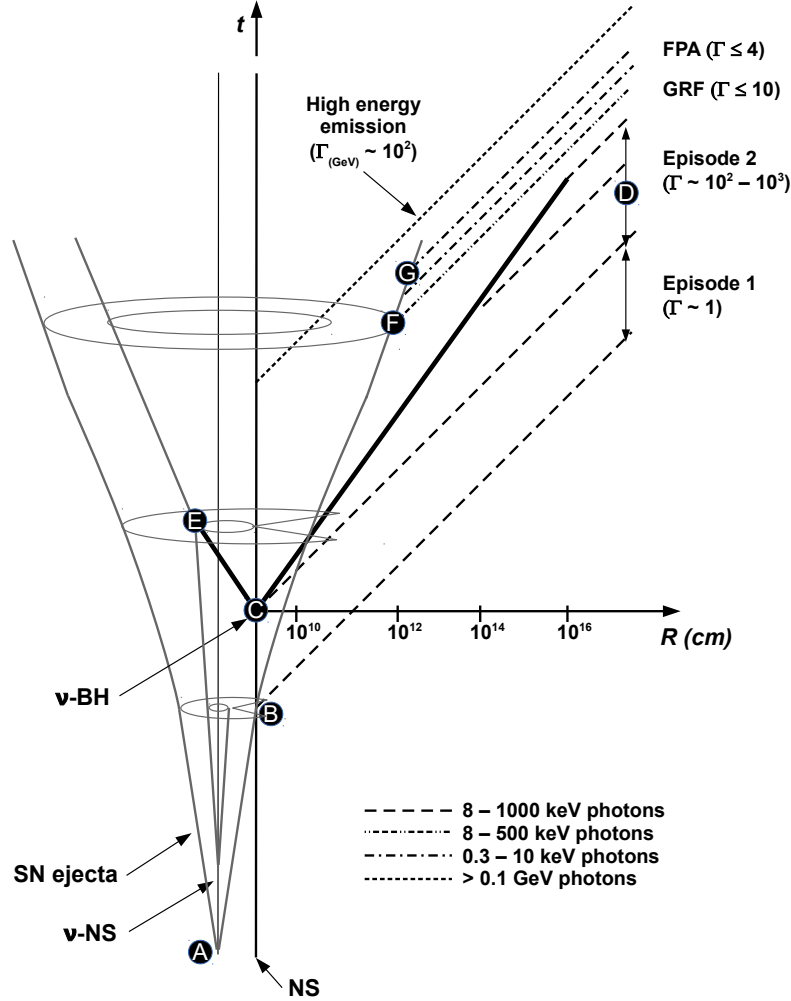


Figure 39. Space-time diagram (not in scale) of BdHNe. The CO_{core} explodes as a SN at point A and forms a new NS (νNS). The companion NS (bottom right line) accretes the SN ejecta starting from point B, giving rise to the non-relativistic Episode 1 emission (with Lorentz factor $\Gamma \approx 1$). At the point C the NS companion collapses into a BH, and an e^+e^- plasma — the dyadosphere — is formed (Ruffini et al. 1999). The following self-acceleration process occurs in a spherically symmetric manner (thick black lines). A large portion of plasma propagates in the direction of the line of sight, where the environment is cleared by the previous accretion into the NS companion, finding a baryon load $B \lesssim 10^{-2}$ and leading to the GRB prompt gamma-ray spikes (GRS, Episode 2, point D) with $\Gamma \sim 10^2 - 10^3$. The remaining part of the plasma impacts with the high density portion of the SN ejecta (point E), propagates inside the ejecta encountering a baryon load $B \sim 10^1 - 10^2$, and finally reaches transparency, leading to the gamma-ray flare emission (point F) in gamma rays with an effective Lorentz factor $\Gamma \lesssim 10$ and to the FPA emission (point G) corresponding to the X-ray Flares with an effective $\Gamma \lesssim 4$ (see Secs. 9 and 10). In the meantime, accretion over the newly formed BH produces the high energy GeV emission with $\Gamma \sim 10^2$. For simplicity, this diagram is 2D and static and does not attempt to show the 3D rotation of the ejecta.

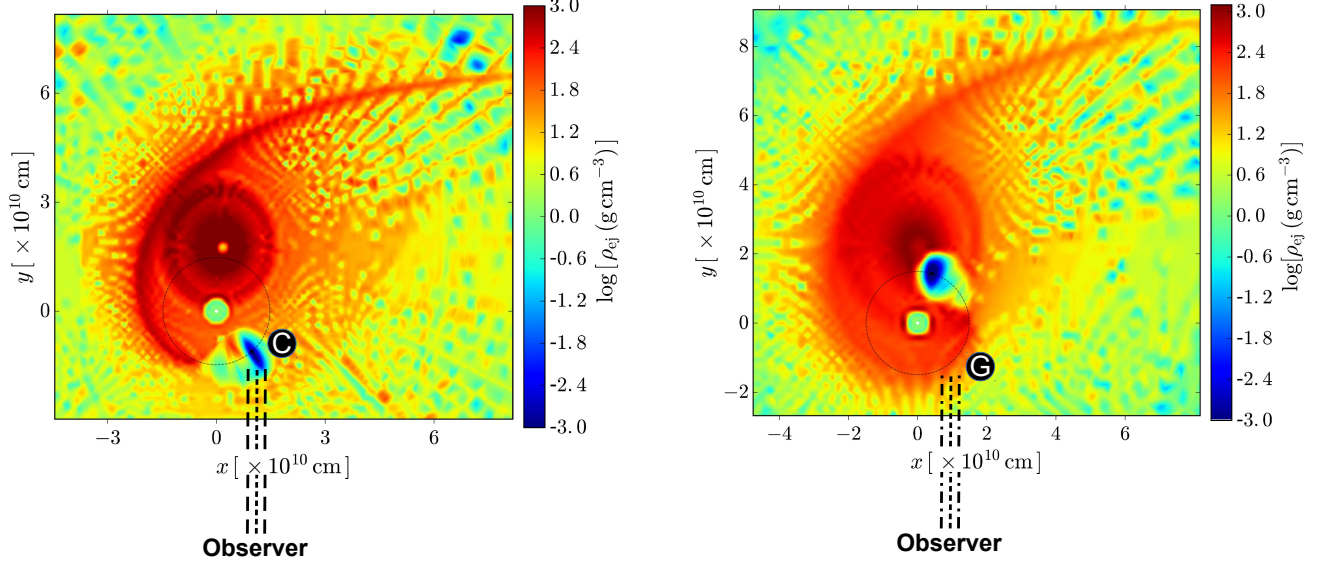


Figure 40. Two snapshots of the distribution of matter in the equatorial plane of the progenitor binary system. The one on the right side corresponds to point C, when the BH is formed and a large portion of the e^+e^- plasma starts to self-accelerate in a low density environment ($B \lesssim 10^{-2}$) toward the observer producing the GRB prompt emission. The one on the left side corresponds to point G, when the remaining part of the plasma, after the propagation inside the high density SN ejecta ($B \sim 10^2-10^3$), reaches transparency and produces the FPA emission in the X-rays which is directed toward the observer due to the rotation of the ejecta in the equatorial plane. The simulations of the matter distributions in the three snapshots are from Becerra et al. (2016).

Table 9. List of the BdHNe considered in this work. It is composed by 345 sources spanning 12 years of Swift/XRT observation activity. In the table we report important observational features: the redshift z , the isotropic energy E_{iso} , the observing instrument in the gamma-ray band, and the correspondent reference from which we take the gamma-ray spectral parameters in order to estimate E_{iso} .

(^a): in units of 10^{52} erg.

(^b): “LX” marks the sources with Swift/XRT data observed up to times larger than 10^4 s in the rest-frame after the initial explosion.

(^c): “C” and “E” mark the sources showing an early flare in their Swift/XRT, and they stay for “confirmed” and “excluded” respectively. The 16 C sources compose the sample considered in the present paper.

(^d): “UL” stays for ultra-long, indicating sources with $T_{90} \gtrsim 1000$ s.

(^e): observed T_{90} (s).

(^f): “B-SAX” stays for Beppo-SAX/GRBM; “BATSE” stays for Compton-GRO/BATSE; “Ulysses” stays for Ulysses/GRB; “KW” stays for Konus-WIND; “HETE” stays for HETE-2/FREGATE; “Swift” stays for Swift/BAT; “Fermi” stays for Fermi/GBM.

(^g): (1) Frontera et al. (1998); (2) Ruffini et al. (2015c); (3) in ’t Zand et al. (1998); (4) Amati et al. (2000); (5) Hurley et al. (2000); (6) in’t Zand et al. (2001); (7) Barraud et al. (2003); (8) Shirasaki et al. (2008); (9) Cenko et al. (2006).

GRB	z	$E_{iso}^{(a)}$	LX ^(b)	Early flare ^(c)	UL ^(d)	$T_{90}^{(e)}$	Instrument ^(f)	Reference ^(g)
970228	0.695	1.65 ± 0.16				80	B-SAX	(1)
970828	0.958	30.4 ± 3.6				90	BATSE	(2)

Table 9. continued.

GRB	z	$E_{iso}^{(a)}$	LX ^(b)	Early flare ^(c)	UL ^(d)	$T_{90}^{(e)}$	Instrument ^(f)	Reference ^(g)
971214	3.42	22.1 ± 2.7				40	BATSE	IAUC 6789
980329	3.5	267 ± 53				54	B-SAX	(3)
980703	0.966	7.42 ± 0.74				400	BATSE	GCN 143
990123	1.6	241 ± 39				63.3	BATSE	GCN 224
990506	1.3	98.1 ± 9.9				131.33	BATSE	GCN 306
990510	1.619	18.1 ± 2.7				75	BATSE	GCN 322
990705	0.842	18.7 ± 2.7				42	B-SAX	(4)
991208	0.706	23.0 ± 2.3				68	Ulysses	(5)
991216	1.02	69.8 ± 7.2				15.17	BATSE	GCN 504
000131	4.5	184 ± 32				50	KW+Ulysses	GCN 529
000210	0.846	15.4 ± 1.7				12.3	BATSE	GCN 540
000301C	2.0335	4.96 ± 0.50				10	Ulysses	GCN 568
000418	1.12	9.5 ± 1.8				30	KW+Ulysses	GCN 642
000911	1.06	70 ± 14				500	KW+Ulysses	GCN 791
000926	2.07	28.6 ± 6.2				25	KW+Ulysses	GCN 801
010222	1.48	84.9 ± 9.0				170	B-SAX	(6)
010921	0.45	0.97 ± 0.10				12	HETE	GCN 1096
011121	0.36	8.0 ± 2.2				28	Ulysses	GCN 1148
011211	2.14	5.74 ± 0.64				270	B-SAX	GCN 1215
020124	3.2	28.5 ± 2.8				78.6	HETE	(7)
020127	1.9	3.73 ± 0.37				9.3	HETE	(7)
020405	0.69	10.6 ± 1.1				40	KW+Ulysses	GCN 1325
020813	1.25	68 ± 17				90	HETE	(7)
021004	2.3	3.47 ± 0.46				57.7	HETE	(7)
021211	1.01	1.16 ± 0.13				5.7	HETE	GCN 1734
030226	1.98	12.7 ± 1.4				100	HETE	GCN 1888
030323	3.37	2.94 ± 0.92				26	HETE	GCN 1956
030328	1.52	38.9 ± 3.9				100	HETE	GCN 1978
030329	0.169	1.62 ± 0.16				50	HETE	IAUC 8101
030429	2.65	2.29 ± 0.27				14	HETE	GCN 2211
030528	0.78	2.22 ± 0.27				21.6	HETE	GCN 2256
040912	1.563	1.36 ± 0.36				122	HETE	GCN 2723
040924	0.859	0.98 ± 0.10				2.4	KW	GCN 2754
041006	0.716	3.11 ± 0.89				27.3	HETE	(8)
041219A	0.31	10.0 ± 1.0				520	Swift	GCN 2874
050126	1.29	2.47 ± 0.25				26	Swift	GCN 2987
050315	1.95	6.15 ± 0.30	LX			96	Swift	GCN 3099
050318	1.444	2.30 ± 0.23	LX			32	Swift	GCN 3134
050319	3.243	$4.63 \pm .056$	LX			10	Swift	GCN 3119

Table 9. continued.

GRB	z	$E_{iso}^{(a)}$	LX ^(b)	Early flare ^(c)	UL ^(d)	$T_{90}^{(e)}$	Instrument ^(f)	Reference ^(g)
050401	2.898	37.6 ± 7.3	LX			33	KW	GCN 3179
050408	1.2357	2.48 ± 0.25	LX			34	HETE	GCN 3188
050502B	5.2	2.66 ± 0.22				17.5	Swift	GCN 3339
050505	4.27	16.0 ± 1.1	LX			60	Swift	GCN 3364
050525A	0.606	2.30 ± 0.49	LX			5.2	KW	GCN 3479
050603	2.821	64.1 ± 6.4				6	KW	GCN 3518
050714B	2.4383	4.99 ± 0.85				46.7	Swift	GCN 3615
050730	3.969	11.8 ± 0.8	LX			155	Swift	GCN 3715
050802	1.71	5.66 ± 0.47	LX			13	Swift	GCN 3737
050803	4.3	1.16 ± 0.12	LX	E		85	Swift	GCN 3757
050814	5.3	9.9 ± 1.1	LX			65	Swift	GCN 3803
050819	2.5043	3.60 ± 0.55				36	Swift	GCN 3828
050820	2.615	103 ± 10	LX			549.2	KW	(9)
050822	1.434	10.8 ± 1.1	LX	E		102	Swift	GCN 3856
050904	6.295	133 ± 14				225	Swift	GCN 3938
050908	3.347	1.54 ± 0.16				20	Swift	GCN 3951
050915	2.5273	1.8 ± 1.3				53	Swift	GCN 3982
050922B	4.9	46.4 ± 4.6	LX	E		980	Swift	GCN 4019
050922C	2.199	5.6 ± 1.8	LX			8.4	KW	GCN 4030
051001	2.4296	2.3 ± 1.7				190	Swift	GCN 4052
051006	1.059	1.02 ± 0.56				26	Swift	GCN 4063
051008	2.77	115 ± 20				280	KW	GCN 4078
051022	0.8	56.0 ± 5.6				200	KW	GCN 4150
051109A	2.346	6.85 ± 0.73	LX			130	KW	GCN 4238
051111	1.55	15.4 ± 1.9				47	KW	GCN 4260
060108	2.03	1.51 ± 1.33	LX			14.4	Swift	GCN 4445
060111	2.32	1.62 ± 0.08	LX	E		13	Swift	GCN 4486
060115	3.533	5.9 ± 3.8	LX			142	Swift	GCN 4518
060124	2.296	43.8 ± 6.4	LX			300	KW	GCN 4599
060202	0.785	1.20 ± 0.09	LX			203.7	Swift	GCN 4635
060204B	2.3393	29.3 ± 6.0	LX	C		134	Swift	GCN 4671
060206	4.056	4.1 ± 1.9	LX			7	Swift	GCN 4697
060210	3.91	32.2 ± 3.2	LX			255	Swift	GCN 4748
060223	4.41	9.73 ± 0.72				11	Swift	GCN 4820
060306	3.5	7.6 ± 1.0				61	Swift	GCN 4851
060418	1.489	13.5 ± 2.7	LX			52	Swift	GCN 4975
060502A	1.51	10.57 ± 0.48	LX			33	Swift	GCN 5053
060510B	4.9	19.1 ± 0.8	LX			276	Swift	GCN 5107
060512	2.1	2.38 ± 2.70	LX			8.6	Swift	GCN 5124

Table 9. continued.

GRB	z	$E_{iso}^{(a)}$	LX ^(b)	Early flare ^(c)	UL ^(d)	$T_{90}^{(e)}$	Instrument ^(f)	Reference ^(g)
060522	5.11	6.47 ± 0.63				69	Swift	GCN 5153
060526	3.22	2.75 ± 0.37	LX			298	Swift	GCN 5174
060602A	0.787	6.63 ± 0.41				60	Swift	GCN 5206
060605	3.773	4.23 ± 0.61	LX			15	Swift	GCN 5231
060607A	3.082	21.4 ± 11.9	LX	C		100	Swift	GCN 5242
060707	3.424	4.3 ± 1.1	LX			68	Swift	GCN 5289
060708	1.92	1.06 ± 0.08	LX			9.8	Swift	GCN 5295
060714	2.7108	7.67 ± 0.44	LX			115	Swift	GCN 5334
060719	1.532	1.4 ± 1.3				55	Swift	GCN 5349
060729	0.54	1.20 ± 0.53	LX	E		116	Swift	GCN 5370
060814	1.923	56.7 ± 5.7	LX			40	KW	GCN 5460
060906	3.6856	7.81 ± 0.51	LX			43.6	Swift	GCN 5538
060908	1.884	7.2 ± 1.9				19.3	Swift	GCN 5551
060923B	1.5094	2.71 ± 0.34				8.8	Swift	GCN 5595
060926	3.2086	2.29 ± 0.37				8	Swift	GCN 5621
060927	5.46	12.0 ± 2.8				22.6	Swift	GCN 5639
061007	1.262	90.0 ± 9.0	LX			75	KW	GCN 5722
061110B	3.4344	17.9 ± 1.6				128	Swift	GCN 5810
061121	1.314	23.5 ± 2.7	LX			81	Swift	GCN 5831
061126	1.1588	31.4 ± 3.6	LX			191	Swift	GCN 5860
061202	2.2543	21.99 ± 0.63				91	Swift	GCN 5887
061222A	2.088	30.0 ± 6.4	LX			72	Swift	GCN 5964
061222B	3.355	8.1 ± 1.5				40	Swift	GCN 5974
070110	2.3521	4.98 ± 0.30	LX			85	Swift	GCN 6007
070125	1.547	84.1 ± 8.4				75	Swift	GCN 6049
070129	2.3384	16.8 ± 1.7	LX	E		460	Swift	GCN 6058
070223	1.6295	4.73 ± 0.28				89	Swift	GCN 6132
070224	1.9922	2.37 ± 0.28				34	Swift	GCN 6141
070306	1.4959	8.26 ± 0.41	LX			210	Swift	GCN 6173
070318	0.84	3.41 ± 2.14	LX	C		63	Swift	GCN 6212
070328	2.0627	56.7 ± 7.7				45	KW	GCN 6230
070411	2.954	8.31 ± 0.45				101	Swift	GCN 6274
070419B	1.959	12.1 ± 1.7				236.5	Swift	GCN 6327
070508	0.82	7.74 ± 0.29	LX			40	KW	GCN 6403
070521	1.35	10.8 ± 1.8				55	KW	GCN 6459
070529	2.4996	12.8 ± 1.1	LX			109	Swift	GCN 6468
070611	2.0394	0.92 ± 0.13				12	Swift	GCN 6502
070612A	0.617	1.96 ± 0.40				370	Swift	GCN 6522
070721B	3.6298	24.2 ± 1.4				340	Swift	GCN 6649

Table 9. continued.

GRB	z	$E_{iso}^{(a)}$	LX ^(b)	Early flare ^(c)	UL ^(d)	$T_{90}^{(e)}$	Instrument ^(f)	Reference ^(g)
070802A	2.45	1.65 ± 2.78	LX			16.4	Swift	GCN 6699
070810A	2.17	91.5 ± 1.1				11	Swift	GCN 6748
071003	1.604	38.3 ± 4.5	LX			30	KW	GCN 6849
071010B	0.947	2.32 ± 0.40				16.6	KW	GCN 6879
071020	2.145	10.0 ± 4.6				8.45	KW	GCN 6960
071021	2.452	8.18 ± 0.82	LX	E		225	Swift	GCN 6966
071025	5.2	115 ± 4				109	Swift	GCN 6996
071031	2.6918	4.99 ± 0.97				180	Swift	GCN 7029
071112C	0.823	15.7 ± 2.1				15	Swift	GCN 7081
071117	1.331	5.86 ± 2.7				5	KW	GCN 7114
080129	4.349	7.7 ± 3.5				48	Swift	GCN 7235
080205	2.72	15.21 ± 0.72				106.5	Swift	GCN 7257
080207	2.0858	16.4 ± 1.8				340	Swift	GCN 7272
080210	2.6419	4.77 ± 0.29	LX			45	Swift	GCN 7289
080310	2.4274	20.9 ± 2.1	LX	E		365	Swift	GCN 7402
080319A	2.0265	27.0 ± 2.2				64	Swift	GCN 7447
080319B	0.937	118 ± 12	LX			50	KW	GCN 7482
080319C	1.95	14.9 ± 3.0	LX			15	KW	GCN 7487
080325	1.78	9.55 ± 0.84				128.4	Swift	GCN 7531
080411	1.03	16.2 ± 1.6				70	KW	GCN 7589
080413A	2.433	8.6 ± 2.1				46	Swift	GCN 7604
080413B	1.1	1.61 ± 0.27				8	Swift	GCN 7606
080514B	1.8	18.1 ± 3.6				7	KW	GCN 7751
080515	2.47	5.11 ± 0.77				21	Swift	GCN 7726
080602	1.8204	6.08 ± 0.38				74	Swift	GCN 7786
080603B	2.69	6.0 ± 3.1				70	KW	GCN 7812
080604	1.4171	1.05 ± 0.12				82	Swift	GCN 7817
080605	1.64	28 ± 14	LX			20	Swift	GCN 7854
080607	3.04	187 ± 11	LX	C		85	KW	GCN 7862
080710	0.8454	1.68 ± 0.22				120	Swift	GCN 7969
080721	2.591	134 ± 23	LX			30	KW	GCN 7995
080804	2.205	12.0 ± 1.2	LX			34	Swift	GCN 8067
080805	1.51	7.16 ± 1.90	LX	C		78	Swift	GCN 8068
080810	3.35	50.0 ± 4.4	LX	C		79.4	KW	GCN 8101
080825B	4.3	38.4 ± 3.8				110	KW	GCN 8142
080905B	2.3739	4.55 ± 0.37	LX			128	Swift	GCN 8188
080906	2.1	21.2 ± 1.2				147	Swift	GCN 8196
080913	6.695	9.2 ± 2.7				8.8	KW	GCN 8280
080916A	0.689	0.98 ± 0.10				40	KW	GCN 8259

Table 9. continued.

GRB	z	$E_{iso}^{(a)}$	LX ^(b)	Early flare ^(c)	UL ^(d)	$T_{90}^{(e)}$	Instrument ^(f)	Reference ^(g)
080916C	4.35	407 ± 86	LX			60	Fermi	GCN 8263
080928	1.692	3.99 ± 0.91	LX			66	Fermi	GCN 8278
081008	1.967	13.5 ± 6.6	LX	C		185.5	Swift	GCN 8351
081028	3.038	18.3 ± 1.8	LX			260	Swift	GCN 8428
081029	3.8479	12.1 ± 1.4				270	Swift	GCN 8447
081109	0.9787	1.81 ± 0.12	LX			45	Fermi	GCN 8505
081118	2.58	12.2 ± 1.2				20	Fermi	GCN 8550
081121	2.512	32.4 ± 3.7	LX			18	KW	GCN 8548
081203A	2.05	32 ± 12	LX			213	KW	GCN 8611
081210	2.0631	15.6 ± 5.4	LX	C		146	Swift	GCN 8649
081221	2.26	31.9 ± 3.2	LX			40	Fermi	GCN 8704
081222	2.77	27.4 ± 2.7	LX			30	Fermi	GCN 8715
081228	3.44	9.9 ± 2.0				3	Swift	GCN 8749
081230	2.0	3.21 ± 0.31				60.7	Swift	GCN 8759
090102A	1.547	22.6 ± 2.7	LX			30	KW	GCN 8776
090113A	1.7493	1.00 ± 0.17				9.1	Swift	GCN 8808
090201A	2.1	93.4 ± 8.1				110	KW	GCN 8878
090205A	4.6497	1.12 ± 0.16				8.8	Swift	GCN 8886
090313A	3.375	4.42 ± 0.79	LX			78	Swift	GCN 8986
090323A	3.57	438 ± 53				150	Fermi	GCN 9035
090328A	0.736	14.2 ± 1.4	LX			80	Fermi	GCN 9057
090404A	3	59.2 ± 6.1	LX	E		84	Swift	GCN 9089
090418A	1.608	17.2 ± 2.7	LX			64.8	KW+Swift	GCN 9196
090423A	8.26	8.8 ± 2.1	LX			12	Fermi	GCN 9229
090424A	0.544	4.07 ± 0.41	LX			52	Fermi	GCN 9230
090429B	9.3	6.7 ± 1.3				5.5	Swift	GCN 9290
090516A	4.109	99.6 ± 16.7	LX	C		350	Fermi	GCN 9415
090519A	3.85	24.7 ± 2.8				64	Swift	GCN 9406
090529A	2.625	2.56 ± 0.30				100	Swift	GCN 9434
090530A	1.266	1.73 ± 0.19				48	Swift	GCN 9443
090618A	0.54	28.6 ± 2.9	LX			113.2	Fermi	GCN 9535
090715B	3.	63.9 ± 3.7	LX	E		100	KW	GCN 9679
090726A	2.71	1.82 ± 0.40				67	Swift	GCN 9716
090809A	2.737	1.88 ± 0.26	LX			5.4	Swift	GCN 9756
090812A	2.452	44.0 ± 6.5	LX	C		64.8	KW+Swift	GCN 9821
090902B	1.822	292 ± 29.2	LX			21	Fermi	GCN 9866
090926A	2.106	228 ± 23	LX			20	Fermi	GCN 9933
090926B	1.24	4.14 ± 0.45				81	Fermi	GCN 9957
091003A	0.897	10.7 ± 1.8	LX			21.1	Fermi	GCN 9983

Table 9. continued.

GRB	z	$E_{iso}^{(a)}$	LX ^(b)	Early flare ^(c)	UL ^(d)	$T_{90}^{(e)}$	Instrument ^(f)	Reference ^(g)
091020A	1.71	8.4 ± 1.1	LX			37	Fermi	GCN 10095
091024A	1.092	18.4 ± 2.0			UL	1250	KW	GCN 10083
091029A	2.752	7.97 ± 0.82	LX			39.2	Swift	GCN 10103
091109A	3.076	10.6 ± 1.4				48	Swift	GCN 10141
091127A	0.49	1.64 ± 0.18	LX			9	Fermi	GCN 10204
091208B	1.063	2.06 ± 0.21	LX			15	Fermi	GCN 10266
100219A	4.6667	3.93 ± 0.61				18.8	Swift	GCN 10434
100302A	4.813	1.33 ± 0.17	LX			17.9	Swift	GCN 10462
100414A	1.368	55.0 ± 5.5				26.4	Fermi	GCN 10595
100424A	2.465	3.05 ± 0.53				104	Swift	GCN 10670
100425A	1.755	2.76 ± 3.45	LX			37	Swift	GCN 10685
100513A	4.8	6.75 ± 0.53	LX			84	Swift	GCN 10753
100615A	1.398	5.81 ± 0.11				37.7	Fermi	GCN 10851
100621A	0.542	2.82 ± 0.35	LX			80	KW	GCN 10882
100728A	1.567	86.8 ± 8.7				162.9	Fermi	GCN 11006
100728B	2.106	3.55 ± 0.36				11.8	Fermi	GCN 11015
100814A	1.44	15.3 ± 1.8	LX			149	Fermi	GCN 11099
100816A	0.8049	0.75 ± 0.10	LX			2	Fermi	GCN 11124
100901A	1.408	4.22 ± 0.50	LX			439	Swift	GCN 11169
100906A	1.727	29.9 ± 2.9	LX			105	Fermi	GCN 11248
101213A	0.414	2.72 ± 0.53				45	Fermi	GCN 11454
110128A	2.339	1.58 ± 0.21	LX			12	Fermi	GCN 11628
110205A	2.22	48.3 ± 6.4	LX			330	KW	GCN 11659
110213A	1.46	5.78 ± 0.81	LX			33	Fermi	GCN 11727
110213B	1.083	8.3 ± 1.3				50	KW	GCN 11722
110422A	1.77	79.8 ± 8.2	LX			40	KW	GCN 11971
110503A	1.613	20.8 ± 2.1	LX			12	KW	GCN 12008
110715A	0.82	4.36 ± 0.45	LX			20	KW	GCN 12166
110731A	2.83	49.5 ± 4.9	LX			7.3	Fermi	GCN 12221
110801A	1.858	10.9 ± 2.7				415.1	KW+Swift	GCN 12276
110808A	1.348	6.09 ± 4.83	LX			48	KW	GCN 12270
110818A	3.36	26.6 ± 2.8				75	Fermi	GCN 12287
110918A	0.982	185 ± 5	LX			22	KW	GCN 12362
111008A	4.9898	24.7 ± 1.2	LX			40	KW	GCN 12433
111107A	2.893	3.76 ± 0.55				12	Fermi	GCN 12545
111123A	3.1516	24 ± 14	LX			290	Swift	GCN 12598
111209A	0.677	5.14 ± 0.62	LX		UL	11900	KW	GCN 12663
111215A	2.06	22.1 ± 2.5				796	Swift	GCN 12689
111228A	0.716	2.75 ± 0.28	LX			101.2	Fermi	GCN 12744

Table 9. continued.

GRB	z	$E_{iso}^{(a)}$	LX ^(b)	Early flare ^(c)	UL ^(d)	$T_{90}^{(e)}$	Instrument ^(f)	Reference ^(g)
120118B	2.943	6.24 ± 0.55				23.26	Swift	GCN 12873
120119A	1.728	27.2 ± 3.6	LX			55	Fermi	GCN 12874
120211A	2.4	7.1 ± 1.0				61.7	Swift	GCN 12924
120326A	1.798	3.27 ± 0.33	LX			12	Fermi	GCN 13145
120327A	2.813	14.42 ± 0.46	LX			62.9	Swift	GCN 13137
120404A	2.876	4.18 ± 0.34				38.7	Swift	GCN 13220
120521C	6.01	11.9 ± 1.9				26.7	Swift	GCN 13333
120624B	2.197	319 ± 32				271	Fermi	GCN 13377
120711A	1.405	180 ± 18	LX			44	Fermi	GCN 13437
120712A	4.175	21.2 ± 2.1	LX			23	Fermi	GCN 13469
120716A	2.486	30.2 ± 3.0				234	Fermi	GCN 13498
120802A	3.796	12.9 ± 2.8				50	Swift	GCN 13559
120805A	3.1	19.0 ± 3.2				48	Swift	GCN 13594
120811C	2.671	6.41 ± 0.64				26.8	Swift	GCN 13634
120815A	2.358	1.65 ± 0.27				9.7	Swift	GCN 13652
120909A	3.93	87 ± 10	LX			112	Fermi	GCN 13737
120922A	3.1	22.4 ± 1.4	LX			180	Fermi	GCN 13809
121024A	2.298	4.61 ± 0.55	LX			69	Swift	GCN 13899
121027A	1.773	1.50 ± 0.17	LX	E	UL	6000	Swift	GCN 13910
121128A	2.2	8.66 ± 0.87	LX			17	Fermi	GCN 14012
121201A	3.385	2.52 ± 0.34				85	Swift	GCN 14028
121209A	2.1	24.31 ± 0.84				42.7	Swift	GCN 14052
121217A	3.1	25.9 ± 19.7	LX			780	Fermi	GCN 14094
121229A	2.707	3.7 ± 1.1				100	Swift	GCN 14123
130408A	3.758	35.0 ± 6.4				15	KW	GCN 14368
130131B	2.539	7.15 ± 0.84				4.3	Swift	GCN 14164
130215A	0.597	4.45 ± 0.11				140	Fermi	GCN 14219
130408A	3.757	35.4 ± 5.9				15	KW	GCN 14368
130418A	1.218	9.9 ± 1.6	LX			120	KW	GCN 14417
130420A	1.297	7.74 ± 0.77	LX			102	Fermi	GCN 14429
130427A	0.334	92 ± 13	LX			162.8	Fermi	GCN 14473
130427B	2.78	13.3 ± 0.5	LX	E		27	Swift	GCN 14469
130505A	2.27	347 ± 35	LX			21	KW	GCN 14575
130514A	3.6	49.5 ± 9.2	LX	E		204	Swift	GCN 14636
130518A	2.488	193 ± 19				48	Fermi	GCN 14674
130528A	1.25	18.0 ± 2.3	LX	E		55	Fermi	GCN 14729
130606A	5.91	28.3 ± 5.1	LX	E		165	KW	GCN 14808
130610A	2.092	6.99 ± 0.46	LX			28	Fermi	GCN 14858
130701A	1.155	2.60 ± 0.09	LX			5.5	KW	GCN 14958

Table 9. continued.

GRB	z	$E_{iso}^{(a)}$	LX ^(b)	Early flare ^(c)	UL ^(d)	$T_{90}^{(e)}$	Instrument ^(f)	Reference ^(g)
130907A	1.238	304 ± 19	LX			214	KW	GCN 15203
130925A	0.347	3.23 ± 0.37	LX	E	UL	4500	Fermi	GCN 15261
131011A	1.874	86.67 ± 0.39				77	Fermi	GCN 15331
131030A	1.293	30.0 ± 2.0	LX	C		28	KW	GCN 15413
131105A	1.686	34.7 ± 1.2	LX			112	Fermi	GCN 15455
131108A	2.4	70.87 ± 0.97	LX			19	Fermi	GCN 15477
131117A	4.042	1.02 ± 0.16	LX			11	Swift	GCN 15499
131227A	5.3	24.2 ± 1.7				18	Swift	GCN 15620
140114A	3.0	27.6 ± 0.8	LX	E		139.7	Swift	GCN 15738
140206A	2.73	35.8 ± 7.9	LX	C		27	Fermi	GCN 15796
140213A	1.2076	9.93 ± 0.15	LX			18.6	Fermi	GCN 15833
140226A	1.98	5.8 ± 1.1	LX			15	KW	GCN 15889
140301A	1.416	0.95 ± 0.18	LX	C		31	Swift	GCN 15906
140304A	5.283	15.3 ± 1.1	LX	E		32	Fermi	GCN 15923
140311A	4.954	11.6 ± 1.5	LX			71.4	Swift	GCN 15962
140419A	3.956	185 ± 77	LX	C		80	KW	GCN 16134
140423A	3.26	65.3 ± 3.3	LX			95	Fermi	GCN 16152
140428A	4.7	1.88 ± 0.31				17.42	Swift	GCN 16186
140430A	1.6	1.54 ± 0.23				173.6	Swift	GCN 16200
140506A	0.889	7.75 ± 0.80	LX	E		64	Fermi	GCN 16220
140508A	1.027	23.24 ± 0.26	LX			44.3	Fermi	GCN 16224
140509A	2.4	3.77 ± 0.44	LX			23.2	Swift	GCN 16240
140512A	0.725	7.76 ± 0.18	LX			148	Fermi	GCN 16262
140515A	6.32	5.41 ± 0.55				23.4	Swift	GCN 16284
140518A	4.707	5.89 ± 0.59				60.5	Swift	GCN 16306
140614A	4.233	7.3 ± 2.1	LX			720	Swift	GCN 16402
140620A	2.04	6.28 ± 0.24	LX			46	Fermi	GCN 16426
140623A	1.92	7.69 ± 0.68				110	Fermi	GCN 16450
140629A	2.275	6.15 ± 0.90	LX			26	KW	GCN 16495
140703A	3.14	1.72 ± 0.09	LX			84	Fermi	GCN 16512
140801A	1.32	5.69 ± 0.05				7	Fermi	GCN 16658
140808A	3.29	11.93 ± 0.75				4.7	Fermi	GCN 16669
140907A	1.21	2.29 ± 0.08	LX			35	Fermi	GCN 16798
141026A	3.35	7.17 ± 0.90	LX			146	Swift	GCN 16960
141028A	2.33	68.9 ± 0.02				31.5	Fermi	GCN 16971
141109A	2.993	33.1 ± 6.9	LX			94	KW	GCN 17055
141121A	1.47	14.2 ± 1.1	LX		UL	1200	KW	GCN 17108
141220A	1.3195	2.44 ± 0.07				7.6	Fermi	GCN 17205
141221A	1.47	6.99 ± 1.98	LX	C		23.8	Fermi	GCN 17216

Table 9. continued.

GRB	z	$E_{iso}^{(a)}$	LX ^(b)	Early flare ^(c)	UL ^(d)	$T_{90}^{(e)}$	Instrument ^(f)	Reference ^(g)
141225A	0.915	2.29 ± 0.11				56	Fermi	GCN 17241
150120B	3.5	7.37 ± 1.09	LX			24.3	Swift	GCN 17330
150206A	2.087	55.6 ± 20.1	LX			60	KW	GCN 17427
150301B	1.5169	2.87 ± 0.42	LX			13	Fermi	GCN 17525
150314A	1.758	95.2 ± 3.1	LX			10.7	Fermi	GCN 17579
150323A	0.593	1.30 ± 0.30				38	KW	GCN 17640
150403A	2.06	98.1 ± 6.3	LX			22.3	Fermi	GCN 17674
150413A	3.139	49.80 ± 7.01				263.6	KW+Swift	GCN 17731
150821A	0.755	14.7 ± 1.1	LX			103	Fermi	GCN 18190
150910A	1.359	21.6 ± 1.8	LX			112.2	Swift	GCN 18268
151021A	2.33	112.2 ± 35	LX			100	KW	GCN 18433
151027A	0.81	3.94 ± 1.33	LX	C		124	Fermi	GCN 18492
151027B	4.063	18.6 ± 3.7	LX			80	Swift	GCN 18514
151111A	3.5	3.43 ± 1.19	LX	E		40	Fermi	GCN 18582
151112A	4.1	12.1 ± 1.5	LX			19.32	Swift	GCN 18593
151215A	2.59	1.89 ± 0.43	LX			17.8	Swift	GCN 18699
160121A	1.96	2.54 ± 0.21	LX			12	Swift	GCN 18919
160131A	0.972	58.7 ± 32.7	LX			200	KW	GCN 18974
160203A	3.52	12.0 ± 1.0	LX			20.2	Swift	GCN 18998
160227A	2.38	5.52 ± 2.38	LX			316.5	Swift	GCN 19106
160228A	1.64	15.98 ± 0.80				98.36	Swift	GCN 19113
160509A	1.17	84.5 ± 2.3	LX			371	Fermi	GCN 19411
160623A	0.367	22.4 ± 1.5	LX			38.9	KW	GCN 19554
160625B	1.406	419.0 ± 4.8	LX			460	Fermi	GCN 19587
160629A	3.332	48.8 ± 9.9				66.6	Fermi	GCN 19628
160804A	0.736	2.46 ± 0.51	LX			130	Fermi	GCN 19769
161014A	2.823	10.1 ± 1.7				37	Fermi	GCN 20051
161017A	2.013	7.56 ± 1.55	LX			32	Fermi	GCN 20068
161023A	2.708	73.9 ± 27.5	LX			50	KW	GCN 20111
161108A	1.159	1.66 ± 0.15	LX			105.1	Swift	GCN 20151
161117A	1.549	31.2 ± 5.5	LX			122	Fermi	GCN 20192

B. PARAMETERS OF THE EQUATION OF STATE

We give here details concerning the determination of the value of the index γ and verify the accuracy of our assumption $\gamma = 4/3$ adopted in the equation of state of the plasma (30). This index is defined as:

$$\gamma \equiv 1 + \frac{p}{\epsilon}. \quad (\text{B1})$$

The total internal energy density and pressure are computed as

$$\epsilon = \epsilon_{e^-} + \epsilon_{e^+} + \epsilon_{\gamma} + \epsilon_B \quad (\text{B2})$$

$$p = p_{e^-} + p_{e^+} + p_{\gamma} + p_B, \quad (\text{B3})$$

where the subscript B indicates the contributions of the baryons in the fluid. The number and energy densities, as well as the pressure of the different particles, can be computed in natural units ($c = \hbar = k_B = 1$) using the following expressions (see, e.g., Landau & Lifshitz 1980):

$$n_{e^-} = AT^3 \int_0^\infty f(z, T, m_e, \mu_{e^-}) z^2 dz \quad (\text{B4})$$

$$n_{e^+} = AT^3 \int_0^\infty f(z, T, m_e, \mu_{e^+}) z^2 dz \quad (\text{B5})$$

$$\epsilon_{e^-} = AT^4 \int_0^\infty f(z, T, m_e, \mu_{e^-}) \sqrt{z^2 + (m_e/T)^2} z^2 dz - m_e n_{e^-} \quad (\text{B6})$$

$$\epsilon_{e^+} = AT^4 \int_0^\infty f(z, T, m_e, \mu_{e^+}) \sqrt{z^2 + (m_e/T)^2} z^2 dz - m_e n_{e^+} \quad (\text{B7})$$

$$p_{e^-} = A \frac{T^4}{3} \int_0^\infty f(z, T, m_e, \mu_{e^-}) \frac{z^4}{\sqrt{z^2 + (m_e/T)^2}} dz \quad (\text{B8})$$

$$p_{e^+} = A \frac{T^4}{3} \int_0^\infty f(z, T, m_e, \mu_{e^+}) \frac{z^4}{\sqrt{z^2 + (m_e/T)^2}} dz \quad (\text{B9})$$

$$\epsilon_\gamma = aT^4 \quad (\text{B10})$$

$$p_\gamma = \frac{aT^4}{3} \quad (\text{B11})$$

$$\epsilon_B = \frac{3}{2} n_N T \quad (\text{B12})$$

$$p_B = n_N T, \quad (\text{B13})$$

where

$$f(z, T, m, \mu) = \frac{1}{e^{\sqrt{z^2 + (m/T)^2} - \mu/T} + 1} \quad (\text{B15})$$

is the Fermi-Dirac distribution, m_e is the electron mass, n_N the nuclei number density, $a = 8\pi^5 k_B^4 / 15h^3 c^3 = 7.5657 \times 10^{-15} \text{erg cm}^{-3} \text{K}^{-4}$ is the radiation constant, and $A = 15a/\pi^4$. If the pair annihilation rate is zero, i.e., if the reaction $e^- + e^+ \leftrightarrow 2\gamma$ is in equilibrium, then the equality $\mu_{e^-} = -\mu_{e^+} \equiv \mu$ holds, since the equilibrium photons have zero chemical potential. Besides, charge neutrality implies that the difference in the number of electrons and positrons is equal to the number of protons in the baryonic matter, which can be expressed as:

$$n_{e^-}(\mu, T) - n_{e^+}(\mu, T) = Z n_B, \quad (\text{B16})$$

where n_B is the baryon number density and $1/2 < Z < 1$ is the average number of electrons per nucleon. The number density n_B is related to the other quantities as

$$\rho = m_p n_B + m_e (n_{e^-} + n_{e^+}), \quad (\text{B17})$$

where m_p is the proton mass. If the baryons are only protons, then $Z = 1$ and $n_N = n_B$. Together with Eq. (B16), this completely defines the mass density as a function of (μ, T) . The equation of state that relates the pressure with the mass and internal energy densities is thus defined implicitly as the parametric surface

$$\{(\rho(\mu, T), \epsilon(\mu, T), p(\mu, T)) : T > 0, \mu \geq 0\} \quad (\text{B18})$$

that satisfies all of the above relations.

In the cases relevant for the simulations performed in Sec. 10, we have that indeed the index γ in the equation of state of the plasma (30) satisfies $\gamma = 4/3$ with a maximum error of 0.2%.

REFERENCES

- Aimuratov, Y., Ruffini, R., Muccino, M., et al. 2017, ApJ, 844, 83
 Aksenov, A. G., Ruffini, R., & Vereshchagin, G. V. 2007, Physical Review Letters, 99, 125003

- Amati, L., & Della Valle, M. 2013, *International Journal of Modern Physics D*, 22, 30028
- Amati, L., Frontera, F., Vietri, M., et al. 2000, *Science*, 290, 953
- Atwood, W. B., Abdo, A. A., Ackermann, M., et al. 2009, *ApJ*, 697, 1071
- Barraud, C., Olive, J.-F., Lestrade, J. P., et al. 2003, *A&A*, 400, 1021
- Barthelmy, S. D., Chincarini, G., Burrows, D. N., et al. 2005, *Nature*, 438, 994
- Barthelmy, S. D., Baumgartner, W. H., Cummings, J. R., et al. 2013, *GRB Coordinates Network*, 15456
- Baumgartner, W. H., Barthelmy, S. D., Cummings, J. R., et al. 2014, *GRB Coordinates Network*, 16127
- Becerra, L., Bianco, C. L., Fryer, C. L., Rueda, J. A., & Ruffini, R. 2016, *ApJ*, 833, 107
- Becerra, L., Cipolletta, F., Fryer, C. L., Rueda, J. A., & Ruffini, R. 2015, *ApJ*, 812, 100
- Berger, E. 2014, *ARA&A*, 52, 43
- Bernardini, M. G., Bianco, C. L., Chardonnet, P., et al. 2005, *ApJL*, 634, L29
- Bethe, H. A. 1991, *The road from LOS Alamos*
- Bianco, C. L., & Ruffini, R. 2004, *ApJL*, 605, L1
- . 2005a, *ApJL*, 620, L23
- . 2005b, *ApJL*, 633, L13
- . 2006, *ApJL*, 644, L105
- Bianco, C. L., Ruffini, R., & Xue, S.-S. 2001, *A&A*, 368, 377
- Blandford, R. D., & McKee, C. F. 1976, *Physics of Fluids*, 19, 1130
- Bloom, J. S., Frail, D. A., & Sari, R. 2001, *AJ*, 121, 2879
- Bromberg, O., Nakar, E., Piran, T., & Sari, R. 2013, *ApJ*, 764, 179
- Butler, N., Ricker, G., Atteia, J.-L., et al. 2005, *GRB Coordinates Network*, 3570
- Caito, L., Amati, L., Bernardini, M. G., et al. 2010, *A&A*, 521, A80
- Caito, L., Bernardini, M. G., Bianco, C. L., et al. 2009, *A&A*, 498, 501
- Calderone, G., Ghirlanda, G., Ghisellini, G., et al. 2015, *MNRAS*, 448, 403
- Cavallo, G., & Rees, M. J. 1978, *MNRAS*, 183, 359
- Centko, S. B., Kasliwal, M., Harrison, F. A., et al. 2006, *ApJ*, 652, 490
- Cherubini, C., Geralico, A., Rueda, H. J. A., & Ruffini, R. 2009, *PhRvD*, 79, 124002
- Chester, M. M., Wang, X. Y., Cummings, J. R., et al. 2008, in *American Institute of Physics Conference Series*, Vol. 1000, American Institute of Physics Conference Series, ed. M. Galassi, D. Palmer, & E. Fenimore, 421–424
- Chincarini, G., Moretti, A., Romano, P., et al. 2007, *The Astrophysical Journal*, 671, 1903
- Chincarini, G., Mao, J., Margutti, R., et al. 2010, *Monthly Notices of the Royal Astronomical Society*, 406, 2113
- Cleveland, W., & Devlin, S. 1988, *Journal of the American Statistical Association*, 83, 596.
- <http://www.jstor.org/stable/2289282>
- Cline, T. L., Desai, U. D., Trainor, J., et al. 1979, *ApJL*, 229, L47
- Cobb, B. E. 2007, *GRB Coordinates Network*, 6296
- Colella, P., Graves, D. T., Johnson, J. N., et al. 2003, *Chombo software package for AMR applications design document*, Tech. Rep. LBNL-6615E
- Colgate, S. A. 1971, *ApJ*, 163, 221
- Costa, E., Frontera, F., Heise, J., et al. 1997, *Nature*, 387, 783
- Cummings, J. R., Barthelmy, S. D., Burrows, D. N., et al. 2007, *GRB Coordinates Network*, 6210, 1
- Dai, Z. G., Wang, X. Y., Wu, X. F., & Zhang, B. 2006, *Science*, 311, 1127
- Damour, T., & Ruffini, R. 1975, *Physical Review Letters*, 35, 463
- D’Avanzo, P., D’Elia, V., & Covino, S. 2008, *GRB Coordinates Network*, 8350
- de Pasquale, M., Piro, L., Gendre, B., et al. 2006, *A&A*, 455, 813
- de Ugarte Postigo, A., Fynbo, J. P. U., Thöne, C. C., et al. 2012, *A&A*, 548, A11
- Della Valle, M. 2011, *International Journal of Modern Physics D*, 20, 1745
- Dezalay, J.-P., Barat, C., Talon, R., et al. 1992, in *American Institute of Physics Conference Series*, Vol. 265, American Institute of Physics Conference Series, ed. W. S. Paciesas & G. J. Fishman, 304–309
- Eichler, D., Livio, M., Piran, T., & Schramm, D. N. 1989, *Nature*, 340, 126
- Evans, P. A., Beardmore, A. P., Page, K. L., et al. 2007, *A&A*, 469, 379
- . 2009, *MNRAS*, 397, 1177
- Falcone, A., Barbier, L., Barthelmy, S., et al. 2006, *GRB Coordinates Network*, 4655
- Falcone, A. D., Morris, D., Racusin, J., et al. 2007, *The Astrophysical Journal*, 671, 1921
- Fan, Y. Z., Zhang, B., & Proga, D. 2005, *ApJL*, 635, L129
- Fenimore, E. E., Palmer, D., Galassi, M., et al. 2003, in *American Institute of Physics Conference Series*, Vol. 662, *Gamma-Ray Burst and Afterglow Astronomy 2001: A Workshop Celebrating the First Year of the HETE Mission*, ed. G. R. Ricker & R. K. Vanderspek, 491–493
- Fermi, E. 1934, *Il Nuovo Cimento*, 11, 1

- Frail, D. A., Kulkarni, S. R., Nicastro, L., Feroci, M., & Taylor, G. B. 1997, *Nature*, 389, 261
- Frail, D. A., Kulkarni, S. R., Sari, R., et al. 2001, *ApJL*, 562, L55
- Frey, L. H., Fryer, C. L., & Young, P. A. 2013, *The Astrophysical Journal Letters*, 773, L7.
<http://stacks.iop.org/2041-8205/773/i=1/a=L7>
- Frontera, F., Costa, E., Piro, L., et al. 1998, *ApJL*, 493, L67
- Fruchter, A. S., Levan, A. J., Strolger, L., et al. 2006, *Nature*, 441, 463
- Fryer, C., Benz, W., Herant, M., & Colgate, S. A. 1999, *ApJ*, 516, 892
- Fryer, C. L., Oliveira, F. G., Rueda, J. A., & Ruffini, R. 2015, *Physical Review Letters*, 115, 231102
- Fryer, C. L., Rueda, J. A., & Ruffini, R. 2014, *ApJL*, 793, L36
- Fryer, C. L., Woosley, S. E., & Hartmann, D. H. 1999, *The Astrophysical Journal*, 526, 152
- Galama, T. J., Vreeswijk, P. M., van Paradijs, J., et al. 1998, *Nature*, 395, 670
- Gamow, G., & Schoenberg, M. 1940, *Physical Review*, 58, 1117
- . 1941, *Physical Review*, 59, 539
- Gehrels, N., Chipman, E., & Kniffen, D. A. 1993, *A&AS*, 97, 5
- Gehrels, N., Ramirez-Ruiz, E., & Fox, D. B. 2009, *ARA&A*, 47, 567
- Golenetskii, S., Aptekar, R., Frederiks, D., et al. 2013, *GRB Coordinates Network*, 15413
- Golenetskii, S., Aptekar, R., Mazets, E., et al. 2008, *GRB Coordinates Network*, 7862
- Golenetskii, S., Aptekar, R., Frederiks, D., et al. 2014, *GRB Coordinates Network*, 16134
- Golenetskii, S., Aptekar, R., Frederiks, D., et al. 2015, *GRB Coordinates Network*, 1851, 1
- Goodman, J. 1986, *ApJL*, 308, L47
- Gursky, H., & Ruffini, R., eds. 1975, *Astrophysics and Space Science Library*, Vol. 48, Neutron stars, black holes and binary X-ray sources; Proceedings of the Annual Meeting, San Francisco, Calif., February 28, 1974
- Heisenberg, W. 1943, *Zeitschrift fur Physik*, 120, 513
- Hjorth, J., & Bloom, J. S. 2012, *Cambridge Astrophysics Series*, Vol. 51, The Gamma-Ray Burst - Supernova Connection, ed. C. Kouveliotou, R. A. M. J. Wijers, & S. Woosley (Cambridge University Press (Cambridge)), 169–190
- Hurley, K., Cline, T., Mazets, E., et al. 2000, *ApJL*, 534, L23
- in 't Zand, J. J. M., Amati, L., Antonelli, L. A., et al. 1998, *ApJL*, 505, L119
- in't Zand, J. J. M., Kuiper, L., Amati, L., et al. 2001, *ApJ*, 559, 710
- Itoh, N., Adachi, T., Nakagawa, M., Kohyama, Y., & Munakata, H. 1989, *ApJ*, 339, 354
- Izzo, L., Ruffini, R., Penacchioni, A. V., et al. 2012, *A&A*, 543, A10
- Jakobsson, P., Fynbo, J. P. U., Vreeswijk, P. M., & de Ugarte Postigo, A. 2008, *GRB Coordinates Network*, 8077
- Jaunsen, A. O., Fynbo, J. P. U., Andersen, M. I., & Vreeswijk, P. 2007, *GRB Coordinates Network*, 6216
- Jin, Z.-P., Fan, Y.-Z., & Wei, D.-M. 2010, *ApJ*, 724, 861
- Klebesadel, R. W. 1992, in *Gamma-Ray Bursts - Observations, Analyses and Theories*, ed. C. Ho, R. I. Epstein, & E. E. Fenimore (Cambridge University Press), 161–168
- Klebesadel, R. W., Strong, I. B., & Olson, R. A. 1973, *ApJL*, 182, L85
- Kouveliotou, C., Meegan, C. A., Fishman, G. J., et al. 1993, *ApJL*, 413, L101
- Krimm, H. A., Beardmore, A. P., Brown, P. J., et al. 2008, *GRB Coordinates Network*, 8648
- Kruehler, T., Tanvir, N. R., Malesani, D., Xu, D., & Fynbo, J. P. U. 2014, *GRB Coordinates Network*, 15900
- Kumar, P., & Zhang, B. 2015, *PhR*, 561, 1
- Landau, L. D., & Lifshitz, E. M. 1980, *Statistical physics. Pt.1, Third edition* (Butterworth-Heinemann)
- Ledoux, C., Vreeswijk, P., Smette, A., Jaunsen, A., & Kaufer, A. 2006, *GRB Coordinates Network*, 5237
- Lien, A. Y., Barthelmy, S. D., Chester, M. M., et al. 2014, *GRB Coordinates Network*, 15784
- Lyman, J. D., Bersier, D., James, P. A., et al. 2016, *MNRAS*, 457, 328
- MacFadyen, A., & Woosley, S. E. 1999, *ApJ*, 524, 262 P., & Rees, MJ 1992a (*ApJ*)
- MacFadyen, A. I., & Woosley, S. E. 1999, *ApJ*, 524, 262
- Malesani, D., Xu, D., Fynbo, J. P. U., et al. 2014, *GRB Coordinates Network*, 15800
- Mangano, V., Cummings, J. R., Cusumano, G., et al. 2008, *GRB Coordinates Network*, 7847
- Mao, S., & Yi, I. 1994, *ApJL*, 424, L131
- Margutti, R., Guidorzi, C., Chincarini, G., et al. 2010, *Monthly Notices of the Royal Astronomical Society*, 406, 2149
- Marisaldi, M., Fuschino, F., Galli, M., et al. 2008, *GRB Coordinates Network*, 7866, 1
- Marshall, F. E., Cummings, J. R., Gronwall, C., et al. 2014, *GRB Coordinates Network*, 16118
- Maselli, A., D'Ai, A., Lien, A. Y., et al. 2015, *GRB Coordinates Network*, 1847, 1

- Masumitsu, T., Negoro, H., Kawai, N., et al. 2015, GRB Coordinates Network, 18525
- Mazets, E. P., Golenetskii, S. V., Ilinskii, V. N., et al. 1981, *Ap&SS*, 80, 3
- McBreen, S. 2009, GRB Coordinates Network, 9415, 1
- Mészáros, P. 2002, *ARA&A*, 40, 137
- . 2006, *Reports on Progress in Physics*, 69, 2259.
<http://stacks.iop.org/0034-4885/69/i=8/a=R01>
- Meszáros, P., Laguna, P., & Rees, M. J. 1993, *ApJ*, 415, 181
- Mészáros, P., & Rees, M. J. 1997, *The Astrophysical Journal Letters*, 482, L29
- Metzger, M. R., Djorgovski, S. G., Kulkarni, S. R., et al. 1997, *Nature*, 387, 878
- Mignone, A., Zanni, C., Tzeferacos, P., et al. 2011, *The Astrophysical Journal Supplement Series*, 198, 7.
<https://doi.org/10.1088%2F0067-0049%2F198%2F1%2F7>
- Morgan, A., Grupe, D., Gronwall, C., et al. 2005, GRB Coordinates Network, 3577
- Munakata, H., Kohyama, Y., & Itoh, N. 1985, *ApJ*, 296, 197
- Narayan, R., Paczynski, B., & Piran, T. 1992, *ApJL*, 395, L83
- Narayan, R., Piran, T., & Shemi, A. 1991, *ApJL*, 379, L17
- Negreiros, R., Ruffini, R., Bianco, C. L., & Rueda, J. A. 2012, *A&A*, 540, A12
- Nousek, J. A., Kouveliotou, C., Grupe, D., et al. 2006, *ApJ*, 642, 389
- Nysewander, M., Reichart, D. E., Crain, J. A., et al. 2009, *ApJ*, 693, 1417
- Oppenheimer, J. R., & Volkoff, G. M. 1939, *Physical Review*, 55, 374
- Paczynski, B. 1986, *ApJL*, 308, L43
- Paczyński, B. 1998, *The Astrophysical Journal Letters*, 494, L45
- Pagani, C., Baumgartner, W. H., Chester, M. M., et al. 2008, GRB Coordinates Network, 8059
- Page, K. L., Barthelmy, S. D., Baumgartner, W. H., et al. 2014, *GCN Report*, 460
- Page, K. L., Willingale, R., Bissaldi, E., et al. 2009, *MNRAS*, 400, 134
- Panaitescu, A., & Mészáros, P. 1999, *ApJ*, 526, 707
- Patricelli, B., Bernardini, M. G., Bianco, C. L., et al. 2012, *ApJ*, 756, 16
- Penacchioni, A. V., Ruffini, R., Bianco, C. L., et al. 2013, *A&A*, 551, A133
- Penacchioni, A. V., Ruffini, R., Izzo, L., et al. 2012, *A&A*, 538, A58
- Perley, D. A., Cao, Y., & Cenko, S. B. 2014, GRB Coordinates Network, 17228
- Perley, D. A., Hillenbrand, L., & Prochaska, J. X. 2015, GRB Coordinates Network, 18487
- Perley, D. A., Krühler, T., Schulze, S., et al. 2016, *ApJ*, 817, 7
- Piran, T. 1999, *PhR*, 314, 575
- . 2004, *Reviews of Modern Physics*, 76, 1143
- Piran, T., Shemi, A., & Narayan, R. 1993, *MNRAS*, 263, 861
- Piro, L., De Pasquale, M., Soffitta, P., et al. 2005, *ApJ*, 623, 314
- Pisani, G. B., Izzo, L., Ruffini, R., et al. 2013, *A&A*, 552, L5
- Pisani, G. B., Ruffini, R., Aimuratov, Y., et al. 2016, *ApJ*, 833, 159
- Racusin, J. L., Baumgartner, W. H., Brown, P. J., et al. 2008, GRB Coordinates Network, 8344
- Rees, M. J., & Meszaros, P. 1992, *MNRAS*, 258, 41P
- . 1994, *ApJL*, 430, L93
- Romano, P., Campana, S., Chincarini, G., et al. 2006, *A&A*, 456, 917
- Rossi, A., Afonso, P., & Greiner, J. 2009, GRB Coordinates Network, 9382
- Rowlinson, B. A., Beardmore, A. P., Evans, P. A., et al. 2009, GRB Coordinates Network, 9374
- Rueda, J. A., & Ruffini, R. 2012, *ApJL*, 758, L7
- Rueda, J. A., Aimuratov, Y., de Almeida, U. B., et al. 2017, *International Journal of Modern Physics D*, 26, 1730016
- Ruffini, R. 1998, in *Frontiers Science Series 23: Black Holes and High Energy Astrophysics*, ed. H. Sato & N. Sugiyama, Vol. 23, 167
- Ruffini, R. 2015, in *Thirteenth Marcel Grossmann Meeting: On Recent Developments in Theoretical and Experimental General Relativity, Astrophysics and Relativistic Field Theories*, ed. K. Rosquist, 242–314
- Ruffini, R., Bianco, C. L., Chardonnet, P., Fraschetti, F., & Xue, S.-S. 2002, *ApJL*, 581, L19
- Ruffini, R., Bianco, C. L., Fraschetti, F., Xue, S.-S., & Chardonnet, P. 2001a, *ApJL*, 555, L107
- . 2001b, *ApJL*, 555, L113
- . 2001c, *ApJL*, 555, L117
- Ruffini, R., Salmonson, J. D., Wilson, J. R., & Xue, S. 2000, *A&A*, 359, 855
- Ruffini, R., Salmonson, J. D., Wilson, J. R., & Xue, S.-S. 1999, *A&A*, 350, 334
- Ruffini, R., Song, D. J., & Stella, L. 1983, *A&A*, 125, 265
- Ruffini, R., Vereshchagin, G., & Xue, S. 2010, *PhR*, 487, 1
- Ruffini, R., & Wilson, J. 1973, *Physical Review Letters*, 31, 1362
- Ruffini, R., Muccino, M., Bianco, C. L., et al. 2014, *A&A*, 565, L10
- Ruffini, R., Muccino, M., Kovacevic, M., et al. 2015a, *ApJ*, 808, 190

- Ruffini, R., Wang, Y., Enderli, M., et al. 2015b, *ApJ*, 798, 10
- Ruffini, R., Izzo, L., Bianco, C. L., et al. 2015c, *Astronomy Reports*, 59, 626
- Ruffini, R., Rueda, J. A., Muccino, M., et al. 2016a, *ApJ*, 832, 136
- Ruffini, R., Muccino, M., Aimuratov, Y., et al. 2016b, *ApJ*, 831, 178
- Sakamoto, T., Barthelmy, S. D., Baumgartner, W. H., et al. 2014, *GRB Coordinates Network*, 15805
- Sari, R., Piran, T., & Halpern, J. P. 1999, *ApJL*, 519, L17
- Shemi, A., & Piran, T. 1990, *ApJL*, 365, L55
- Shirasaki, Y., Yoshida, A., Kawai, N., et al. 2008, *PASJ*, 60, 919
- Smith, N. 2014, *ARA&A*, 52, 487
- Smith, N., Li, W., Filippenko, A. V., & Chornock, R. 2011, *MNRAS*, 412, 1522
- Sonbas, E., Cummings, J. R., D'Elia, V., et al. 2014, *GRB Coordinates Network*, 17206
- Stamatikos, M., Cummings, J. R., Evans, P. A., et al. 2009, *GRB Coordinates Network*, 9768
- Svensson, K. M., Levan, A. J., Tanvir, N. R., Fruchter, A. S., & Strolger, L.-G. 2010, *MNRAS*, 405, 57
- Swenson, C. A., & Roming, P. W. A. 2014, *ApJ*, 788, 30
- Tanvir, N. R., Levan, A. J., Cucchiarra, A., Perley, D., & Cenko, S. B. 2014, *GRB Coordinates Network*, 16125
- Tavani, M. 1998, *ApJL*, 497, L21
- Taylor, E. F., & Wheeler, J. A. 1992, *Spacetime physics - Introduction to special relativity* (2nd edition)
- Toelge, K., Yu, H. F., & Meegan, C. A. 2015, *GRB Coordinates Network*, 1849, 1
- Troja, E., Piro, L., Vasileiou, V., et al. 2015, *ApJ*, 803, 10
- Troja, E., Barthelmy, S. D., Baumgartner, W. H., et al. 2013, *GRB Coordinates Network*, 15402
- van Paradijs, J., Groot, P. J., Galama, T., et al. 1997, *Nature*, 386, 686
- von Kienlin, A., & Bhat, P. N. 2014, *GRB Coordinates Network*, 15796
- Wheeler, J. A. 1937, *Physical Review*, 52, 1107
- Woosley, S. E. 1993, *ApJ*, 405, 273
- Woosley, S. E., & Bloom, J. S. 2006, *ARA&A*, 44, 507
- Xu, D., Fynbo, J. P. U., Jakobsson, P., et al. 2013, *GRB Coordinates Network*, 15407
- Yi, S.-X., Wu, X.-F., Wang, F.-Y., & Dai, Z.-G. 2015, *The Astrophysical Journal*, 807, 92
- Yu, H.-F. 2014, *GRB Coordinates Network*, 17216
- Yuan, F., Schady, P., Racusin, J. L., et al. 2010, *ApJ*, 711, 870
- Zel'dovich, Y. B., Ivanova, L. N., & Nadezhin, D. K. 1972, *Soviet Ast.*, 16, 209
- Zhang, B., Fan, Y. Z., Dyks, J., et al. 2006, *ApJ*, 642, 354
- Zhang, F.-W., Shao, L., Yan, J.-Z., & Wei, D.-M. 2012, *ApJ*, 750, 88
- Ziaepour, H. Z., Barthelmy, S. D., Gehrels, N., et al. 2006, *GRB Coordinates Network*, 5233